INVESTIGATING THE SPECTRUM OF ATOMS IN MULTIPLE-RADIOFREQUENCY DRESSED POTENTIALS FOR COHERENT SPLITTING OF QUANTUM GASES

KATHRIN LUKSCH

Hertford College

University of Oxford

A thesis submitted for the degree of

Doctor of Philosophy

Hilary Term, 2019

Kathrin Luksch: *Investigating the Spectrum of Atoms in Multiple-Radiofrequency Dressed Potentials for Coherent Splitting of Quantum Gases,* Hilary Term, 2019

Investigating the Spectrum of Atoms in Multiple-Radiofrequency Dressed Potentials for Coherent Splitting of Quantum Gases

Kathrin Luksch

Hertford College

University of Oxford

A thesis submitted for the degree of Doctor of Philosophy

Hilary Term 2019

ABSTRACT

This thesis presents experimental work to investigate the properties of ultracold rubidium atoms in multiple-radiofrequency dressed potentials and detailed theoretical calculations to understand this system. The use of multiple frequencies rather than a single dressing frequency increases the complexity of the spectrum, and we present theoretical calculations that predict all possible transitions as well as the corresponding strengths. Extensive measurements for dressing with a single and multiple frequencies have verified these predictions, observing transitions up to tenth order in the probe field. We observe previously unknown transitions even for the single-frequency case and have uncovered further transitions which we explain by the non-linearity of the Zeeman effect even at our small field strengths.

These results are used to understand the absorption spectrum as the potential transforms from a single to a double well in order to split a Bose-Einstein condensate. This is important for applications since spurious noise leads to atom loss if it is resonant with a transition between eigenstates. We present a new method of splitting, replacing adiabatic ramps with a projection, that reduces the duration of the ramps as well as the spectrum of resonances throughout the ramps, thus reducing losses.

The new experimental techniques will allow observation of the thermalisation of a two-dimensional quantum system using ultracold gases. We discuss how multiple-radiofrequency dressed potentials can be used to confine ultracold atoms in two dimensions, and subsequently split the trapped cloud into two parallel sheets. After a varying hold time, the atoms can be released and overlapped to produce interference fringes. Analysis of the fringes determines how the relative phase between the two sheets thermalises. Information can be accumulated to determine the probability distribution of the integrated contrast, which can then be compared to the equilibrium distribution to determine if and how the relative phase thermalises. This promises to answer key questions in non-equilibrium physics.

PUBLICATIONS

The following publications emerged from the work towards my D.Phil:

- K. Luksch, E. Bentine, A. J. Barker, S. Sunami, T. L. Harte, B. Yuen, and C. J. Foot. "Probing multiple-frequency atom-photon interactions with ultracold atoms". In: *New Journal of Physics* 21.7 (2019), p. 073067.
  Chapters 5 and 6 are based on and use parts of this publication.

- T. L. Harte, E. Bentine, K. Luksch, A. J. Barker, D. Trypogeorgos, B. Yuen, and C. J. Foot. "Ultracold atoms in multiple radio-frequency dressed adiabatic potentials". In: *Physical Review A* 97.1 (2018), p. 013616.

- E. Bentine, T. L. Harte, K. Luksch, A. J. Barker, J. Mur-Petit, B. Yuen, and C. J. Foot. "Species-selective confinement of atoms dressed with multiple radiofrequencies". In: *Journal of Physics B* 50.9 (2017), p. 094093.

- A. J. Barker, H. Style, K. Luksch, S. Sunami, D. Garrick, F. Hill, C. J. Foot, and E. Bentine. "Applying machine learning optimization methods to the production of a quantum gas". 2019. arXiv:1908.08495 [cond-mat.quant-gas].

During the work on my thesis, I also played a major role in developing and writing the grant proposal for the EPSRC grant EP/S013105/1:

- C. J. Foot. *Investigating non-equilibrium physics and universality using two-dimensional quantum gases.* https://gow.epsrc.ukri.org/NGBOViewGrant.aspx?GrantRef=EP/S013105/1. 2018.

Chapter 2 is based on and uses parts of this grant proposal.

ACKNOWLEDGMENTS

I am immensely grateful for all the support I received while working towards this thesis.

First, I would like to thank my supervisor Chris Foot for offering me a position in his group, and for the guidance and independence he offered throughout.

A huge thank you goes to everyone who has introduced me to the experimental apparatus – Ben Yuen for showing me the ropes with the optical lattice, as well as introducing me to the resolvent formalism; Tiffany Harte and Elliot Bentine for making the cold basement a welcoming place, for their patience, incredibly hard work, and enthusiasm, and for creating a smooth-running experimental apparatus. Thanks also to Tiffany for plenty of amazing cake and to Elliot for believing in fringes until the very end.

Thanks to Adam Barker, Shinichi Sunami, and most recently David Garrick, for their dedication, energy, and creativity. I know the experiment is safe in their capable hands. Best of luck for the future! Thanks also to the rest of the group – Ed Owen, Sean Ravenhall, Leo Xu, and Rowan Moore – for making my stay in Oxford fun, both inside and outside the lab.

Furthermore, I would like to thank the anonymous referee of the spectroscopy paper for their detailed and helpful feedback.

I am grateful to the support staff of the Clarendon Laboratory for their help in dealing with problems large and small, be it water leaks or short circuits, and for providing a near-endless supply of cable ties and glue.

H. P. aus F. for being an inspiring teacher: Vielen Dank!

Big thanks also go to my friends and family, for listening to my rants, and for distracting me when needed. Special thanks to my parents for their unconditional support – even when I abandoned mathematics for the 'dark side' that is experimental physics.

Und natürlich: Danke, Niko.

CONTENTS

LIST OF FIGURES

ACRONYMS

AOD	acousto-optic deflector
BEC	Bose-Einstein condensate
BKT	Berezinskii-Kosterlitz-Thouless
CCD	charge-coupled device
DDS	direct digital synthesis
ECDL	external cavity diode laser
ETH	eigenstate thermalisation hypothesis
KS	Kolmogorov-Smirnov
KZ	Kibble-Zurek
MOT	magneto-optical trap
MRF	multiple radiofrequency
NEQ	non-equilibrium
PDF	probability distribution function
RF	radiofrequency
RWA	rotating wave approximation
SNR	signal-to-noise ratio
SRF	single radiofrequency
TAAP	time-averaged adiabatic potential
TOF	time-of-flight

TOP time-orbiting potential

1D one-dimensional

2D two-dimensional

3D three-dimensional

1

INTRODUCTION

Relaxation of non-equilibrium (NEQ) states is ubiquitous, ranging from the thermalisation of a cup of coffee to the emergence of structure in the early universe [1]. Equilibration of classical systems has been described with great success, but there is no general theoretical framework for quantum mechanics which describes how equilibrium is reached; and direct numerical simulation can be very challenging. Open questions include how local dynamics lead to thermal states, and on what timescale thermalisation occurs [2–5].

Ultracold quantum gases provide a powerful platform to investigate these questions experimentally. The development of laser cooling enabled the preparation and confinement of cold gases [**Nobel1997**]. The subsequent achievement of creating Bose-Einstein condensates (BECs) [**Nobel2001**] led to a wide range of experiments exploring questions from the foundations of quantum mechanics to many-body physics. Further developments led to unprecedented control over individual quantum systems [**Nobel2012**].

Ultracold quantum gases are extremely well isolated from the environment, allowing investigation of closed quantum systems. The timescales associated with these systems are readily accessible, a characteristics that makes them particularly suitable for observing the dynamics of phase transitions. The recent spectacular progress in experimental techniques for preparing and manipulating ultracold quantum gases now enables fundamental theoretical questions about NEQ systems to be investigated in unprecedented detail [6–11]. Moreover, the repeatability of cold-atom experiments allows us to measure distribution functions of observables, not just their expecta-

tion values [12–14]. These probability distributions represent the essence of quantum mechanics and enable comparison to theoretical predictions.

Both magnetic and light fields can be used to confine ultracold atoms, and many different architectures exist. While optical dipole traps offer the benefit of nearly arbitrary potential shapes, magnetic potentials are smooth and robust. These advantages over dipole traps are particularly useful when very low heating rates are required, and for mobile applications [**Becker2018**]. Dressing atoms in static magnetic fields with radiofrequency (RF) radiation increases the versatility of available shapes [15]. In Oxford, we have recently extended this method using multiple radiofrequency (MRF) fields to confine atoms [16]. This combines the advantages of magnetic traps with the capability of making more versatile potential shapes.

Atoms have been dressed with multiple frequencies before, and multi-frequency optical dipole traps can be used to confine quantum gases in superlattices [21, 22] or species-selective potentials [23]. In these cases, however, the frequency of the radiation is far from resonance so that the perturbation arising from each frequency component can be treated independently. Using this approach to describe atoms dressed with MRFs, as in Reference [24], is overly simplistic when coherent processes are important, such as for separations between frequency components comparable to the Rabi frequencies.

Rather than treating frequency components independently, we therefore calculate MRF-dressed eigenstates by solving the full Hamiltonian in our theoretical treatment. Measurements of ultracold atoms trapped in such a potential showed the influence of the non-resonant frequencies on the eigenenergies, demonstrating the need to take these into account [16]. We have used MRF-dressing to confine atoms in a double-well potential of two parallel sheets, with full control on the distance between the two sheets as well as the height of the barrier separating them. The spacing can be made sufficiently small to realize matter-wave interferometry [25]. The addition of multiple frequencies adds versatility to magnetic traps but retains their smoothness and robustness, with the possibility of very low heating rates. These potentials offer a tunable geometry and the ability to influence the dimensionality of the trapped

gas [16, 26]. These characteristics make MRF-dressed traps extremely suitable for investigating NEQ physics with ultracold atoms.

The work in this thesis is presented in two parts. First, we show that MRF-dressed potentials are well suited to investigating NEQ physics in two-dimensional (2D) systems and propose experiments that can be carried out on our existing apparatus. We then detail progress towards achieving these goals. Secondly, we fully characterise transitions in MRF-dressed potentials both theoretically and experimentally.

In part, the experiments proposed in the first part of this thesis have been inspired by investigations on thermalisation in one-dimensional (1D) systems [12, 27] and the intense interest those results have stimulated in the theoretical community. While in one dimension the dynamics are determined by quantum fluctuations, quantum systems confined to two dimensions are especially interesting. Quantum fluctuations play a large role and prevent true long-range order, however, a phase transition to a superfluid at non-zero temperature does exist [28, 29].

This work shows that 2D quantum gases are an excellent test bed for understanding behaviour close to the critical point, and when crossing the phase transition. We argue that MRF-dressed potentials are a promising tool to observe thermalisation and explain how a 2D superfluid in an NEQ state can be prepared using our cold-atom apparatus, and how we plan to observe the phase fluctuations and density evolution.

Using several dressing frequencies introduces a multitude of transitions into the spectrum, making MRF-dressed potentials susceptible to RF noise. We fully characterise this spectrum in the second part of the thesis. Even for a single frequency we predict new transitions which go beyond the well-known Autler-Townes splitting [119]. We further generalise the results to describe the spectrum when dressing atoms with multiple frequencies, and verify these results experimentally.

We spectroscopically probe a trapped BEC over a wide range of frequencies and find agreement between predicted and measured results. We observe transitions up to tenth order in the probe field, as well as transitions that were previously assumed to be forbidden. We explain the latter with the non-linearity of the Zeeman effect.

Understanding loss spectra is crucial when choosing parameters for MRF-dressed potentials, and when diagnosing loss for existing systems. The theoretical description

we present, however, is valid beyond the specific application of RF-dressed potentials, and is widely applicable to multi-frequency processes.

This thesis is structured as follows: In Chapter 2, we start by detailing the proposed experiments to investigate NEQ physics in 2D gases. We then explain the theory of RF-dressed potentials and their extension to multiple frequencies in Chapter 3, and their implementation on our experimental apparatus in Chapter 4, focussing on the proposed experiments. In Chapter 5, we theoretically investigate transitions in MRF-dressed potentials and fully characterise the RF spectrum. We proceed to test these predictions in Chapter 6, with extensive measurements of spectra for atoms dressed by a single and by multiple frequencies. Finally, we present a method to split a BEC using MRF-dressed potentials in Chapter 7 before concluding and giving an outlook in Chapter 8.

2

THERMALISATION OF TWO-DIMENSIONAL QUANTUM SYSTEMS

Equilibrium states are readily observable, and have thus been investigated in great detail. While it is mostly straightforward to disrupt a system and thus prepare an NEQ state, it is often difficult to observe the path that it follows towards equilibrium. Figure 2.1 illustrates the difficulty of investigating NEQ physics as well as different paths to equilibrium.

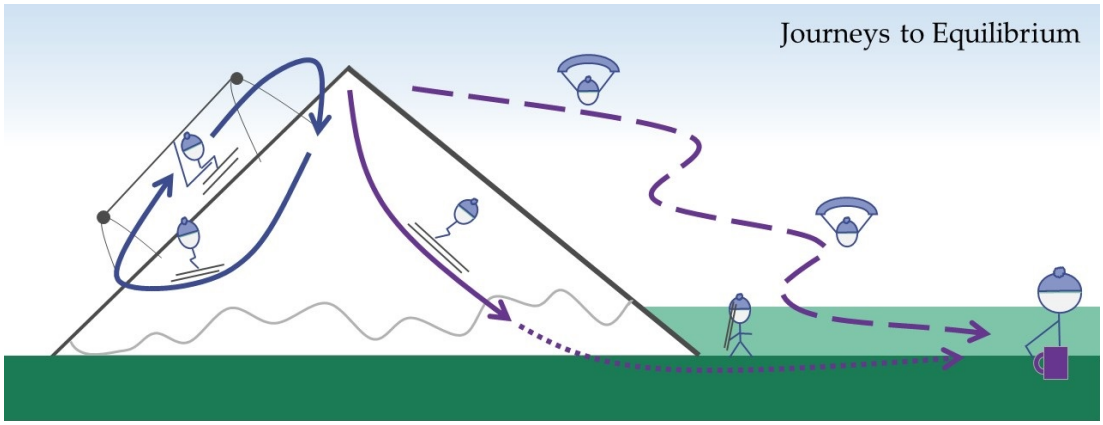

Figure 2.1: Different journeys to equilibrium are illustrated in this figure. Thermalised states are easy to observe, while the observation of NEQ states requires 'climbing the mountain' as well as following the sometimes rapid evolution of the state. Thermalisation at a constant rate is illustrated (purple, dashed line). A different path to thermal equilibrium is illustrated in purple, with rapid prethermalisation as a solid line and the slow final thermalisation dotted. Finally, a non-thermalising equilibrium state is illustrated in blue. This figure is based on one made by Adam Barker.

An out-of-equilibrium state may thermalise, and most examples that are commonly known consist of thermalisation on one timescale. Examples exist which display at least two timescales: a rapid initial evolution that has been termed 'prethermal-

isation', and a much slower evolution to the final thermal state. The intermediate prethermalised state appears thermal, but has not fully thermalised. The term was originally introduced to explain the apparent rapid thermalisation after collisions of heavy nuclei [32]. Additionally, systems exist that do not thermalise.

Cold atoms provide a means to investigate quantum systems out of equilibrium. The timescales are easily accessible and individual atoms, density distributions and momentum distributions can be observed. Furthermore, the same state can reliably and repeatedly be prepared to obtain sufficient statistics and probability distributions.

In this chapter we lay out proposed experiments on thermalisation of a closed 2D quantum system [33]. Preparing a 2D superfluid in an NEQ state by a non-adiabatic change in the density allows observation of the subsequent phase fluctuations and density evolution. In turn, these provide evidence of the timescales and mechanisms of thermalisation.

We start by giving an overview of related work in Section 2.1, before explaining the proposed experiments in Section 2.2. In Section 2.3 we detail the specific interferometric measurements necessary to achieve the objectives.

2.1 RELATED WORK

We start by elaborating on thermalisation in quantum systems, as compared to classical systems. We then give examples of experiments in one dimension that investigated a lack of thermalisation, before providing some background on 2D systems.

2.1.1 *Eigenstate Thermalisation Hypothesis*

Classical systems thermalise provided they are sufficiently ergodic. Such cases are well described by statistical mechanics and all microstates are considered to be equally probable [34]. It is not obvious how to reconcile this statement with the unitary evolution of closed quantum systems, but the eigenstate thermalisation hypothesis (ETH)

has emerged as a widely accepted explanation. This postulates the conditions under which local observables of the system's eigenstates can be described using a thermal distribution [34–36]. There is numerical and experimental evidence to support the ETH [37–39]. The recent experiments in an optical lattice [39] demonstrated the conjecture of the ETH extremely well: a quantum system that is initially in a pure state will stay in a pure state throughout the unitary time evolution. When measuring local observables, however, the results are thermal due to entanglement between subsystems. This means that eigenstates of complex quantum systems – although pure – look like thermal states that have the same expectation value for energy.

2.1.2 *Experiments in One Dimension*

There are classical systems that fail to reach a thermal state, such as so-called integrable systems which have a large number of conserved quantities. The Fermi-Pasta-Ulam problem is a famous example of an integrable system that exhibits recurrences rather than thermalisation [40].

Quantum mechanically, the Lieb-Liniger model describing 1D systems is an example of an integrable system. Experiments revealed that 1D Bose gases do not equilibrate on the timescales accessible in the experiments but rather relax to a non-thermal state, even when the integrability is weakly broken [12, 27, 41]. In the experiments relevant to this thesis [12, 27], a 1D quasi-condensate was split lengthways to prepare two 1D quantum gases with zero relative phase. These two clouds evolved independently under the strong local phase fluctuations in a quasi-1D system, but the relative phase did not reach an equilibrium distribution. Instead, the system attained a prethermal state. Further experiments found that relaxation is local, resulting in light-cone-like decay of correlations [42], and that the prethermalised state is described by a generalised Gibbs ensemble [43]. Recently, the effect of quantum tunnelling between the two gases was investigated [44, 45] and recurrences were observed [46].

2.1.3 *Experiments in Two Dimensions*

Our proposed work on 2D systems has three notable differences to the experiments conducted with 1D gases. First, 2D quantum systems are non-integrable and are predicted to thermalise [47]. Thus our experiments will add to the very few examples of closed quantum systems where equilibration has been observed in microscopic detail. Secondly, there is a quantum critical point associated with the Berezinskii-Kosterlitz-Thouless (BKT) transition to a superfluid phase. Near this point, properties of the system scale with a set of universal critical exponents. Thirdly, the decoherence of the relative phase cannot be explained solely by phonon propagation, as in 1D, and density fluctuations in the form of vortices play a significant role.

Experimental evidence of the BKT transition was first noted in helium films [48], before the theoretical description by Berenzinskii, and Kosterlitz & Thouless [28, 29]. Further investigation in helium films supported this [49], and the phase transition has since been observed in various 2D systems, including thin superconducting films, arrays of Josephson Junctions, and 2D atomic hydrogen [50–52]. Several examples of ultracold atoms trapped in the quasi-2D regime exist, trapped in various combinations of optical and magnetic fields [53–60]. A magnetic trap has been demonstrated, using similar RF-dressed potentials to those presented in this thesis [26].

2D superfluidity is synonymous with quasi-long-range order [61, 62]. Phase correlations decay as a power-law of the separation rather than exponentially, since thermal fluctuations destroy long-range order for any non-zero temperature. In contrast to other phase transitions, there is not a spatially uniform order parameter, but rather the above-mentioned phase correlations g_1:

$$g_1(x,x') := \left\langle \hat{\Psi}^\dagger(x)\hat{\Psi}(x') \right\rangle \propto \begin{cases} (x-x')^{-\alpha}, & T < T_c, \\ e^{(x-x')/l}, & T > T_c, \end{cases} \tag{2.1}$$

where $\hat{\Psi}(x)$ is the annihilation operator for a particle at position x. The value for α lies between 0 and 1/4, such that the decay of correlations is extremely slow. Here, $\alpha = 1/(n_s\lambda^2)$, with λ the thermal wavelength and n_s the superfluid density [61],

and l is the correlation length for a gas above the BKT transition. Equilibrium phase correlations have been measured in a 2D atomic Bose gas, but only the first-order correlation function was inferred in these experiments [63]. The accurate verification of $\alpha = 1/4$ is still an active field of research within the cold-atom community.

Density fluctuations are strongly suppressed in the superfluid phase, and vortex-antivortex pairs form. The size of these pairs is on the order of the healing length, such that they do not have a significant effect on the long-range behaviour of the phase. Above the transition unbound vortices proliferate, causing strong local density variations [61, 62]. A measurement of the distribution of unbound vortices by observing them as holes in the density distribution after a time-of-flight (TOF) expansion has identified pairwise correlations consistent with unbound vortex-antivortex pairs [64].

While the Mermin-Wagner theorem proves the lack of long-range order in infinite 2D systems, finite size effects are important, and a true BEC exists in experimentally feasible situations [61]. Finite system size also leads to a finite crossover region, rather than an instantaneous jump, for the superfluid density at the transition. We detail in Section 4.4 how the experimental implementation allows some investigations into boundary effects.

2.1.4 *Theoretical Predictions for Two Dimensions*

It has been proposed that out-of-equilibrium dynamics close to the BKT critical point can be investigated by splitting a 2D Bose gas into two parallel components [47, 65, 66], analogous to the experiments in one dimension [12, 27, 42–45]. The split constitutes a sudden non-adiabatic change of the density which can be designed to leave the two daughter clouds in a 'superheated superfluid' state, i. e. with a phase-space density below the critical value, and is predicted to drive a phase transition from super to normal fluid.

We expect the system to change on at least two timescales: initial light-cone-like evolution of the relative phase with a rapid relaxation time approximately inversely proportional to the bandwidth of the spectrum of phonons excited during the split.

Initially this evolution is driven by quantum fluctuations, but vortices are predicted to disrupt phonon propagation at longer times, as bound vortex-antivortex pairs form. These are the lowest energy thermal excitations of a 2D system. This behaviour has been called the 'reverse Kibble-Zurek (KZ) mechanism', as the relaxation towards equilibrium from a state of initial order resembles the inverse of the widely-investigated KZ mechanism [1, 67]. Observing this in reverse, within a closed quantum system, has important advantages such as precise control of initial conditions and start time.

2.2 PROPOSED EXPERIMENTS

The ability to isolate ultracold gases from the environment makes them ideal for studying relaxation in closed quantum systems. We propose to use a 2D quantum degenerate Bose gas to investigate NEQ dynamics near a critical point, and how these lead to thermal equilibrium. We will measure the evolution of phase correlations towards an equilibrium distribution and how this process is accompanied by the appearance of unbound vortices.

An atomic Bose gas of ^{87}Rb will be confined in an RF-dressed potential [15, 16, 26] where atoms are restricted to move in a 2D plane, and cooled below the superfluid transition. We coherently split the cloud in two, such that the system is out of equilibrium with zero relative phase between the two components, as illustrated in Figure 2.2 (a). After the split, the phase fluctuations in each cloud evolve independently. The clouds are released after a variable hold time t_{hold}, so that they expand and overlap as shown in Figure 2.2 (b) and (c). The phase of the fringes equals the relative phase between the two condensates at the time of release, resulting in flat fringes immediately after the condensate is split and wavy fringes for longer values of the hold time t_{hold}. The relative phase is determined from the resulting interference pattern and repeated measurement gives the distribution of relative phase fluctuations [30, 31]. Hence, we will build a precise picture of relaxation towards the equilibrium distribution. Furthermore, individual vortices can be detected in a single component following a period of in-plane expansion [64].

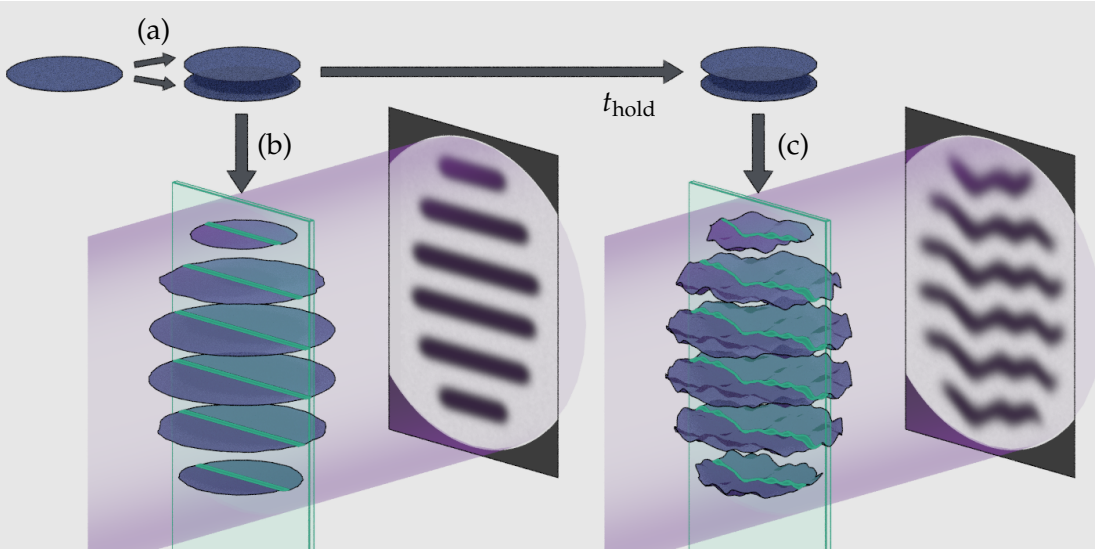

Figure 2.2: (a) Coherent splitting creates two parallel 2D quasi-condensates in a double well. (b) A resonant probe beam (purple) is absorbed by atoms in the path of the repumping beam (green) and the shadow imaged on a CCD camera. Interference arising from release immediately after the split produces straight fringes (constant relative phase). (c) Atoms held before they are released produce wavy fringes. This figure is based on one made by Elliot Bentine for Reference [33].

Measuring the probability distribution function (PDF) of the relative phase will enable us to gain more information about the equilibrium state; the characteristic function of this distribution is expected to be universal at the critical point [30, 31]. Below we list different objectives that will be implemented on our experimental apparatus.

2.2.1 *Relaxation of a Two-Dimensional Gas after Coherent Splitting*

We will investigate the relaxation of relative phase after the split and compare it with a theoretical study of a similar scenario for untrapped gases [47].

We will use our RF-dressed double-well potential to implement splitting of 2D quantum gases and verify the coherence using absorption images of the interference fringes. Using matter-wave interferometry, we will observe the time evolution and study the mechanisms described above. In particular, we will address questions about whether thermalisation in two dimensions takes place via prethermalisation to an intermediate long-lived state.

2.2.2 *Dynamically Crossing the Kosterlitz-Thouless Phase Transition*

A cloud of atoms that is initially a superfluid, below the BKT critical point, can be split such that the two resultant clouds have densities and energies that lead them to cross the phase transition as they thermalise. The NEQ clouds created by the splitting are 'superheated superfluids', obtained by changing density rather than rapid heating. This provides a very clean way to probe the NEQ dynamics, as confirmed in recent theoretical work [66]. From detailed measurements of near- and far-from-equilibrium systems around the BKT transition we will explore the extent to which NEQ behaviour is universal. We will measure the equilibrium distribution of the relative phase fluctuations, from which we can extract the quantum-mechanical PDF of the order parameter. Close to the critical point of the BKT transition, this is universal [31]. By making a comparison with the equilibrium case, this probes the existence of universality away from equilibrium.

2.2.3 *Processes with Finite Quantum Tunnelling*

For the experiments described above, the two clouds are fully coupled initially, and not coupled after separation. As an extension, we plan to make a double-well with a barrier of finite height initially or finally, or both. After separation, the initial presence of coupling alters their relaxation, specifically the final temperature of the clouds [47]. The highly controllable double-well potential enables investigation of how this initial coupling strength influences intermediate metastable states, timescales, and final states. Conversely, bringing together two independent condensates by reducing the barrier to 'reverse the quench' permits observation of the relaxation to a common phase [68, 69].

2.2.4 *A Quantum Gas in a Near-Homogeneous System*

RF-dressed trapping can be used to make quantum gases with a more uniform density across the cloud than in harmonic traps. Although not necessary for the previous objectives, it facilitates comparison with theory in some cases and adds the possibility of observing revivals [46]. Preventing atoms from moving outside a well-defined region of the trap enables a local density approximation to be used for the theoretical description. We will observe thermalisation in these traps, and compare the evolution to the harmonic case as well as theoretical models.

2.3 MATTER-WAVE INTERFEROMETRY OF A TWO-DIMENSIONAL GAS

Here we give details of how matter-wave interference can be used to observe thermalisation as proposed in Section 2.2. The goal is to determine the correlation function of the relative phase, and even the full PDF.

Interference between independent three-dimensional (3D) condensates was achieved shortly after the creation of the first BECs and demonstrated their wave-like nature [70]. More recently, coherently split BECs were re-interfered, exhibiting an interference pattern with constant phase over many runs [71]. In 1D gases, the interference pattern after coherent splitting has been used to investigate thermalisation [12]. Spatial correlations within individual 2D clouds were extracted from interference fringes to observe the BKT phase transition [63].

The interference fringes are a rich source of information about phase correlations and the state of the system. Usually only the phase of interference patterns is measured, and the effects of noise are not only ignored, but also unwanted. However, they are connected to the fluctuations in the order parameter, and can thus be analysed to receive further information about the investigated system. Full PDFs of the order parameter can be obtained [30, 31]. These PDFs for 1D gases have been used to measure the distribution of the quantum noise [72] and to provide evidence for prethermalisation [73].

We will quantify the fluctuations in the relative phase by using the fringe contrast $C(L_x, L_y, t_{\text{hold}})$ of the integrated atom density over an area with side lengths L_x, L_y as shown in Figure 2.3. For a uniform system, for $L_x \gg L_y$, and with L_y small enough that g_1 does not decay significantly over distance L_y [30, 31, 63]:

$$\left\langle C^2(L_x, L_y, t_{\text{hold}})\right\rangle \approx \frac{1}{L_x}\int_0^{L_x} dx\,[g_1(x, 0, t_{\text{hold}})]^2 \propto \left(\frac{1}{L_x}\right)^{2\alpha}, \tag{2.2}$$

which means the dependence of the integrated contrast on L_x can be described using a single parameter α. Strong phase fluctuations decrease the integrated contrast, while for gases with a constant phase it is unity, and therefore $\alpha = 0$. If $g_1(x, x')$ decays exponentially, as is the case for a gas above the BKT transition, the decay is much faster than the length scale of L_x. Thus, the integral is independent of L_x and we have $\alpha = 0.5$. At the transition temperature, α suddenly drops to $\alpha = 0.25$ for the case of a uniform gas, according to the jump in superfluid density at the transition [30, 31, 63].

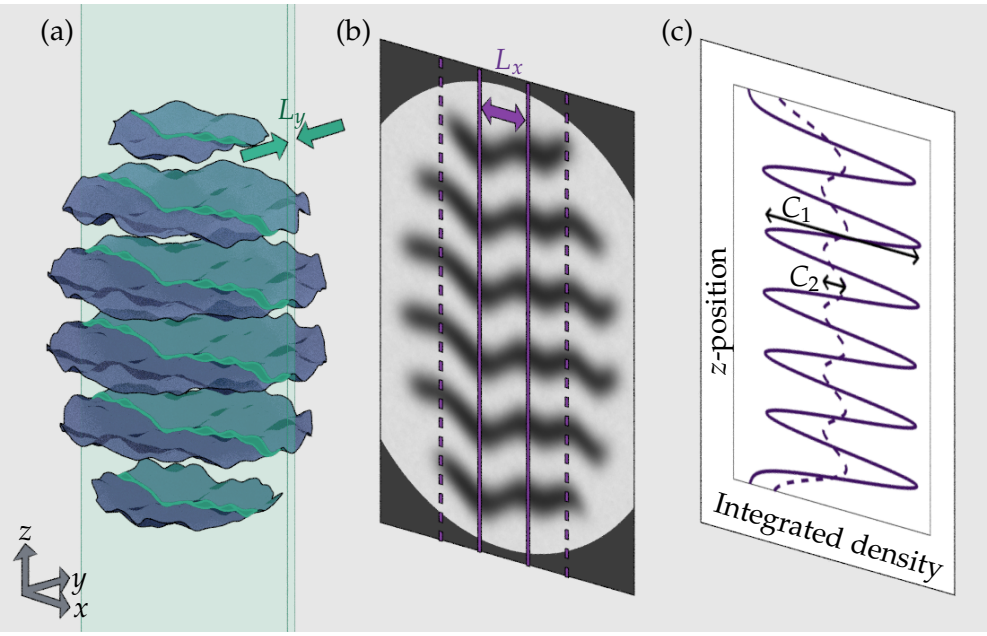

Figure 2.3: Illustration of the method for determining correlation functions of the 2D gas. (a) Atoms are optically pumped by a light sheet of thickness L_y. (b) A shadow image of these atoms is recorded, corresponding to the integrated density along y over distance L_y. Numerical integration along x over distance L_x returns the integrated atom density as a function of z. The contrast $C(L_x, L_y, t_{\text{hold}})$ of this fringe function decays with increasing L_x as shown in (c): Shorter integration length (solid lines) leads to higher contrast C_1 while longer integration length (dashed) leads to smaller contrast C_2. This decay is directly related to the phase fluctuations of the gas [63]. This figure is based on one made by Elliot Bentine for Reference [33].

Experimentally, the integration along L_y is performed by the absorption imaging. For the experiments proposed in this thesis, the clouds are (almost) spherically symmetric and a thin slice of atoms has to be selected to ensure $L_x \gg L_y$. Figure 2.3 illustrates this: a light sheet optically pumps a slice of atoms into the $F = 2$ state, and only these atoms then absorb the imaging light. Integration along L_x can be performed numerically, and thus for different lengths L_x for one image.

Many repetitions for a given t_{hold} build up the full PDF as the histogram of the contrast [31]. We will observe the evolution of this probability distribution by further series of measurements for different values of t_{hold}, and compare it to the distribution for thermal equilibrium. Since the full PDF is accessible, extracting higher-order moments of the fringe contrast is possible, which correspond to higher-order correlation functions. These contain additional information, and have been used to investigate tunnel-coupled 1D gases [44].

Discontinuities in the fringes appear if there are individual unbound vortices [63]. To obtain more information about the distribution of unbound vortices, the density can instead be measured by high-resolution imaging after an in-plane TOF expansion [64].

2.4 CONCLUSION

We have presented proposed experiments to investigate thermalisation in closed 2D quantum systems, and given an overview of related work. The remainder of this thesis will focus on how these experiments can be implemented, and investigations that were carried out to improve understanding of the trapping potentials and in turn enable trapping in two dimensions and splitting of 2D gases.

Of course, there are other ways to investigate equilibration in isolated 2D quantum systems. One such possibility is to investigate NEQ dynamics using a single sheet of atoms [74] which can be taken out of equilibrium by a periodic modulation of the trapping potential. Crossing the BKT transition can be observed by observing the momentum-distribution using matter-wave focusing techniques [75–77]. Ways to implement this technique on the apparatus presented in this thesis are currently

under investigation. This approach, while not providing the same depth of possible information, might be easier to implement than coherent splitting.

3

ULTRACOLD ATOMS IN RADIOFREQUENCY-DRESSED POTENTIALS

In this chapter, we describe RF-dressed potentials theoretically, including the use of multiple dressing frequencies for potential shaping. The dressed-atom formalism [78] is an established framework for understanding atom-photon interactions. Applications include laser cooling, cavity quantum electrodynamics, and trapping of cold atoms; the latter encompasses atoms dressed with optical [79], microwave [80] or RF [15, 81–83] radiation to either provide or shape the confinement.

The use of RF radiation in combination with static magnetic fields to create magnetic trapping potentials was first suggested in 2001 [15]. The addition of oscillating fields increases the versatility of magnetic potentials. At the same time, their advantages over optical potentials are retained: macroscopic coils create smooth, defect-free potentials as compared to corrugation from diffraction and interference effects when using laser light. Furthermore, magnetic potentials are less sensitive to alignment, and there are no off-resonant scattering processes. Although optical potentials have the ability to sculpt almost arbitrary shapes, the use of magnetic potentials proves advantageous in many practical cases. The addition of multiple dressing frequencies enables further shaping of magnetic potentials, making them an attractive alternative to optical dipole traps.

We now examine the theory of these potentials in detail, starting by describing single radiofrequency (SRF)-dressing and how this can be used to trap neutral atoms. We then describe the extension to multiple frequencies, presenting a non-degenerate basis which can be used for numerical diagonalisation.

3.1 THE DRESSED-ATOM PICTURE

The dressed-atom picture is a mathematical description of atoms interacting with oscillating fields and was first introduced in 1969 to explain the optical spectrum of atoms interacting with an RF field [84, 85]. Nowadays, it is well-known for the description of atoms interacting with laser light [79]. The atom is regarded as being 'dressed' by the field, and the combination of atom and photons of the field is described by one state [78]. The Hamiltonian describing the total system is

$$H = H_{\text{atoms}} + H_{\text{field}} + H_{\text{int}}\,, \tag{3.1}$$

with H_{atom} and H_{field} describing the energies of the atom and field independently, and H_{int} describing the interaction between the two. Spontaneous emission is negligible for the Zeeman states of the hyperfine ground state that we investigate. Where necessary, e. g. to investigate states dressed with optical frequencies, it can be incorporated by considering a reservoir of photons and a coupling term between the atom and the reservoir [**Cohen-Tannoudji1977**].

3.2 SINGLE RADIOFREQUENCY

In this section, we consider an atom at a fixed point in space, in a static magnetic field, dressed by a single RF. The static field lifts the degeneracy of the magnetic Zeeman components of the atom and the corresponding Hamiltonian can be written as

$$H_{\text{atom}} = \text{sgn}\,(g_F)\,\hbar\omega_0 F_z, \tag{3.2}$$

where $\omega_0 = |g_F|\mu_B|B_0|$ is the energy splitting due to the magnetic field $\boldsymbol{B_0} = B_0\boldsymbol{e_z}$, with the Landé g-factor g_F and the Bohr magneton μ_B. F_z is the operator projecting the spin along the vertical z direction [86]. We assume that $g_F < 0$ throughout the rest of this thesis, as is the case for the ^{87}Rb, $F = 1$ states that we investigate experimentally. The case $g_F > 0$ is analogous.

The field energy is

$$H_{\text{field}} = \hat{N}\hbar\omega_{\text{rf}}, \tag{3.3}$$

with the photon number operator $\hat{N}$ and the frequency of the field ω_{rf}. We call $H_0 = H_{\text{atom}} + H_{\text{field}}$ the combined energy of atom and field. Eigenstates of H_0 are $|N, m_F\rangle_0$, which are tensor products of Fock states of the dressing field $|N\rangle$ and the eigenstates of F_z, $|m_F\rangle$.

The interaction of an oscillating field with an atom, in the dipole approximation, is

$$V_{\text{rf}} = \frac{1}{2}(\lambda_+ F_+ a + \lambda_+^* F_- a^\dagger + \lambda_- F_- a + \lambda_-^* F_+ a^\dagger) + (\lambda_z a + \lambda_z^* a^\dagger) F_z, \tag{3.4}$$

with the coupling constants $\lambda_{\pm,z}$ that describe the coupling between the atom and the field, and account for the polarisation of the dressing field [87, 88]. $a, a^\dagger$ are ladder operators acting on the field. Assuming large coherent fields $|\alpha\rangle$, such that $\langle N\rangle = \alpha$, this interaction can be approximated as follows:

$$V_{\text{rf}} = \frac{1}{2}(\Omega_+ F_+ \widetilde{a} + \Omega_+^* F_- \widetilde{a}^\dagger + \Omega_- F_- \widetilde{a} + \Omega_-^* F_+ \widetilde{a}^\dagger) + (\Omega_z \widetilde{a} + \Omega_z^* \widetilde{a}^\dagger) F_z, \tag{3.5}$$

where we have introduced commuting, normalised raising and lowering operators

$$\widetilde{a}\,|N\rangle = |N-1\rangle, \quad \widetilde{a}^\dagger\,|N\rangle = |N+1\rangle\,, \tag{3.6}$$

and Rabi frequencies $\Omega_{\pm,z} = \lambda_{\pm,z}\alpha$ for the different polarisations of the external field. The full Hamiltonian is then

$$H_1 = H_0 + V_{\text{rf}}. \tag{3.7}$$

Its eigenenergies and eigenstates can be found using different approaches. Under the commonly-known rotating wave approximation (RWA), only those terms that resonantly couple the states are retained, and the system can be solved analytically. For a circularly-polarised RF field only the Rabi frequency $\Omega_- \neq 0$, and the RWA is exact. Numerical methods can be employed to calculate exact results for other cases, such as

a linearly-polarised field with $\Omega_+ = \Omega_-, \Omega_z = 0$, which we use in our experimental work.

3.2.1 *Circular Polarisation – Analytical Solution*

Under the RWA, or for a circularly-polarised dressing field, the interaction between the dressing field and the atom reduces to

$$V_{\mathrm{rf}} = \frac{\Omega_0}{2}\left(F_+\tilde{a}^\dagger + F_-\tilde{a}\right), \tag{3.8}$$

where, without loss of generality, we assume a real Rabi frequency Ω_0. H_1 is block-diagonal in the eigenbasis of H_0, with coupling only within manifolds with constant $k = N - m_F$. Thus for $F = 1$ it can be written as

$$H_1 = \mathbb{1}_k \otimes \hbar \begin{pmatrix} -\Delta & \Omega_0/\sqrt{2} & 0 \\ \Omega_0/\sqrt{2} & 0 & \Omega_0/\sqrt{2} \\ 0 & \Omega_0/\sqrt{2} & \Delta \end{pmatrix} + \hbar\hat{k}\omega_{\mathrm{rf}} \otimes \mathbb{1}_{\mathrm{atom}}, \tag{3.9}$$

in the basis where $|k\rangle \otimes \left(\begin{smallmatrix}1\\0\\0\end{smallmatrix}\right)$ denotes states in the manifold k with $m_F = -1$, $|k\rangle \otimes \left(\begin{smallmatrix}0\\1\\0\end{smallmatrix}\right)$ states with $m_F = 0$, and $|k\rangle \otimes \left(\begin{smallmatrix}0\\0\\1\end{smallmatrix}\right)$ states with $m_F = 1$. The frequency detuning Δ is defined as $\Delta := \omega_{\mathrm{rf}} - \omega_0$, $\hat{k}\,|k\rangle = k\,|k\rangle$, and $\mathbb{1}_k, \mathbb{1}_{\mathrm{atom}}$ are the identity operators on the manifold number and atomic state respectively. Eigenvalues are

$$\Omega(\omega_0) = \hbar\left\{0, \pm\sqrt{\Omega_0^2 + \Delta^2}\right\} + \hbar k\omega_{\mathrm{rf}} \tag{3.10}$$

with the corresponding eigenstates

$$\begin{aligned} |k = N, 0\rangle_1 &= \frac{1}{\Omega}\left(\frac{\Omega_0}{\sqrt{2}}\,|N-1,-1\rangle_0 + \Delta\,|N,0\rangle_0 - \frac{\Omega_0}{\sqrt{2}}\,|N+1,1\rangle_0\right), \\ |k = N, \pm 1\rangle_1 &= \frac{1}{\Omega}\left(\frac{\Omega \mp \Delta}{2}\,|N-1,-1\rangle_0 \pm \frac{\Omega_0}{\sqrt{2}}\,|N,0\rangle_0 + \frac{\Omega \pm \Delta}{2}\,|N+1,1\rangle_0\right). \end{aligned} \tag{3.11}$$

Note that each eigenstate of H_1 is a sum of eigenstates of H_0 of that same manifold. This is a result of the Hamiltonian in Equation 3.9 being block-diagonal, and not coupling states from different manifolds.

It may seem unnecessary to introduce a new label k for the manifold since $k = N$ above, but this is not true for half-integer spin. Furthermore, it is useful to remember that the manifold of the dressed eigenstate does not equal photon number, as the eigenstates are a superposition of states with different numbers of photons.

These eigenstates are shown in Figure 3.1 for a spin-one system with an SRF circularly-polarised dressing field. States are grouped into manifolds with constant $k = N - m_F$, and states within one manifold are $\{|N-1,-1\rangle_0, |N,0\rangle_0, |N+1,1\rangle_0\}$ as well as $\{|k=N,1\rangle_1, |k=N,0\rangle_1, |k=N,-1\rangle_1\}$.

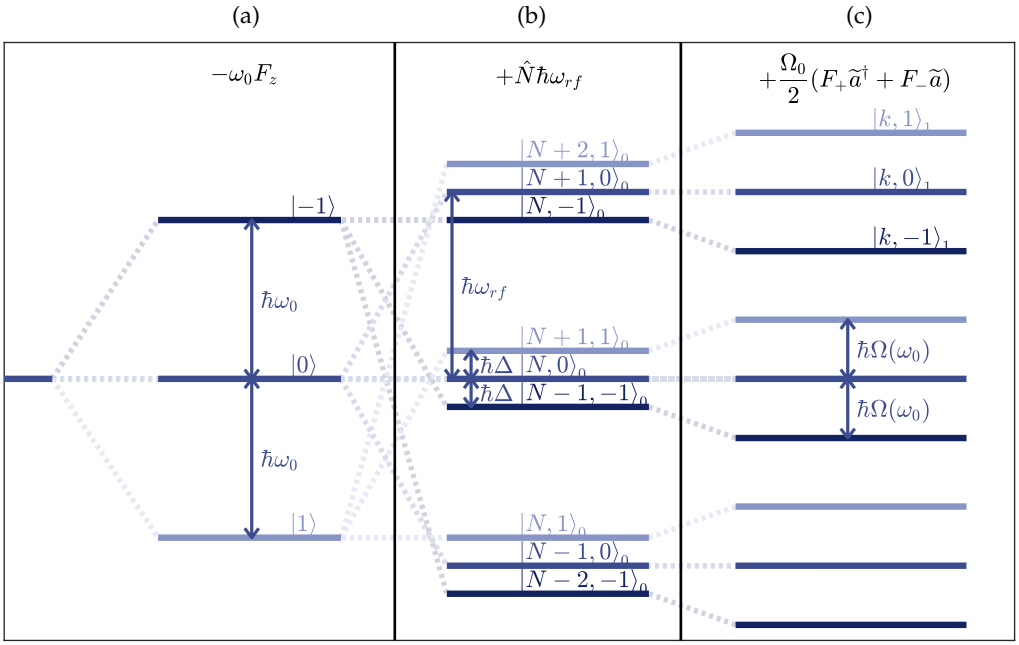

Figure 3.1: Eigensystems of various components of the Hamiltonian under consideration, for an atom with $g_F < 0$ and $F = 1$, and for $\Delta > 0$. (a) The Zeeman effect of a static magnetic field lifts the degeneracy of the three energy levels. (b) The addition of a single-frequency dressing field results in a ladder of energy levels. States belonging to one manifold with $k = N - m_F$ are now grouped together. (c) Taking into account the interaction between atoms and dressing field gives the dressed eigenstates. $\Omega(\omega_0)$ depends on ω_0 and is equal to the Rabi frequency Ω_0 on resonance.

3.2.2 *Linear Polarisation – Numerical Solution*

For any polarisation other than circular, analytical diagonalisation is not possible. Since only non-resonant terms are neglected under the RWA, the analytical results hold in first approximation even for a linearly-polarised field where $\Omega_+ = \Omega_- = \Omega_0$. However, the position of minimum eigenenergy is shifted, an effect which is named the 'Bloch-Siegert shift' [88, 89]. H_1 is no longer block-diagonal and thus couples states from different manifolds. Therefore, eigenstates are now composed of states of more than one manifold.

We calculate eigenenergies numerically. The most straightforward approach is to truncate the basis, and diagonalise the resulting Hamiltonian. Alternatively, under a full semi-classical approximation, Floquet theory can be used to calculate the eigenenergies [16, 25, 90]. This is efficient and yields results to an arbitrary level of precision. Furthermore, it can easily be extended to more complicated scenarios, such as multiple dressing fields (see Section 3.3). However, because a semi-classical approximation was made that disregards the quantum nature of the photon field, the eigenstates are superpositions of m_F states but contain no information about the quantum state of the dressing field. For some situations, such as calculating resonant transitions as in Chapter 5, this information is helpful and numerical diagonalisation of the matrix is therefore preferred. Lastly, the resolvent formalism can be used to find eigenenergies [78, 91]. This yields further insights into the processes that shape the confining potential, and we will use it when calculating transitions in Chapter 5.

Since eigenstates of H_1 contain contributions from different manifolds, $k = N - m_F$ is no longer a good label for these eigenstates. It is commonly employed however, and taken as the value in the limit of circular polarisation. While this definition works in the case of a single dressing field, it is not straightforward to extend it to the case of multiple frequencies. We therefore introduce a different method of labelling eigenstates of H_1, as illustrated in Figure 3.2, in which the eigenenergies of H_1 are given by

$$H_1 \left|k, m\right\rangle_1 = \hbar \left(k\omega_{\mathrm{rf}} + m\Omega(\omega_0)\right) \left|k, m\right\rangle_1 , \tag{3.12}$$

where k now merely denotes the energy rather than the manifold and eigenstates with the same value of k are indexed by integers m such that $-F \leq m \leq F$ and separated by an energy $\Omega(\omega_0) \geq 0$. Furthermore, we choose k such that $\Omega(\omega_0) \leq \omega_{\mathrm{rf}}/2$ for integer F and $\Omega(\omega 0) \leq \omega_{\mathrm{rf}}$ for half-integer F.

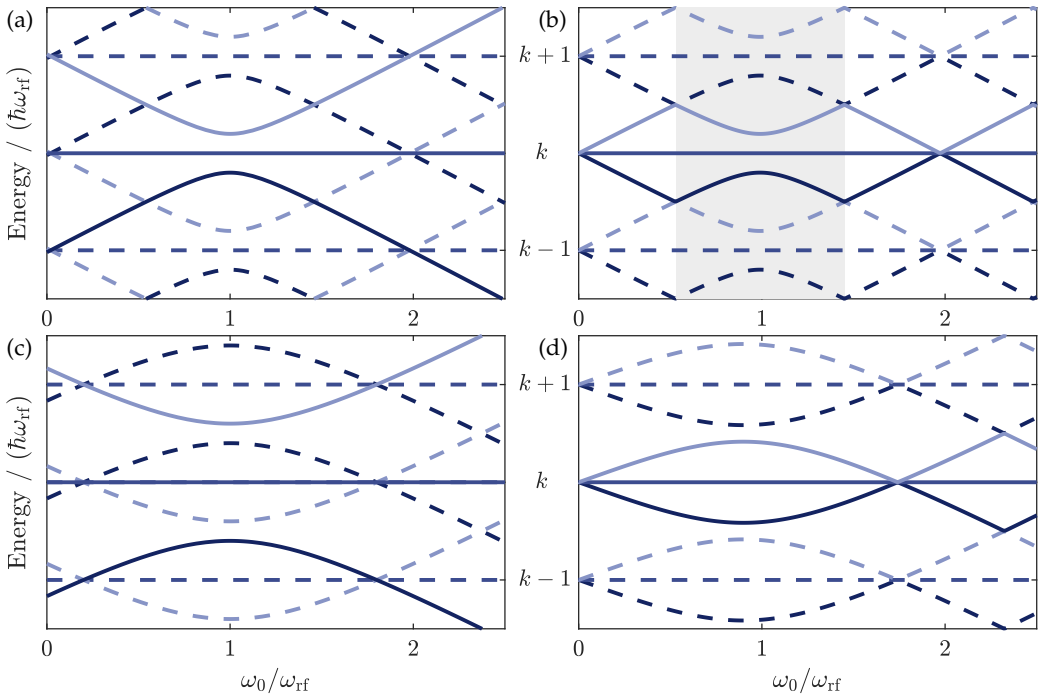

Figure 3.2: Eigenenergies of H_1 for a circularly-polarised (left) and a linearly-polarised (right) field with $\Omega_0 = 0.2\omega_{\mathrm{rf}}$ (top) and $\Omega_0 = 0.6\omega_{\mathrm{rf}}$ (bottom) as a function of ω_0. Solid lines indicate states with label k, dashed lines other states. Eigenenergies corresponding to states with $m = 1$ are light blue, states with $m = 0$ medium blue, and states with $m = -1$ dark blue. The grey area in (b) indicates values of ω_0 for which the two definitions coincide for $\Omega_0 = 0.2\omega_{\mathrm{rf}}$. For $\Omega_0 = 0.6\omega_{\mathrm{rf}}$, the labels do not coincide for any value of ω_0. Here, the differences in eigenenergies are apparent: while the minimum eigenenergy in (c) occurs for $\omega_0 = \omega_{\mathrm{rf}}$, it occurs for a smaller value of ω_0 in (d), due to the Bloch-Siegert shift [88, 89]. Furthermore, the crossing of eigenenergies at $\omega_0 = 0$ is shifted to higher frequencies by the coupling to the RF field in (c). For the case of a linearly-polarised dressing field, this shift is cancelled by the opposite shift due to the counter-rotating terms, such that the eigenenergies still cross at $\omega_0 = 0$ in (d).

Note that this defines states locally at each specific value of ω_0. As such, the state labels for a particular eigenstate will change wherever several eigenstates cross, as shown in Figure 3.2. As a result, no relation between N, m_F and k, m exists, but the calculations presented in Chapter 5 are simplified; if it is desired that the labels k, m are independent of ω_0, they can instead be defined via N, m_F of the eigenstate in the limit $\omega_0 \to 0$. Ultimately, the state labels are an arbitrary choice which does not affect the physics, provided the definition is consistent.

For the purpose of calculating transitions in Chapter 5, we numerically diagonalise the Hamiltonian including the state of the dressing field, and use the above definition of k and m. For plotting the potentials, we take the eigenenergies calculated by the Floquet code which are ordered by following each state adiabatically as the detuning is scanned. This could also be added when including the state of the dressing field, but is not necessary for our purposes. As long as they are used consistently, the different definitions of quantum numbers lead to the same results.

3.2.3 *Trapping Potential*

Since the eigenenergy of an atom depends on ω_0, a spatially varying static magnetic field can now be used to provide a trapping potential. In this thesis we use a quadrupole field, but a quadrupole-Ioffe-configuration trap has been used elsewhere [81] and the use of other field geometries is possible. Using a quadrupole field of the form

$$B(\boldsymbol{r}) = B'(x\boldsymbol{e_x} + y\boldsymbol{e_y} - 2z\boldsymbol{e_z}) \tag{3.13}$$

results in a spheroidal equipotential surface as shown in Figure 3.3 (a).

When the effect of gravity is included, atoms accumulate at the bottom. The coupling strength varies on the surface of the shell depending on the polarisation of the dressing fields and the direction of the static field compared to the dressing field [92, 93]. The two most commonly used polarisations in our experiment are circular about the vertical axis (as depicted here), which is used for preparing BECs, and linear along a direction perpendicular to the vertical axis (depicted in Figure 3.4 for multiple frequencies), which we use for most manipulations and measurements.

Figure 3.3 (b) shows the eigenenergies in the z-direction. Dashed lines indicate eigenenergies if the interaction between atom and field is neglected. These correspond to the Zeeman energies in the quadrupole field, in a ladder of states as shown in Figure 3.1 (b). Solid lines indicate the eigenenergies if the interaction is taken into

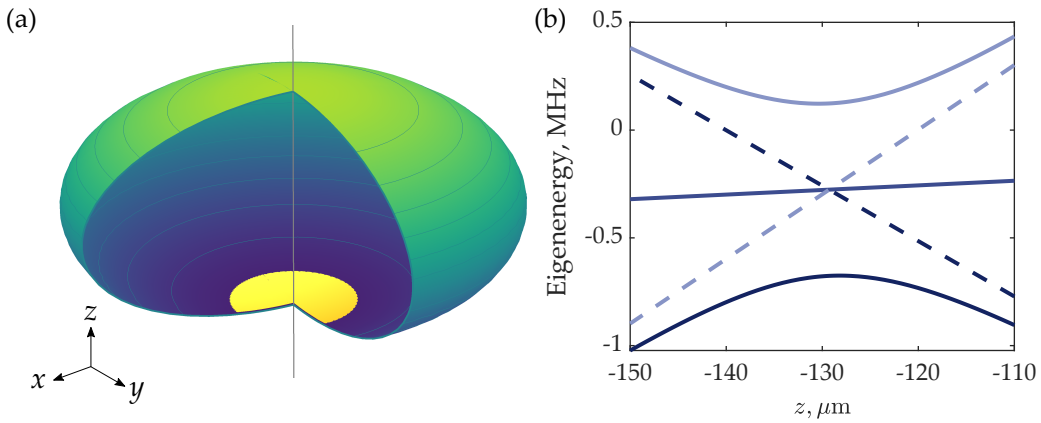

Figure 3.3: (a) Resonant spheroid for a static quadrupole field and a single, circularly-polarised, dressing field. Atoms (yellow) are trapped at the bottom of the shell trap due to gravity. The shading of the surface corresponds to the coupling strength, with maximum coupling at the bottom, and zero coupling at the top. (b) Potential energies of the three eigenstates in the vertical direction at the bottom of the shell. The eigenstates cross if the interaction is neglected (dashed lines). If the interaction is included, this becomes an avoided crossing (solid lines). The eigenenergy of the $m_F = 0$ state is equal to the eigenenergy of the $m = 0$ state. States with $m_F, m = 1$ are light blue, and states with $m_F, m = -1$ are dark blue. Atoms can be trapped at the minimum of the topmost eigenstate. The influence of gravity tilts the eigenenergies.

account, corresponding to the ladder of states shown in Figure 3.1 (c). The crossing of the initial states becomes an avoided crossing.

3.3 MULTIPLE RADIOFREQUENCIES

Adding multiple dressing frequencies increases the versatility of RF-dressed potentials. In References [16, 94] we have demonstrated the feasibility of this technique using a double-well potential. It has since been used to split a BEC and observe matter-wave interference [25].

Adding frequencies increases the number of avoided crossings and thus enables potential-shaping in a position-dependent magnetic field. As for the SRF case, the eigenenergies can be determined very accurately using a semi-classical approximation and Floquet theory [16, 25]. Here, we extend the description used in the previous section to multiple frequencies. This allows calculation not only of eigenenergies, but also the full quantum-mechanical eigenstates.

3.3.1 *The Hamiltonian*

We assume that all frequencies are an integer-multiple of a fundamental frequency ω_f, such that we have frequencies $\{n_i\omega_\mathrm{f}\}$, where the n_i are coprime integers. This is not a significant constraint, however, since although the individual frequencies are required to be rational, the rational numbers are dense in the real numbers so this does not pose a problem in reality. Furthermore, experimental considerations require that the dressing frequencies have a common fundamental frequency – if this is not the case, then sum- and difference-frequencies arising from mixing in the RF amplifiers will drive transitions to untrapped states [25, 94].

The total field energy is now $H_\mathrm{field} = \sum_i \hat{N}_i n_i \hbar\omega_\mathrm{f}$ where $\hat{N}_i$ is the photon number operator acting on the field with frequency $n_i\omega_\mathrm{f}$. The interaction of the dressing fields with the atom, analogously to Equation 3.4, is

$$V_\mathrm{rf} = \sum_i \big[\frac{1}{2}(\lambda_{i+}F_+a_i + \lambda_{i+}^*F_-a_i^\dagger + \lambda_{i-}F_-a_i + \lambda_{i-}^*F_+a_i^\dagger) + (\lambda_{iz}a_i + \lambda_{iz}^*a_i^\dagger)F_z\big]. \tag{3.14}$$

The sum over i runs over all dressing fields which are present. Operators $a_i^\dagger, a_i$ are raising and lowering operators acting on the field with frequency $n_i\omega_\mathrm{f}$.

3.3.2 *A New Basis*

In this section, we introduce a new basis to describe a multi-frequency field. The basis has been introduced by Dr. Ben Yuen, and a derivation can be found in Reference [91]. We give a brief description here.

Extending the single-frequency dressed-atom picture, a natural choice of basis is to represent the field using tensor products of Fock states. For l dressing fields, the state of the field in the Fock basis is $|N_1, N_2, \ldots, N_l\rangle$, where N_i is the photon number for the field with frequency $n_i\omega_\mathrm{f}$.

This basis is degenerate, however, and for three or more frequencies the interaction V_rf connects degenerate states in higher orders. In the case of three dressing fields with $n_1, n_2, n_3 = 1, 2, 3$, for example, the energy of the two states $|N_1, N_2, N_3, 1\rangle$

and $|N_1+1, N_2-2, N_3+1, 1\rangle$ is equal. The states are connected via the operators $\widetilde{a}_2 F_+ \widetilde{a}_1^\dagger F_- \widetilde{a}_2 F_+ \widetilde{a}_3^\dagger F_-$. No matter how large the basis is made, any truncation excludes states which are similarly degenerate. Numerical diagonalisation of the resulting matrix is problematic and leads to erroneous avoided crossings as well as states with different energies where they should be degenerate [91].

To avoid this problem, we define a non-degenerate basis $\{|N\rangle\}$, following Reference [91]. We assume that each frequency mode of the field is in a coherent state $|\alpha_i\rangle$, and the total field is the tensor product of these coherent states, $|\{\alpha_i\}\rangle$. Given $|\{\alpha_i\}\rangle$, we define a set of states $\{|N\rangle\}$ such that

$$|N\rangle := \frac{P_N |\{\alpha_i\}\rangle}{\sqrt{\langle\{\alpha_i\}|P_N|\{\alpha_i\}\rangle}}. \tag{3.15}$$

Here, $P_N : \mathscr{H}_F \to \mathscr{E}_N$ is the orthogonal projection[1] from the Hilbert space of the field, $\mathscr{H}_F$, to the subspace $\mathscr{E}_N$. The latter is defined as the set of all states with energy $N\hbar\omega_f$:

$$\mathscr{E}_N := \{|\Psi\rangle \in \mathscr{H}_F, \quad \text{with} \quad H_{\text{field}} |\Psi\rangle = N\hbar\omega_f |\Psi\rangle\}. \tag{3.16}$$

It can be shown that $\mathscr{E}_N$ is spanned by the set of all Fock states $|\{N_i\}\rangle$ with $\sum_i n_i N_i = N$ and that the subspaces $\{\mathscr{E}_N\}$ partition the Hilbert space $\mathscr{H}_F$ [91]. Therefore, the projection can be written as $P_N = \sum_{\sum n_i N_i = N} |\{N_i\}\rangle \langle\{N_i\}|$.

States $|N\rangle$ are a superposition of degenerate states, thus forming a non-degenerate basis to describe the coherent state of the multiple-frequency field [91]. The coherent product state $|\{\alpha_i\}\rangle$ can now be written in the non-degenerate basis $\{|N\rangle\}$:

$$|\{\alpha_i\}\rangle = \sum_N P_N |\{\alpha_i\}\rangle = \sum_N \sqrt{\langle\{\alpha_i\}|P_N|\{\alpha_i\}\rangle}\, |N\rangle =: \sum_N \gamma_N |N\rangle. \tag{3.17}$$

In the next section, we will calculate the matrix elements of the Hamiltonian and then diagonalise the matrix numerically, without the problems mentioned above caused by a degenerate basis.

It is worth noting that the basis $\{|N\rangle\}$ depends on the state $|\{\alpha_i\}\rangle$, and that it does not span the full Hilbert space $\mathscr{H}_F$. It is, however, sufficient to describe the coherent

1 This projection is unique according to the Hilbert projection theorem.

state of the field, and is closed under the application of photon raising and lowering operators $a_i, a_i^\dagger$ to a good approximation if $|\alpha_i|^2 \gg 1$ [91]. For a single frequency field, this basis corresponds to the standard Fock basis.

3.3.3 *The Hamiltonian in the Non-Degenerate Basis*

In order to diagonalise the Hamiltonian in the non-degenerate basis, we first calculate the matrix elements. It is easy to see that $H_{\text{field}} |N\rangle = \sum_i \hat{N}_i n_i \hbar\omega_{\text{f}} |N\rangle = N\hbar\omega_{\text{f}}$, since $|N\rangle \in \mathscr{E}_N$. Furthermore, it has been proven in Reference [91] that

$$a_i |N\rangle = \frac{\gamma_{N-n_i}}{\gamma_N} \alpha_i |N - n_i\rangle , \tag{3.18}$$

$$a_i^\dagger |N\rangle = \frac{\gamma_N}{\gamma_{N+n_i}} \alpha_i^* |N + n_i\rangle . \tag{3.19}$$

We can approximate $\gamma_N / \gamma_{N\pm n_i} \approx 1$, which is valid as long as n_i is much smaller than the standard deviation of the distribution γ_N, which is $\sigma_N^2 = \sum_i n_i^2 |\alpha_i|^2$ [91]. This corresponds to neglecting quantum fluctuations, an approximation valid for the case of classical fields which we consider. Within this approximation, we can again introduce normalised ladder operators, as in Equation 3.6:

$$\widetilde{a}_i |N\rangle = |N - n_i\rangle, \quad \widetilde{a}_i^\dagger |N\rangle = |N + n_i\rangle . \tag{3.20}$$

Analogously to Equation 3.5, the interaction with the dressing fields can then be written as

$$V_{\text{rf}} = \sum_i \Big[\frac{1}{2} (\Omega_{i+} F_+ \widetilde{a}_i + \Omega_{i+}^* F_- \widetilde{a}_i^\dagger + \Omega_{i-} F_- \widetilde{a}_i + \Omega_{i-}^* F_+ \widetilde{a}_i^\dagger) + (\Omega_{iz} \widetilde{a}_i + \Omega_{iz}^* \widetilde{a}_i^\dagger) F_z \Big], \tag{3.21}$$

with Rabi frequencies $\Omega_{i\pm,z} = \lambda_{i\pm,z} \alpha_i$. Note that for a single dressing frequency, this corresponds exactly to Equation 3.5, and the approximations in each case lead to the same result.

For a given set of frequencies, the basis can now be truncated and the Hamiltonian written as a matrix, which can be diagonalised numerically. The quantum numbers k and m are defined analogously to those for a single frequency in Section 3.2.2.

3.3.4 *Trapping Potential – Double Well*

Applying multiple frequencies to atoms in a quadrupole field leads to concentric resonant spheroids, as shown in Figure 3.4 (a). The coupling strength is calculated for a dressing field with linear polarisation along the y-axis, which results in nodes of zero coupling where the resonant spheroid intersects the y-axis [95]. We use three different frequencies to make a double-well potential [16]. The shape of the potential can be adjusted by individually changing the different amplitudes, as shown in Figure 3.4 (b) and (c). Changing the amplitude ratio of the two fields that create the two wells allows balancing them, as we will demonstrate in Section 7.1.5, and changing the amplitude of the field that creates the barrier lowers or raises it. This also draws the wells further together or pushes them further apart. Higher-order avoided crossings, as can be seen in the top-right corner, limit the depth of the potential.

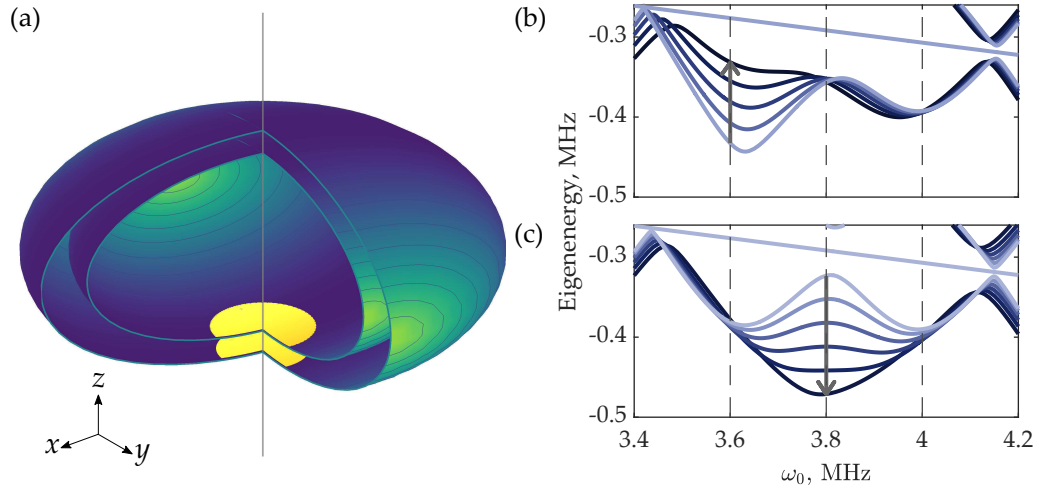

Figure 3.4: (a) Trapping surfaces for a static quadrupole field and three, linearly-polarised, dressing fields. When gravity is included atoms (yellow) accumulate at the bottom of the shell trap. The shading of the surface corresponds to the coupling strength, which is zero at two opposite nodes on the equator for a linearly-polarised dressing field. (b) and (c) Potential energies including gravitational energy of the trapped eigenstates in the vertical direction at the bottom of the shell. The atoms are dressed with frequencies 3.6, 3.8 and 4.0 MHz and amplitudes of 97, 60 and 120 kHz, in a quadrupole gradient of 199 G cm^{-1}. (b) shows eigenenergies for varying amplitudes of the field at 3.6 MHz, which forms the upper well. (c) shows eigenenergies for varying amplitudes of the field at 3.8 MHz, which forms the barrier. Light blue lines indicate small amplitudes and darker blue lines indicate larger amplitudes. Arrows indicate the effect of increasing amplitude. The frequencies of the dressing fields are indicated by vertical dashed lines.

3.4 TWO-DIMENSIONAL CONFINEMENT

To achieve the objectives proposed in Chapter 2, quasi-2D confinement has to be achieved. RF-dressed potentials are well-suited to this task, and have been used to trap a 2D gas and to observe the monopole and quadrupole modes [26].

If the vertical trap frequency exceeds the chemical potential of the trapped atoms, i. e. $\mu \ll \omega_z$, all atoms are in the ground state of the harmonic oscillator, and the geometry of the gas is quasi-2D.

The trap frequencies for atoms trapped in the state $|m\rangle$, with $|m| > 0$, of a quadrupole field dressed by a linearly-polarised RF field can be approximated as [26]:

$$\begin{aligned}
\omega_x &= \sqrt{\frac{g}{4R}}, \\
\omega_y &= \sqrt{\frac{g}{4R}}\left[1 - \frac{|m|\hbar\Omega_0}{MgR}\sqrt{1-\epsilon^2}\right]^{1/2}, \\
\omega_z &= 2|g_F|\mu_B B' \sqrt{\frac{|m|}{\hbar M \Omega_0}}\left(1-\epsilon^2\right)^{3/4},
\end{aligned} \tag{3.22}$$

where $\Omega_0 = \Omega_+ = \Omega_-$ is the coupling strength at the bottom of the shell. Note that as $\Omega_0 \to 0$ the gap closes and the trap will cease to exist. $\omega_{x,y}$ are the trap frequencies in two perpendicular radial directions with the y axis aligned with the direction of the linear polarisation. The atomic mass is M and g is the gravitational acceleration. Furthermore

$$R = \frac{\hbar\omega_{\mathrm{rf}}}{2|g_F|\mu_B B'}\left(1 + \frac{\epsilon}{\sqrt{1-\epsilon}}\frac{\Omega_0}{\omega_{\mathrm{rf}}}\right), \tag{3.23}$$

$$\epsilon = \frac{Mg}{2m_F|g_F|\mu_B B'} \tag{3.24}$$

where R is the vertical distance from the centre of the quadrupole field to the potential minimum including the effect of gravity. The trap frequencies are obtained by Taylor-expanding the trapping potential and extracting the second-order terms, and are valid for $\epsilon \ll 1$, i. e. if the force of the magnetic field gradient exceeds the force of gravity. For circular polarisation both radial trap frequencies are equal and correspond to ω_y in Equation 3.22, with $\Omega_0 = \Omega_-$, and $\Omega_+ = 0$.

A higher quadrupole gradient and a smaller Rabi frequency lead to tighter confinement in the vertical direction, that is $\omega_z \propto B'/\sqrt{\Omega_0}$. The dressing frequency has no effect on ω_z.

So far, we have neglected atomic motion. As atoms move in the dressed potential, their internal states must follow the eigenstate adiabatically[2] to remain trapped. The probability of the eigenstate changing non-adiabatically depends on how quickly it changes with time, and therefore increases for increasing velocities, or larger changes with distance. This is a well-known mechanism called Landau-Zener loss [96, 97] and has been investigated with regards to RF-dressed potentials [98, 99].

As we increase the vertical trap frequency to achieve 2D confinement, this non-adiabatic loss increases due to a number of reasons: Firstly, as trap frequencies are increased, atoms travel faster as they traverse the trap minimum, and this transit occurs more often, leading to an increased loss probability. Secondly, the Rabi frequency needs to be decreased and the quadrupole gradient increased to achieve tighter confinement. Both of these lead to larger changes of the eigenstate for a given distance, thus further increasing the loss rate.

While these losses provide a lower limit on Rabi frequencies, and upper limit on the quadrupole gradient that can be used, they do not prevent trapping of 2D clouds. This has been demonstrated in Reference [26], in a dressed quadrupole with a gradient of $216\,\mathrm{G\,cm^{-1}}$ and a Rabi frequency of the dressing field of 27.7 kHz, leading to $\mu \sim 0.2\hbar\omega_z$.

3.5 CONCLUSION

In this chapter we have described the theoretical foundation of RF-dressed potentials for the purpose of trapping ultracold atoms. We have introduced the dressed-atom picture and calculated eigenenergies and eigenstates for the case of a single dressing field. We have then described a basis that can be used for numerical diagonalisation in the case of multiple dressing frequencies, and given an example of a potential for

2 For this reason, dressed potentials are sometimes called adiabatic potentials.

the case of three frequencies. Finally, we have elaborated how 2D confinement can be achieved using RF-dressed potentials.

4

EXPERIMENTAL APPARATUS

In this chapter, we detail the experimental implementation of RF-dressed potentials and explain how it will be used to achieve the measurements proposed in Chapter 2. RF-dressing provides smooth potentials which are well-suited to trapping ultracold atoms in 1D and 2D geometries [26, 125]. We have recently demonstrated the addition of multiple frequencies to further shape the confinement by trapping atoms in two parallel sheets [16]. This constitutes a promising platform to perform the proposed experiments, and important advantages of the implementation of RF-dressed potentials include:

- The dimensionality of the gas can be transformed between two and three dimensions to study the crossover between these regimes. It has been shown that RF-dressed potentials are extremely useful for studying low-dimensional quantum gases [26, 125].

- They provide the inherent stability required to split a cloud of atoms whilst preserving the phase coherence, as shown in 1D systems [**Hofferberth2007b**]. Our highly controllable double-well potential [16] enables coherent splitting of 2D clouds with a chosen population ratio and distance between clouds.

- We use macroscopic coils to generate very smooth RF fields with extremely low heating rates; a value of 4 nK/s was measured in a trap similar to ours [26]. This is much lower than for atom chips (e. g. $\sim$ 200 nK/s for 1D experiments in Reference [12]) thus our potentials are excellent for measuring intrinsic quantum evolution and thermodynamics.

- Quartic potentials can be made using specific combinations of static and RF field amplitudes to create nearer homogeneous gases. A dipole potential can be added to improve homogeneity and shape the radial confinement.

In this chapter, we describe the implementation of RF-dressed potentials on our experimental apparatus. A general background on ultracold atoms can be found in References [86, 101], with more details on the experimental apparatus in References [25, 92–94]. Here, we give a brief description, with a focus on those elements that are essential for the experiments proposed in the previous chapter. We describe an optical dipole trap that has previously been built [94] and present measurements of atoms trapped in the combination of optical and RF-dressed potentials.

4.1 MAKING BOSE-EINSTEIN-CONDENSATES IN SHELL TRAPS

The vacuum system consists of two chambers: ^{87}Rb atoms are loaded in the first, into a pyramid magneto-optical trap (MOT) [102] from background vapour. A differential pumping tube separates the high-vacuum MOT chamber from the second chamber, the 'science cell', a glass cell at ultra-high vacuum. After loading, the atoms are transported to this second chamber, where they are further cooled to make a BEC. Here, we describe these steps in more detail. In the following sections, we describe how the trapped atoms can then be manipulated further to investigate the specific questions we are interested in, and how the clouds are imaged.

The light for the MOT comes from a tapered amplifier, which is seeded by light with frequencies corresponding to the cooling and the repumping transitions[1]. The light for driving the cooling transition is provided by an injection-locked diode laser, seeded by an external cavity diode laser (ECDL). The output of the latter is also used for absorption imaging, and its frequency can be changed throughout the sequence. Both this and the 'repumping laser' are ECDLs which are offset-locked to a master laser. The master laser is another ECDL which is itself locked to the $F = 2 \rightarrow F' = 3$ 'cooling' transition of ^{87}Rb using modulation transfer spectroscopy.

1 The energy level diagram, corresponding energy differences and further useful values for ^{87}Rb can be found in Reference [103].

The next stage of the experimental cycle is transporting the atoms to the science cell. To this end, we first perform a compressed-MOT stage to decrease the temperature and density of the cloud by increasing the detuning of the cooling light and reducing the quadrupole gradient. We then increase the quadrupole gradient and turn off the laser light, thus trapping the atoms in the quadrupole field.

A translation stage moves the coils, and thus the trapped atoms, towards the second chamber. The last stages of the transport are magnetic, and varying magnetic fields in two subsequent sets of coils push the atoms towards the centre of the final quadrupole trap.

We obtain approximately $5 \cdot 10^8$ atoms trapped in the quadrupole field at a temperature of a few hundred µK in the science cell. We then decrease the temperature using evaporative cooling [104]. Atoms with above-average energy are ejected from the trap using an RF field, and the overall temperature decreases due to rethermalisation. Evaporation is performed in three different traps consecutively, and the temperature at which atoms are transferred between traps is chosen to maximise the final phase-space density. We explain the different steps below:

In the first stage, atoms are trapped in the quadrupole field. As the temperature decreases, loss due to non-adiabatic Majorana transitions at the quadrupole node becomes significant [105], which limits the phase-space density achievable in such a trap. Therefore, we transfer atoms into a time-orbiting potential (TOP) trap, where the quadrupole field is time averaged [106]. A bias field oscillating at a frequency of 7 kHz continuously moves the field zero in a circular orbit around the position of the atoms, thus avoiding non-adiabatic loss. Evaporation in this second trap can be performed until quantum degeneracy is reached. Alternatively, after some evaporative cooling in the TOP trap, we transfer thermal atoms into a time-averaged RF-dressed potential and continue evaporative cooling there.

The RF dressing field is turned on such that the resonance is created away from the position of the atoms, resulting in the resonant spheroid described in Section 3.2 orbiting the atoms. The amplitude of the time-averaging TOP field is now reduced, until the equator of the orbiting spheroid overlaps with the atoms and atoms are loaded into the time-averaged adiabatic potential (TAAP) trap. Reducing the TOP field

amplitude further to zero loads the atoms into the shell trap. Evaporative cooling is performed at a non-zero TOP field to utilise the high geometric mean trap frequency of the TAAP trap before loading a BEC into the shell. We obtain approximately $2 \cdot 10^5$ atoms in the final cloud, with negligible thermal component.

To create all fields that are necessary for the production of a BEC in a shell trap, a number of coils are used. Figure 4.1 shows their arrangement surrounding the science cell. The macroscopic coils guarantee smooth, defect-free traps and enable low heating rates. Circular polarisation of the RF field is required for loading atoms into the TAAP trap, since the points of zero coupling lie on the equator for linear polarisation (see Figure 3.4) and cause atom loss. To produce a circularly-polarised RF field, the two perpendicular coil pairs each emit an RF field at the same amplitude, but phase-shifted by 90° [25, 94]. Once atoms are loaded into the shell trap, the polarisation of the field can be changed. Most commonly we use linear polarisation, where the amplitude of one set of coils is reduced to zero.

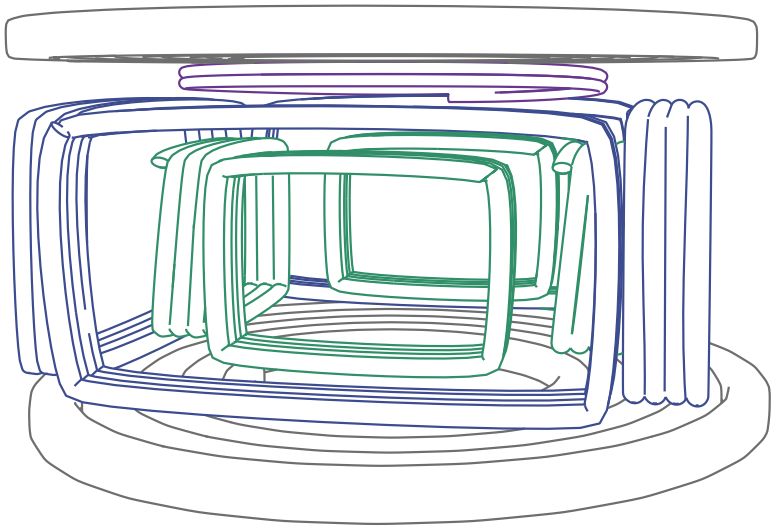

Figure 4.1: Sketch of the coil array surrounding the ultra-high vacuum science cell. Quadrupole coils are shown in grey, and provide the static magnetic field for the quadrupole, TOP and shell traps. RF coils are shown in blue and the coils generating the time-averaging field for the TOP trap are shown in green. The purple coil parallel to the quadrupole coils is used as a source for evaporative RF fields as well as RF probe fields for spectroscopy. This figure is not drawn to scale. The inner diameter of the quadrupole coils is 36 mm, and the dimensions of the RF coils are 24×29.2 mm. Further details on the coil array can be found in Reference [94]. This figure is based on one made by Elliot Bentine [25].

To generate a high enough quadrupole gradient, a current of 300 A is necessary. Previously, we used a *Magnapower SQA-30-330* power supply. The output of this

switch-mode power supply exhibited a ripple at a frequency of 396 Hz, resulting from the internal chopper. This frequency is resonant with trap frequencies of the shell traps for certain combinations of Rabi frequency and magnetic field gradient, causing parametric heating. We have since replaced this power supply with two *Delta Elektronika SM 15-400* power supply units used in parallel. Any ripples produced by these power supplies are below the detection threshold of our oscilloscope, and the parametric heating for the above parameters was removed.

The experimental control system and interlocks have enabled running the experiment remotely [25]. Consistent efforts in maintaining the experimental apparatus and improving its stability have allowed over-night running and made it possible to obtain large sets of data for the first time in this thesis, which resulted in the measurement of the detailed spectra presented in Chapter 6.

4.2 MANIPULATING TRAPPED ATOMS

In the previous section, we have explained how we obtain a BEC in the shell trap. In the next step, we manipulate the cloud, before it is released and imaged. These manipulations constitute the heart of the experimental cycle, and the experiments proposed in Chapter 2 as well as the measurements presented in the next chapters take place during this stage. The manipulations are performed using either magnetic fields or laser light, and an evolution in time can be observed by varying the hold times.

An additional RF field can be turned on suddenly to eject atoms from the trap, analogously to the evaporative RF. The loss in atom number can be observed for various frequencies to determine the energy spacing between eigenstates and thus measure dressing field amplitudes. We calculate all resonant transitions in Chapter 5 and present spectroscopic measurements in Chapter 6.

As mentioned in the previous section, most of our measurements are performed in a shell trap formed by a linearly-polarised RF field. To load atoms into such a potential, we reduce the amplitude in one set of coils generating the dressing fields to zero. This is used to measure the amplitude of the two sets of coils individually,

as well as for loading MRF-dressed potentials. It reduces the number of parameters that have to be controlled from two amplitudes and one phase per frequency to one amplitude only. This decreases time-consuming calibration and increases overall stability. It also simplifies the setup for frequency generation, since all frequencies have to be phase-locked [25].

The amplitude of the dressing fields can be changed dynamically. We normally load BECs in a circularly-polarised trap with $\Omega_0 = 2\pi \cdot 400\,\mathrm{kHz}$, load a linearly-polarised trap as described above, and then reduce the amplitude of the remaining coil. This increases the vertical trap frequencies and we have used the approach to trap condensed atoms in a potential with parameters suitable for 2D confinement. With a quadrupole gradient of $181\,\mathrm{G\,cm^{-1}}$, a dressing frequency of 3.6 MHz, and a linearly-polarised dressing field with an amplitude of 38 kHz, we achieved trap frequencies of $\omega_z = 2\pi \cdot 1.4\,\mathrm{kHz}$ and $\omega_{x,y} \simeq 2\pi \cdot 20\,\mathrm{Hz}$.

With the addition of further RFs, atoms can be loaded into an MRF-dressed potential. All amplitudes can be changed dynamically to achieve loading of the final potential with minimal atom loss and heating. We have demonstrated the first use of MRF-dressed potentials in Reference [16], and have observed matter-wave interference of a split BEC with it [25]. This will be used to split a 2D gas and observe thermalisation, and we present amplitude ramps to load a double-well potential in Chapter 7.

The addition of other fields is also possible: optical potentials can be added [94, 108], as described in Section 4.4, and microwaves can drive transitions between the hyperfine states. Furthermore, the static magnetic field can be changed suddenly, inducing a kick to the atoms. The subsequent oscillation of the centre-of-mass or size of the cloud can be used to measure trap frequencies.

Of course, many of these options can be combined, to e. g. load a linearly-polarised shell trap and then an MRF-dressed potential, before performing RF spectroscopy of the trapped atoms.

4.3 IMAGING

Absorption imaging is used to determine properties of the trapped clouds. From the images, atom number and spatial distribution of atoms can be determined directly. If the image was taken with atoms *in situ*, the trapped density distribution can be inferred. If atoms have been released from the trap and the image taken after a certain TOF, then the cloud expands as it drops [109], and the temperature of the cloud as well as the condensate fraction can be inferred. Lastly, the shape and position of the cloud gives clues to its dynamics, e. g. whether the cloud has a centre-of-mass motion or breathing mode.

To take absorption images, we first apply light from the repumping laser to the atoms, such that atoms are optically pumped from the $F = 1$ into the $F = 2$ hyperfine manifold. We then provide a quantisation axis using the TOP coils to provide a bias field and apply light resonant with the $F = 2 \rightarrow F' = 3$ transition for 15 µs when the TOP field is parallel to the imaging beam. Three images are taken with a CCD camera. The first is the shadow image of the cloud, the second is a reference image with no atoms, and the third is a dark image for background correction. The optical density and thus atom number can be inferred from the ratio of light that is absorbed using Beer's law [86].

For a trapped BEC, the atomic density is too high, such that all light is absorbed. To obtain an accurate measure of atom number, the clouds are released from the trap and imaged after 10 to 30 ms of free fall. *In situ* images are still useful to observe small atom numbers, thermal clouds, and the spatial distribution of atoms.

4.3.1 *Releasing the Clouds*

We release atoms from the RF-dressed trap in one of two ways: we turn off either the static quadrupole field or the dressing fields first. The turn-off of the quadrupole field is not instantaneous, and thus the resonant spheroids expand, changing the potential energy and eigenstates at the position of the atoms as the quadrupole field is

reduced faster than the atoms can follow. Depending on the exact shape of the current ramp, clouds may split into different m_F components in an MRF potential. This happens if a higher-order, weak, avoided crossing such as those shown in Figure 3.4 is swept through the cloud. Atoms follow different eigenstates and are thus accelerated differently by the change in the magnetic field. Additionally, atoms trapped in different potentials, or in different wells of the same MRF potential, will be accelerated differently [25].

While the splitting into m_F components is unwanted, different acceleration of different clouds is useful to distinguish the population of two different wells, with a separation that could otherwise not be resolved. We have therefore optimised the turn-off using clouds trapped in the double well potential presented in Chapter 7. We avoid splitting the clouds into m_F components, but kick atoms from the two wells differently, and can thus distinguish the two populations.

The RF dressing fields can be turned off instantaneously. Atoms are projected into the undressed Zeeman states and then accelerated by the quadrupole field depending on the state, with atoms with $m_F = 0$ falling freely under gravity. This method reduces the optical density as only the fraction of atoms projected into $m_F = 0$ are useful, but ensures that the clouds receive no initial kick. It is used to calibrate the magnification of the imaging systems [94], or to overlap clouds from two wells to observe matter-wave interference [25].

4.3.2 *Imaging Directions*

Atoms can be imaged from three directions: two of which are almost perpendicular to each other, and parallel to the optical table, and one of which is vertical, i. e. perpendicular to the optical table and in the direction of gravity [94]. Most regularly, we use the first of the horizontal imaging directions. During the measurements presented in this thesis, it has been upgraded from the system described in [94], which had a magnification of 1, to a system with a choice between a magnification of 2.7 or 1, which will be detailed in the thesis of Adam Barker [110]. The measurements presented in

Chapter 6 were taken with the previous system, while the measurements presented in Chapter 7 were taken with a magnification of 2.7, and a new camera[2].

Images in the second horizontal direction are distorted since the imaging beam passes through the curved side of the glass cell. This imaging path is mainly used for diagnostic purposes, e. g. for aligning the optical dipole trap (see Section 4.4).

The vertical imaging system has a magnification of 12 and is focused on the *in situ* position of the shell traps. It can be used for measuring radial trap frequencies, but has been designed to image the density distribution of atoms in shell traps. The goal is to either image vortices, or small numbers of atoms trapped in a lock-in lattice after TOF expansion in a shell trap [92].

For the latter, fluorescence imaging will be used – rather than imaging the shadow of the cloud on a camera, the light emitted by the atoms when irradiated with resonant light is imaged. This method is currently not used on our apparatus, but is in preparation for use with the imaging lattice [108].

4.3.3 *Imaging Interference Fringes*

To image fringes from matter-wave interference as proposed in Chapter 2, the horizontal imaging system will be used. The increase in magnification was implemented with this in mind, and the combination of larger magnification, smaller pixel size, and improved camera sensitivity will allow greatly improved resolution compared to the images taken with the previous imaging system [25]. As mentioned in Section 2.3, only a slice of atoms will be repumped and imaged to avoid blurring of the fringes due to integration along the optical axis. This will require a slight modification to the experimental setup, and two options are available: first, a repumping beam could be introduced vertically, focused with a cylindrical lens to form a thin light sheet at the position of the atoms or secondly, the setup for the optical dipole trap (described in Section 4.4) could be used with light at the repumping frequency. The latter would allow painting of arbitrary shapes for repumping, and specifically repumping of slices of varying thickness to investigate the integrated contrast in both directions. It would,

2 *Ximea MD028MU-SY*, with a pixel size of 4.54 µm.

however, be more challenging technically and prevent simultaneous use of the dipole trap.

4.4 AN OPTICAL DIPOLE TRAP

While initially magnetic traps were used for the majority of cold-atom experiments, optical potentials have been gaining popularity and are by now the most common method of confining ultracold atoms. Their main advantage is versatility in shape – lenses can be used to form laser beams into single spots and light sheets, and interference of laser beams can create lattices in one, two and three dimensions [79]. Masks can be imaged to generate fully arbitrary shapes [46, 129], and spatial light modulators provide a way to easily generate varying masks [130, 131]. The smallest length scales of these potentials are on the order of the wavelength. Disadvantages include: scattering of light by atoms leading to heating, imperfections in the potentials due to corrugations and interference, and the high laser powers being required for deep, off-resonant potentials. Furthermore, optical alignment is crucial, which imposes stringent requirements on mechanical and temperature stability. The magnetic traps utilised in this thesis are less general, but are stable over time and less costly. With the addition of multiple frequencies, they satisfy most of our requirements.

However, as mentioned in Chapter 2, in the later stages of the planned experimental scheme it is desirable to shape the radial potential, e. g. to make it homogeneous. Other scenarios are possible, such as investigating the effect of boundary conditions on vortex formation and thermalisation. While it is possible to find a combination of static and RF fields to make the potentials quartic in the radial direction, the easiest way to achieve the required radial shape is by using the dipole potential of a vertical laser beam to 'paint' on the sheets of atoms. Using a blue-detuned wavelength to create a repulsive potential allows boundaries to be drawn and atoms trapped in regions with low intensity, thus retaining the small heating rates of the underlying magnetic potentials. A red-detuned dipole trap, on the other hand, forms a dimple in the shell potential to aid evaporative cooling in the trap, and to paint other attractive potentials on the shell surface in which atoms can be trapped.

An optical dipole trap has been combined with RF-dressed potentials previously, to trap atoms in a ring on the surface of the shell, sandwiched between two blue-detuned light sheets [132]. Here, we present the first results of trapping atoms in a combination of a red-detuned dipole trap and an RF-dressed potential[3].

4.4.1 *The Setup*

We use a laser beam aligned in the vertical direction, parallel with gravity, for the dipole trap. The optical setup and steps for alignment are described in detail in the thesis of Tiffany Harte [94]. The light is overlapped with the imaging beam for the vertical imaging, but proceeds in the opposite direction, that is from bottom to top. It passes through the objective lens [133] and is focused to a spot with a waist of 1.6 µm at the location of the atoms.

Before entering the objective, the beam passes through an acousto-optic deflector (AOD). A laser beam going through an AOD is deflected from its initial path by an angle which depends on the driving frequency. If driven by multiple frequencies, several beams are produced. These beams are then imaged onto the cloud of atoms such that the beam is focused, and the beam angle resulting from the AOD is converted into a spatial translation. Therefore, beams generated by different AOD driving frequencies are imaged onto different positions of the cloud. The AOD allows deflection in two directions, such that 2D shapes can be painted on the surface of the shell trap.

Two methods for potential shaping are possible: first, if the frequencies driving the AOD are changed dynamically, the beam position is scanned. This can be used to paint arbitrary shapes onto trapped atoms [134], only limited by the finite update rate – the painting has to be fast enough such that atoms see an averaged potential [135]. Secondly, if several frequencies drive the AOD simultaneously, several beams are diffracted at different angles. This approach has been used to trap individual atoms in tweezers [136] and the arrays of 51 trapped atoms have been used for quantum simulation [137]. In contrast, if beams are created such that they overlap,

3 After submission of this thesis, the combination of a red-detuned dipole trap with RF dressing was reported in Reference [**Sinuco-Leon2019**].

a static potential can be shaped, such as a flat-top potential or asymmetric double-well [138]. Of course, both methods can be combined such that several spots are time averaged simultaneously. For both cases, the potentials experienced by the atoms can be changed dynamically.

For the previous work, a free-running diode laser at 830 nm was used. This was replaced with light from a Ti:Sapphire laser for the measurements presented in this thesis, providing higher optical power. While this is useful for alignment, the diode laser provides sufficient power for trapping atoms once the system has been optimally aligned.

We follow the initial alignment procedure described in Reference [94], and use light resonant with the repumping transition. We use this light just before absorption imaging, such that instead of optically pumping all atoms into the state with $F = 2$, only those in the path of the dipole beam are optically pumped. Once the imaging beam is applied, only those atoms absorb the light and the shadow image reveals the position of the beam for those regions that are occupied with trapped atoms. When illuminating a large thermal cloud released from the quadrupole trap, the relevant part of the beam is clearly visible. Using the two horizontal imaging directions described in Section 4.3.2, the beam can thus be aligned to the position of the atoms, as well as parallel to gravity (and thus perpendicular to the shell surface) [94].

Following this alignment, we account for the difference in chromatic shift by adjusting a lens in the optical setup to approximately focus the dipole trap onto the same position as we had the repumping light. Using several mW of light at 830 nm we then scan the driving frequencies of the AOD until we observe an effect of the dipole trap on the atoms, and further optimise the frequencies to centre the beam on the surface of the shell.

4.4.2 *Trapping Atoms*

Figure 4.2 shows four sample images of atoms trapped in a combination of the shell trap and the dipole trap. Adding the dipole trap leads to atoms being pulled into the beam, as evident by the difference between panels (a) and (b). We load atoms by

increasing the amplitude of the field driving the AOD for a constant frequency over a duration of 250 ms. For faster ramps, we observe heating of the atoms rather than loading of the dipole trap.

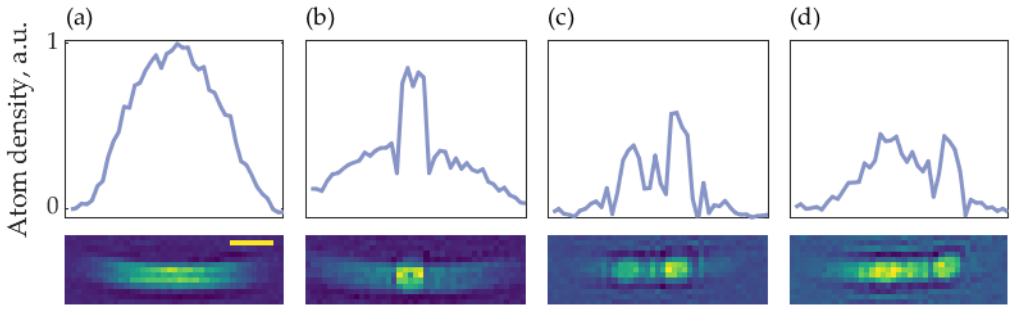

Figure 4.2: Absorption images of atoms trapped in a combination of a shell and an optical dipole trap (bottom) and integrated atomic density for the image (top). The scale bar in the bottom left image has a length of 50 µm and a height of 6.45 µm, and the scale is the same for all images. (a) Atoms trapped in the shell with no dipole trap applied. (b) A single dipole trapping beam pulls atoms to the centre of the trap. (c) Two separate beams trap atoms at different locations of the shell trap. (d) Four beams generate an asymmetric double-well potential on the surface of the shell trap.

Figure 4.2 (c) shows an example of atoms being trapped in two different beams of the dipole trap, with driving frequencies of 50 MHz and 53 MHz. The two frequencies are produced by two channels via direct digital synthesis (DDS) and combined with a splitter before the signal is amplified and then drives the AOD. Since the number of available channels is limited, for patterns with more frequencies we use two channels and then toggle between different frequencies. For the image displayed in Figure 4.2 (d), the amplitudes of two frequencies at 53 MHz and 53.5 MHz are increased, alternating with two frequencies which are initially turned on at 50 MHz and 50.5 MHz and then swept to 48.5 MHz and 52 MHz as their amplitude is increased. The atoms are trapped in the resulting time-averaged asymmetric double-well potential. The frequency ramps ensure that atoms are distributed throughout the full potential.

We are limited by the available update rate of the DDS – since the dipole trap frequencies are on the order of kHz, the time averaging has to be at least an order of magnitude faster. This prevented further investigation at the time, but is not a fundamental limitation. The maximum update rate we could use was 450 kHz, resulting in a toggle-frequency of 3 kHz.

4.4.3 *Next Steps*

Before further detailed investigations on potential shaping, the alignment of the dipole trap has to be improved, and the trap characterised. Currently, the focus of the beam is only approximately aligned: it was moved by the predicted chromatic shift between 780 nm and 830 nm. Further alignment is necessary to ensure that the focus of the beam is well-overlapped with the bottom of the shell trap.

In order to do this, trap frequency measurements of the dipole trap need to be performed, the alignment of the focus varied, and the measurements repeated to find the maximum trap frequencies and thus minimum beam waists. Once this alignment has been performed, the waist of the focus can be determined by comparing expected with measured trap frequencies. Once the dipole trap has been fully aligned and characterised, further investigation into potential shapes can be conducted.

4.5 CONCLUSION

In this chapter, we have described the experimental implementation of RF-dressed potentials for the purpose of trapping ultracold atoms. We have given an overview of how we create BECs in an RF-dressed trap and explained how we release the clouds and subsequently image them.

We have argued that our experimental apparatus is well-suited to carrying out the experiments proposed in Chapter 2. We have already trapped a quasi-2D gas (with $\omega_z = 2\pi \cdot 1.4\,\mathrm{kHz}$), and have demonstrated splitting a 3D BEC [25]. It remains to combine the two and to coherently split a 2D gas. The versatility of the MRF-dressed potentials makes it possible to have the second cloud of atoms trapped in a 3D trap. This could serve as a constant phase reference and relax the technical requirements.

Currently, the main limitation both for trapping 2D gases and splitting a cloud is atom loss induced by RF noise. This is investigated in detail in Chapters 5 and 6. In Chapter 7, we demonstrate an alternative method of splitting a gas which circumvents some of these problems.

Improvements to the experimental apparatus have allowed running the experiment for extended periods of time, and reduced the time per sequence, thus allowing the measurement of detailed spectra as described in Chapter 6. This means that we will be able to collect enough statistics for determining PDFs of the relative phase, and achieve the goals set out in Chapter 2.

We have demonstrated atoms trapped in a combination of an RF-dressed trap and a red-detuned dipole trap for the first time. While an optical dipole trap and a shell trap have been combined previously [132], a blue-detuned laser beam was used in this case, such that atoms were trapped in regions of very low optical power. In contrast, we trap atoms in the region of high optical power. Following the proof-of-principle presented here, further alignment and characterisation is necessary to pursue this promising avenue of potential shaping.

Uses of the dipole trap are manifold: it has originally been designed to trap a small number of atoms in an elliptical potential and induce fast rotation to observe the fractional quantum Hall effect [94]. Since arbitrary shapes can be painted on the surface of the shell, experiments using other shapes are possible, such as observing tunnel decay out of an asymmetric double-well [139].

In the context of the experiments proposed in this thesis, the red-detuned beam can be used to make homogeneous traps of varying shapes to investigate boundary effects on thermalisation of 2D gases. The minimum energy required to unbind vortices depends on the shape and size of the cloud. Additionally, the shape of the potential may affect whether the dynamics of phase fluctuations are chaotic, thus directly leading to thermalisation. Alternatively, if resonant repumping light was used, the optical setup could be used to selectively pump a slice of atoms before absorption imaging, as discussed in Section 2.2. Lastly, the dipole trap can increase the trap frequencies in the shell trap and facilitate evaporative cooling in this trap. This could, for example, be used to first load thermal atoms into a 3-RF single well before cooling them to quantum degeneracy.

5

TRANSITIONS IN RADIOFREQUENCY-DRESSED POTENTIALS

Spectroscopy has spurred great progress in our understanding of physical systems, from the quantum-mechanical explanations of the hydrogen spectrum to measurements of the Lamb shift [111]. Precision measurements continue to illuminate the limits of our knowledge [112, 113]. In turn, the experimental tools developed from spectroscopy have advanced our ability to manipulate the external and internal degrees of freedom of atoms.

The dressed-atom picture, as explained in Chapter 3, is a well-established method to describe the interaction of atoms with radiation. Special attention has been paid to the conceptually simple case of dressing with RF fields, and the insights gained from this have contributed to our understanding of atomic physics [78]. In addition to a single dressing field, a weak probe field, that drives transitions between dressed states, is often considered [114, 115].

More recently, transitions of atoms in RF-dressed potentials have been calculated, though restricted to a single dressing frequency [100, 116–118]. Furthermore, only first-order transitions in the probe field were considered in References [100, 116, 117] and higher-order transitions were calculated only for selected polarisations of the probe field [118]. In Reference [100], RF spectroscopy was used to investigate effects beyond the RWA.

We drive RF transitions of atoms trapped in the RF-dressed potentials for two purposes: firstly, to selectively eject hot atoms during the evaporation stage (Chapter 4), and secondly to probe the energy levels of the trapped atoms [16]. In both cases, we utilise the atom loss due to atoms being driven to untrapped states. RF-induced

losses, however, can be unwanted if they are driven by RF sources outside our control, such as sidebands on the generated frequencies or noise on the power supplies.

A large number of possible transitions arise for atoms dressed with multiple fields, which further renders these potentials vulnerable to atom loss caused by RF noise. Reducing the Rabi frequencies, as is necessary to obtain small spacing between neighbouring wells and to achieve 2D confinement, moves the resonances towards lower frequencies, which are more common amongst noise sources.

Identifying which frequencies are responsible for atom loss within the apparatus allows one to search for the source of a specific frequency in the lab [25]. In order to understand possible transitions in MRF-dressed potentials, to better tackle noise sources and to understand MRF dressing in more detail, we investigate RF transitions in MRF-dressed potentials. Thus, we can make an informed decision for dressing frequencies and amplitudes, as well as to set requirements on the power supplies and frequency sources that form these traps. Our investigations have resulted in the theoretical framework presented here, which is applicable to a wide range of systems dressed by multiple frequencies.

We present the theoretical model used to calculate RF-induced transitions of atoms trapped in MRF-dressed adiabatic potentials (Section 5.1). We then describe the numerical methods used to calculate those transitions for cases that cannot be solved analytically (Section 5.2). In Section 5.3, we describe predicted resonances for dressing by single- and multiple-frequency fields and for any order of the probe field. Finally, in Section 5.4, we describe the consequence of the non-linearity of the Zeeman effect on resonances.

For a single-frequency dressing field, accounting for all possible polarisations of the probe field and higher-order transitions results in a spectrum that goes beyond the well-known Autler-Townes splitting [119]. For certain polarisations of the probe field, we identify resonances that have not been observed or predicted previously. We also investigate the more general case of multiple dressing frequencies, revealing a rich spectrum of resonant transitions that we fully characterise spectroscopically in Chapter 6.

5.1 MODEL

We consider an atom in a static magnetic field, dressed by a radiation field with one or more frequency components, as introduced in Chapter 3. Dressing the atoms leads to a ladder of energy levels, as shown in Figure 3.1. We calculate resonant frequencies and coupling strengths for transitions driven by a probe field between these dressed eigenstates.

Including the probe interaction V_p with frequency ω_p and field energy $\hat{N}_\mathrm{p}\hbar\omega_\mathrm{p}$ we obtain the following Hamiltonian, analogous to Equation 3.7:

$$H = \overbrace{\underbrace{\hat{N}\hbar\omega_\mathrm{f} + \hat{N}_\mathrm{p}\hbar\omega_\mathrm{p} - \omega_0 F_z}_{H_1} + V_\mathrm{rf}}^{H_0} + V_\mathrm{p}. \tag{5.1}$$

We have defined the operator H_0 as the sum of the energies of the fields and the atom, without interaction, and $H_1 := H_0 + V_\mathrm{rf}$, with the interaction V_rf as defined in Equation 3.21. As in Chapter 3 we assume $g_F < 0$ and $F = 1$ throughout.

Again, we assume coherent fields with a large mean photon number. Retaining (normalised) field operators, however, allows insights into the processes on a quantum-mechanical level.

The dressing field is turned on adiabatically, such that the atoms are dressed by the field and their states become eigenstates of $H_1 = H_0 + V_\mathrm{rf}$. Figure 5.1 illustrates transitions between these dressed states, driven by the probe field, which is pulsed on non-adiabatically.

To describe the dressing fields, we use the basis detailed in Section 3.3, of counting 'fundamental excitations', to avoid degenerate bare states. The state of the probe field, however, is treated separately. Since H_0 is diagonal in the original basis, and V_rf is independent of the probe field, degeneracies do not cause a problem. Eigenstates of H_0 thus can be written as $\left|N, N_\mathrm{p}, m_F\right\rangle_0$, and eigenstates of H_1 are $\left|k, N_\mathrm{p}, m\right\rangle_1$, with the index denoting which eigenbasis is used. The eigenstates are the same as introduced in Chapter 3, but include the state of the probe field.

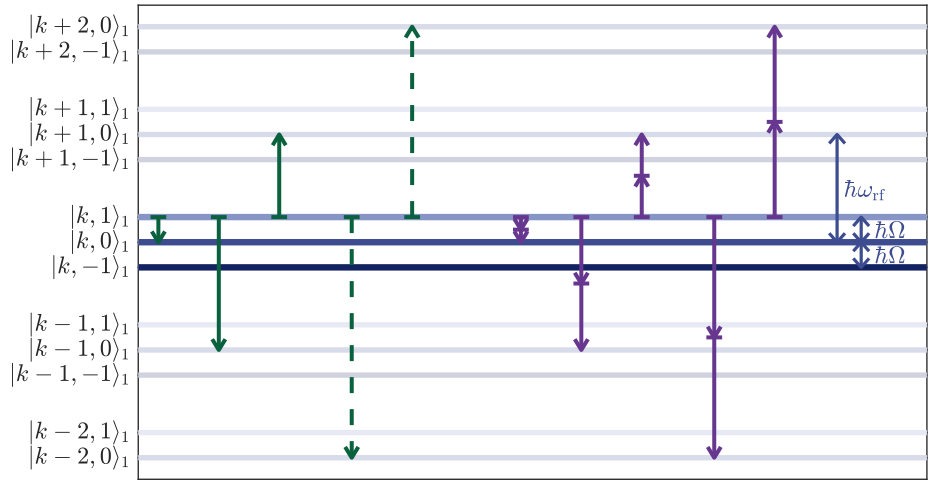

Figure 5.1: First-order (green) and second-order (purple) transitions for an atom with $F = 1$. All transitions for a circularly-polarised dressing field (solid lines) and some transitions for a linearly-polarised dressing field (dashed lines) are shown. This sketch is based on a figure originally made by Tiffany Harte for Reference [107].

Analogous to Equation 3.5, the interaction between probe field and atom is

$$V_{\mathrm{p}} = (\Omega_z \tilde{a}_{\mathrm{p}} F_z + \Omega_z^* \tilde{a}_{\mathrm{p}}^\dagger F_z) + \frac{1}{2}(\Omega_+ \tilde{a}_{\mathrm{p}} F_+ + \Omega_+^* \tilde{a}_{\mathrm{p}}^\dagger F_-) + \frac{1}{2}(\Omega_- \tilde{a}_{\mathrm{p}} F_- + \Omega_-^* \tilde{a}_{\mathrm{p}}^\dagger F_+), \quad (5.2)$$

with $\Omega_\pm, \Omega_z$ the coupling strength between the various polarisations of the probe field and the atom, and $\tilde{a}_{\mathrm{p}}^\dagger$, $\tilde{a}_{\mathrm{p}}$ normalised operators raising / lowering the number of photons in the probe field:

$$\tilde{a}_{\mathrm{p}}^\dagger \left|N_{\mathrm{p}}\right\rangle = \left|N_{\mathrm{p}}+1\right\rangle, \; \tilde{a}_{\mathrm{p}} \left|N_{\mathrm{p}}\right\rangle = \left|N_{\mathrm{p}}-1\right\rangle. \quad (5.3)$$

The order of a given transition is defined as the minimum number of creations/annihilations of probe photons required for that transition. The order of the dressing field, on the other hand, is not well-defined for transitions where atoms are resonant with the dressing field. Transitions with a large change in k become important for strong fields, which give rise to a Bloch-Siegert shift of the resonance, as has been investigated in Reference [100].

5.1.1 *First-Order Transitions*

We now calculate transitions between the eigenstates of H_1 driven by the probe field. For a transition to occur, two conditions must be met: (i) the probe interaction couples initial and final states and (ii) the probe frequency is resonant, such that energy is conserved. For first-order transitions from initial state $\left|k, N_\mathrm{p}, m\right\rangle_1$ to final state $\left|k', N_\mathrm{p}', m'\right\rangle_1$ with $m' \neq m$, these conditions are expressed as:

$$\frac{\Omega_\mathrm{eff}}{2} \left\langle m' \right| F_{\mathrm{sgn}(m'-m)}^{|m'-m|} \left| m \right\rangle = {}_1\left\langle k', N_\mathrm{p}', m' \right| V_\mathrm{p} \left| k, N_\mathrm{p}, m \right\rangle_1 \neq 0, \quad \text{and} \tag{5.4}$$

$$k'\omega_\mathrm{f} + N_\mathrm{p}'\omega_\mathrm{p} + m'\Omega = k\omega_\mathrm{f} + N_\mathrm{p}\omega_\mathrm{p} + m\Omega, \tag{5.5}$$

where we have defined an effective Rabi frequency Ω_eff, and $F_{\mathrm{sgn}(m'-m)}^{|m'-m|}$ denotes the application of the spin raising or lowering operator $|m' - m|$ times to connect states $|m\rangle$ and $|m'\rangle$.

5.1.2 *Resolvent formalism*

Higher-order transitions arise when the path taken between the initial and final state includes a number of off-resonant intermediate states. The resulting transition amplitude therefore depends on the amplitudes of these individual paths, which may interfere. To determine the frequencies of transitions and calculate their strengths, we use the resolvent formalism [78, 115], which gives an effective Hamiltonian and can be used to calculate transitions of any order. This enables understanding of the processes on the level of quantum states, e. g. to identify effects arising from the interference of individual paths. It also provides the possibility of treating the probe field quantum mechanically. We derive effective Hamiltonians between pairs of resonant states which can then be used to calculate transitions as above.

By defining the resolvent operator $G(z) = 1/(z - H)$, algebraic rather than integral equations can be used to describe the time-evolution of H. The time-evolution operator can be retrieved by a contour integral of $G(z)$. We identify a subspace $\mathscr{E}_0$ that contains states which are important in the process that is investigated – in our case

these are initial and final states, as well as all states which are close in energy. Projection operators $P, Q = \mathbb{1} - P$ project onto $\mathscr{E}_0$ and onto its complement. $G(z)$ projected onto $\mathscr{E}_0$ can then be rewritten as

$$PG(z)P = 1/(z - PH_1P - PR(z)P) \tag{5.6}$$

with the level-shift operator $R(z)$. One can identify an effective Hamiltonian acting on $\mathscr{E}_0$ from this version of the resolvent: $H_{\text{eff}} = PH_1P + PR(z)P$. The level-shift operator can be written as a power expansion in V_p:

$$R(z) = V_\text{p} + V_\text{p}\frac{Q}{z - H_1}V_\text{p} + V_\text{p}\frac{Q}{z - H_1}V_\text{p}\frac{Q}{z - H_1}V_\text{p} + \dots \tag{5.7}$$

A common approximation is to replace z with E_0, the mean energy of states in $\mathscr{E}_0$. This is valid provided the energy shift due to V_p is small compared to the energy difference of intermediate states. This is a good approximation, since we assume the probe field to be weak in comparison to the dressing fields.

The level-shift operator describes interactions between two states in $\mathscr{E}_0$ via intermediate states in the complement. The terms $Q/(E_0 - H_1)$ are propagators in frequency space. Truncating the series thus results in a cut-off in energy space, as compared to time-evolution operators in time-dependent perturbation theory, where truncation results in a cut-off in time. The i^{th} term in the expansion of $R(z)$ corresponds to a path via $i - 1$ intermediate states and matrix elements of this term describe transitions of i^{th} order in the probe field.

5.1.3 *Higher-Order Transitions*

Following the explanation above, we replace Equation 5.4 with the following to calculate higher-order transitions:

$$\begin{aligned}&\frac{\Omega_{\text{eff}}}{2}\left\langle m'\middle|F_{\text{sgn}(m'-m)}^{|m'-m|}\middle|m\right\rangle \\ &\quad = {}_1\left\langle k', N_\text{p}', m'\middle|V_\text{p}\frac{Q}{z - H_1}V_\text{p}\cdots V_\text{p}\frac{Q}{z - H_1}V_\text{p}\middle|k, N_\text{p}, m\right\rangle_1 \neq 0.\end{aligned} \tag{5.8}$$

The excluded subset $\mathscr{E}_0$ consists of initial state $\left|k, N_\mathrm{p}, m\right\rangle_1$ and final state $\left|k', N_\mathrm{p}', m'\right\rangle_1$ as well as all other states with the same energy. We therefore have

$$z \approx E_0 = \hbar(k\omega_\mathrm{f} + N_\mathrm{p}\omega_\mathrm{p} + m\Omega(\omega_0)) = \hbar(k'\omega_\mathrm{f} + N_\mathrm{p}'\omega_\mathrm{p} + m'\Omega(\omega_0)). \tag{5.9}$$

Following the explanation in Section 5.1.2, Equation 5.8 can be interpreted as follows: the initial state interacts with the probe field, followed by a free evolution under H_1, followed by another interaction and so forth, connecting initial and final states by i interaction terms for i^{th} order. The condition for energy conservation expressed in Equation 5.5 must also be fulfilled for higher orders.

In Reference [118], some higher-order transitions have been calculated. In contrast to what we present here, these were calculated under the application of the RWA for the dressing field and only a single polarisation of the probe field present, as well as a second RWA. Employing the formalism here will give further resonances that have not been predicted previously and more accurate transition amplitudes.

5.2 NUMERICAL METHODS FOR ARBITRARY FIELDS

Equations 5.5 and 5.8 can be solved if the eigenstates of H_1 are known. If H_1 can be diagonalised analytically, the calculations are straightforward and some examples are detailed in Section 5.3.1.2. Here, we detail the calculations and their implementation if H_1 has to be diagonalised numerically[1]. The following calculations have been implemented in *Mathematica*, and the code can be found on the following git repository `https://bitbucket.org/KathrinL/mrftransitions/`.

1 In the case of a single frequency and a circularly-polarised dressing field, analytical diagonalisation is possible, but for all other cases numerical diagonalisation is required – an analytic solution can also be found with some approximations [120].

5.2.1 *Partial Diagonalisation of the System*

We diagonalise the Hamiltonian $H_1 = H_0 + V_{\mathrm{rf}}$ numerically and find the expansion of the eigenvectors in the undressed basis. The eigenvectors can be written as:

$$\left|k_N, N_{\mathrm{p}}, m\right\rangle_1 = \sum_{i=-N_{\max}}^{N_{\max}} \sum_{m_F=-F}^{F} \alpha_{i,m,m_F}^{(k_N)} \left|N+i, N_{\mathrm{p}}, m_F\right\rangle_0, \tag{5.10}$$

where we again introduce the quantum number k_N, as explained in Section 3.2.2. For non-circularly polarised dressing RF, or with several dressing fields, the expansion in undressed basis states includes states from different manifolds. $N_{\max}$ restricts the maximum change in the number of dressing RF photons. It has to be large enough such that errors are negligible, but small enough for feasible calculation times.

There are $2F+1$ different eigenstates with the same value of k_N. For maximum accuracy we choose those centred about N. The factors α only depend on k_N for finite $N_{\max}$ because it matters where the 'centre' of the state is with respect to $N_{\max}$, but they do not depend on the value of k_N otherwise. Having chosen $2F+1$ states with a given k_N, we can thus drop the notation and use $\alpha_{i,m,m_F}^{(k_N)} =: \alpha_{i,m,m_F}$.

Additionally to $N_{\max}$, a further limit to accuracy is given by the machine precision involved in the calculations. We apply a threshold amplitude t, setting any $\alpha_{i,m,m_F} < t$ to zero. For maximum accuracy, t should be a few times machine precision, but calculations can be sped up significantly as this is increased. Care has to be taken when interpreting results, lest this leads to incomplete cancellation of destructively interfering amplitudes. Similarly, if the fundamental frequency is chosen smaller than necessary, numerical artefacts may lead to transitions between states spaced by $\hbar\omega_{\mathrm{f}}$ that do not exist in reality.

5.2.2 *Matrix Elements*

Matrix elements of V_{p} directly give first-order transitions between eigenstates of H_1. In section Section 5.3.1.1 we will rewrite the probe interaction in the eigenbasis of H_1

to facilitate calculations. Here, we expand the eigenstates of H_1 in the eigenbasis of H_0, using the expansion Equation 5.10, instead:

$$\begin{aligned}
&{}_1\left\langle k_{N'}, N'_\mathrm{p}, m' \middle| V_\mathrm{p} \middle| k_N, N_\mathrm{p}, m \right\rangle_1 \\
&\quad = \sum_{m_F, m'_F = -F}^{F} \sum_{i,j=-N_\mathrm{max}}^{N_\mathrm{max}} \alpha_{i,m,m_F} \alpha^*_{j,m',m'_F} {}_0\left\langle N'+j, N'_\mathrm{p}, m'_F \middle| V_\mathrm{p} \middle| N+i, N_\mathrm{p}, m_F \right\rangle_0 \\
&\quad =: \sum_{i,j,m_F,m'_F} c(m'_F, m_F, i, j, m, m', N-N', N_\mathrm{p}-N'_\mathrm{p}) \qquad (5.11)
\end{aligned}$$

The approximation that we have coherent states with large mean photon numbers is apparent in the fact that the factors α do not depend on N or k, and the factors c only depend on the difference between initial and final values of N and k. To speed up calculations for higher-order transitions, summands with $c < t$ are again set to zero.

The function c can now be calculated analytically using the coefficients α from the numerical diagonalisation of Equation 5.10. Note that this basis transformation is exact except for the cut-off at N_max and the accuracy of the numerical diagonalisation. If we use an exact basis, as for the case of a circularly-polarised dressing field, where N_max is limited naturally, then the above yields exact results.

Higher-order transitions are calculated using the resolvent formalism (Equation 5.8):

$$\begin{aligned}
&{}_1\left\langle k', N'_\mathrm{p}, m' \middle| V_\mathrm{p} \frac{Q}{z-H_1} V_\mathrm{p} \frac{Q}{z-H_1} \cdots V_\mathrm{p} \frac{Q}{z-H_1} V_\mathrm{p} \middle| k, N_\mathrm{p}, m \right\rangle_1 \\
&\quad = \sum_{|g_1\rangle_1 \in \mathscr{S}} \cdots \sum_{|g_{n-1}\rangle_1 \in \mathscr{S}} {}_1\left\langle k', N'_\mathrm{p}, m' \middle| V_\mathrm{p} \frac{Q}{z-H_1} \middle| g_1 \right\rangle_1 {}_1\langle g_1 | V_\mathrm{p} \frac{Q}{z-H_1} | g_2 \rangle_1 \\
&\qquad \cdots {}_1\langle g_{n-2} | V_\mathrm{p} \frac{Q}{z-H_1} | g_{n-1} \rangle_1 {}_1\left\langle g_{n-1} \middle| V_\mathrm{p} \middle| k, N_\mathrm{p}, m \right\rangle_1 \\
&\quad = \sum_{|g_j\rangle_1 \notin \mathscr{E}_0} \left(\prod_{i=1}^{n-1} \frac{1}{z - E_{g_i}} \right) {}_1\left\langle k', N'_\mathrm{p}, m' \middle| V_\mathrm{p} \middle| g_1 \right\rangle_1 {}_1\langle g_1 | V_\mathrm{p} | g_2 \rangle_1 \\
&\qquad \cdots {}_1\langle g_{n-2} | V_\mathrm{p} | g_{n-1} \rangle_1 {}_1\left\langle g_{n-1} \middle| V_\mathrm{p} \middle| k, N_\mathrm{p}, m \right\rangle_1, \qquad (5.12)
\end{aligned}$$

where $H_1 |g_i\rangle_1 = E_{g_i} |g_i\rangle_1$ for $|g_i\rangle_1 \in \mathscr{S}$, with $\mathscr{S}$ the set of all eigenstates of H_1. The individual matrix elements in each summand can be determined using Equation 5.11.

As described in Section 5.1.2, to determine approximate values for Equation 5.8, we use $z = E_{\left|k, N_\mathrm{p}, m\right\rangle_1} = E_{\left|k', N'_\mathrm{p}, m'\right\rangle_1}$. The projection outside the subspace is hard to implement, however, and requires knowledge of the probe frequency before it is

determined in the code. For processes where the probe frequency is resonant, this problem can be avoided: all states in $\mathscr{E}_0$ have the same energy, and we reject any term in the sum of Equation 5.12 where one of the fractions $\frac{1}{z-E_{g_i}}$ results in a division by zero[2].

Equation 5.12 is implemented in *Mathematica* for calculating the transition frequencies and amplitudes for higher orders. The infinite sum over all eigenstates collapses as the matrix elements of V_p return delta functions placing requirements on the value of $k' - k$ and $N'_\mathrm{p} - N_\mathrm{p}$. These can be solved to determine the resonant probe frequency using Equation 5.8.

With the exception of the numerical diagonalisation, the calculations detailed above are analytical. Uncertainties in transition amplitudes result from the truncation of the eigenstates as well as rounding errors arising from machine precision. This may result in some transitions with weak amplitudes being omitted, or incomplete cancellation of paths that interfere destructively. However, computational accuracy can always be increased to rule out these situations, and the predicted values for transition frequencies are always exact.

5.3 PREDICTIONS

In this section, we detail some predictions for cases which are important for our specific experimental implementation. The coupling $\Omega_{iz} = 0$ for all cases discussed here. Including this term does not change the number and frequency of allowed transitions, but only determines which parts of the probe field drive a given transition.

Dressing the atoms with a single frequency is the simplest case. This allows observation of the difference between linear and circular polarisation of the dressing RF, as well as comparison to experimental observations in a simple setting. We start with a single-frequency, circularly-polarised dressing field, and arbitrary probe polarisation (Section 5.3.1). For this case, transitions can be calculated analytically, and we compare the results to those obtained with the program described in the previous section.

2 This will cause some problems in cases where several eigenstates are close in energy, e. g. when including the non-linearity of the Zeeman effect as will be discussed in Section 5.4

We then use the program to predict the existence and location of resonances as well as their relative strengths for cases where analytical diagonalisation is not possible. We start with a single-frequency, linearly-polarised dressing field and compare the results to the circularly-polarised case (Section 5.3.2). We then present transitions for the case of dressing with multiple frequencies (Section 5.3.3). We assume that atoms are trapped in the $m = 1$ states[3] and calculate transitions for atoms to states with $m' = 0$ or $m' = -1$ which are untrapped and atoms will be lost, as we will see in Chapter 6.

5.3.1 *Single Radiofrequency – Circularly-Polarised Dressing Field*

A circularly-polarised dressing field with a single frequency ω_{rf} is the simplest case, since the interaction is confined to one manifold, as explained in Section 3.2.1. With regards to the experiment, this case is also particularly interesting: every sequence starts with atoms trapped in a circularly-polarised field, and evaporative cooling is performed in such a trap (cf. Section 4.1).

5.3.1.1 *Probe Interaction*

For an SRF, circularly-polarised, dressing field, the interaction described in Equation 3.5 reduces to $V_{\mathrm{rf}} = (\Omega_0/2)\left(F_+\widetilde{a}^\dagger + F_-\widetilde{a}\right)$, where we can assume a real Rabi frequency Ω_0. H_1 can be diagonalised exactly, and its eigenstates are admixtures of states from a single manifold (Equation 3.11).

3 As we have seen in Figure 3.2, this is not always the case. For symmetry reasons, transitions from $m = -1$ to $m' = 0$ or $m' = 1$ are the same as those from $m = 1$.

To facilitate the calculation of matrix elements, we rewrite the probe interaction V_p (Equation 5.2) in terms of operators acting on eigenstates of H_1. Details of this calculation can be found in Appendix A. We use the following operators

$$\begin{aligned}
S_\pm \left|k, N_\mathrm{p}, m\right\rangle_1 &= \hbar\sqrt{F(F+1) - (m\pm 1)m}\left|k, N_\mathrm{p}, m\pm 1\right\rangle_1, \\
S_z \left|k, N_\mathrm{p}, m\right\rangle_1 &= \hbar m \left|k, N_\mathrm{p}, m\right\rangle_1, \\
\widetilde{b}^\dagger \left|k, N_\mathrm{p}, m\right\rangle_1 &= \left|k+1, N_\mathrm{p}, m\right\rangle_1, \\
\widetilde{b} \left|k, N_\mathrm{p}, m\right\rangle_1 &= \left|k-1, N_\mathrm{p}, m\right\rangle_1
\end{aligned}$$

to describe raising and lowering of the newly-introduced quantum numbers, i. e. the manifold k and the effective spin m. We can thus write the probe interaction as

$$\begin{aligned}
V_\mathrm{p} = \frac{1}{2\Omega}\Big[&\left(\Omega_z \widetilde{a}_\mathrm{p}\left(2\Delta S_z - \Omega_0\left(S_+ + S_-\right)\right) + h.c.\right) \\
&+\frac{1}{2}\Big(\Omega_+ \widetilde{a}_\mathrm{p}\widetilde{b}\left((\Omega+\Delta)S_+ + 2\Omega_0 S_z - (\Omega-\Delta)S_-\right) + h.c.\Big) \\
&+\frac{1}{2}\Big(\Omega_- \widetilde{a}_\mathrm{p}\widetilde{b}^\dagger\left((\Omega+\Delta)S_- + 2\Omega_0 S_z - (\Omega-\Delta)S_+\right) + h.c.\Big)\Big],
\end{aligned} \tag{5.13}$$

with the frequency detuning $\Delta = \omega_\mathrm{rf} - \omega_0$. The generalised Rabi frequency of the dressing field is $\Omega^2 = \Omega_0^2 + \Delta^2$.

5.3.1.2 *Transitions*

With V_p in the form of Equation 5.13, calculating matrix elements in the eigenbasis of H_1, as is required for solving Equations 5.4 and 5.8, is straightforward. Simultaneously solving Equation 5.5 yields transition frequencies and amplitudes.

FIRST-ORDER TRANSITIONS

We calculate the following matrix elements:

$$
\begin{aligned}
&{}_1\left\langle k', N_\mathrm{p}', 0 \middle| V_\mathrm{p} \middle| k, N_\mathrm{p}, 1 \right\rangle_1 \\
&= \frac{\sqrt{2}}{4\Omega}\Big[\Big(-\Omega_+(\Omega-\Delta)\delta(k',k-1)\delta(N_\mathrm{p}',N_\mathrm{p}-1) + \Omega_+^*(\Omega+\Delta)\delta(k',k+1)\delta(N_\mathrm{p}',N_\mathrm{p}+1)\Big) \\
&\quad + \Big(\Omega_-(\Omega+\Delta)\delta(k',k+1)\delta(N_\mathrm{p}',N_\mathrm{p}-1) - \Omega_-^*(\Omega-\Delta)\delta(k',k-1),\delta(N_\mathrm{p}',N_\mathrm{p}+1)\Big) \\
&\quad -2\Big(\Omega_z\Omega_0\delta(k',k)\delta(N_\mathrm{p}',N_\mathrm{p}-1) + \Omega_z^*\Omega_0\delta(k',k)\delta(N_\mathrm{p}',N_\mathrm{p}+1)\Big)\Big],
\end{aligned}
\tag{5.14}
$$

and

$$
{}_1\left\langle k', N_\mathrm{p}', -1 \middle| V_\mathrm{p} \middle| k, N_\mathrm{p}, 1 \right\rangle_1 = 0.
$$

For the case of $m' = 0$, the matrix element Equation 5.14 is non-zero, given certain conditions on $k - k'$ and $N_\mathrm{p} - N_\mathrm{p}'$. All cases that lead to a resonant transition are illustrated in Figure 5.2. Solving Equation 5.5 yields the corresponding transition frequencies.

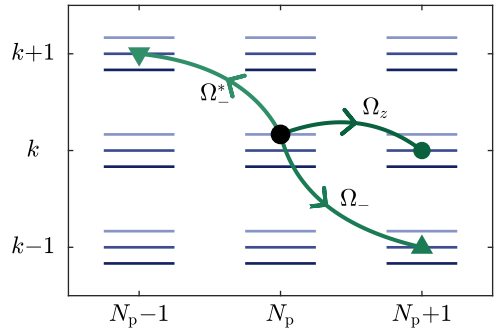

SYMBOL	ω_P	Ω_EFF
▲	$\omega_\mathrm{rf} + \Omega$	$-\frac{1}{2}\frac{\Omega-\Delta}{\Omega}\Omega_-^*$
▼	$\omega_\mathrm{rf} - \Omega$	$\frac{1}{2}\frac{\Omega+\Delta}{\Omega}\Omega_-$
	$-\omega_\mathrm{rf} + \Omega$	$\frac{1}{2}\frac{\Omega+\Delta}{\Omega}\Omega_+^*$
	$-\omega_\mathrm{rf} - \Omega$	$-\frac{1}{2}\frac{\Omega-\Delta}{\Omega}\Omega_+$
●	Ω	$-\frac{\Omega_0}{\Omega}\Omega_z^*$
	$-\Omega$	$-\frac{\Omega_0}{\Omega}\Omega_z$

Figure 5.2: First-order transitions of atoms dressed by a circularly-polarised field are illustrated on a grid with probe photon number on the x axis and manifold number on the y axis. The three possible values of m are indicated by parallel lines within each manifold. Note that the vertical axis does not correspond to energy, and the energy of individual states depends on the frequency of the probe field. The initial state is marked by a black circle, and the three possible final states by different symbols. The paths connecting these states are indicated by arrows, with the component of the probe field that drives them indicated. The corresponding transition frequencies and amplitudes are listed in the table on the right. This figure is based on a figure originally made by Elliot Bentine for Reference [107].

Different polarisations of the probe field drive different transitions. For example, a π-polarised probe field does not change the manifold number and thus causes tran-

sitions at the Rabi frequency. Circular polarisation of the probe field causes a change in the manifold number of one and thus transitions at frequencies $\omega_{\mathrm{rf}} \pm \Omega$, whereas counter-rotating terms result in transitions at negative frequencies, i. e. they couple off-resonantly, as is expected. While these terms do not play a role for first-order transitions, they do become relevant for higher-order transitions, where independent steps are driven off-resonantly.

There is no coupling between states with $m = 1$ and $m' = -1$, as was noted before [100], and is reminiscent of selection rules for spin-1 systems. In a semi-classical approximation and transforming the Hamiltonian into the rotating frame, the quantum number m can be viewed as describing Zeeman states of an effective magnetic field [25]. In this picture, the above selection rule corresponds to angular momentum conservation.

SECOND-ORDER TRANSITIONS

Next, we calculate second-order transitions and thus matrix elements of the form

$$ {}_1\left\langle k', N_{\mathrm{p}}', m' \middle| V_{\mathrm{p}} \frac{Q}{z - H_1} V_{\mathrm{p}} \middle| k, N_{\mathrm{p}}, m \right\rangle_1 . $$

This requires evaluation of the factor $\frac{1}{z-E_1}$. As described in Section 5.1.3, z is approximated as the energy of the excluded subspace $\mathscr{E}_0$, Equation 5.9. E_1 is the energy of the intermediate state, which is different from z given that any states with the same energy were excluded by the projection Q. Solving Equation 5.5 allows evaluation of $z - E_1$. All resulting transitions are illustrated in Figure 5.3 and the corresponding transition amplitudes are stated.

Transitions at $\omega_{\mathrm{rf}} \pm \Omega/2$ are driven by a circularly-polarised probe field, as was the case for transitions at $\omega_{\mathrm{rf}} \pm \Omega$ in first order. Transitions at half the Rabi frequency can be caused by either vertical polarisation (though this contribution is zero for $\Delta = 0$) or by a mix of co- and counter-rotating terms. The additional transitions at $\frac{1}{2}(\omega_{\mathrm{rf}} \pm \Omega)$ result from a mix of one circularly-polarised photon and one vertically polarised one. While the other transitions have been predicted in [118], a mix of

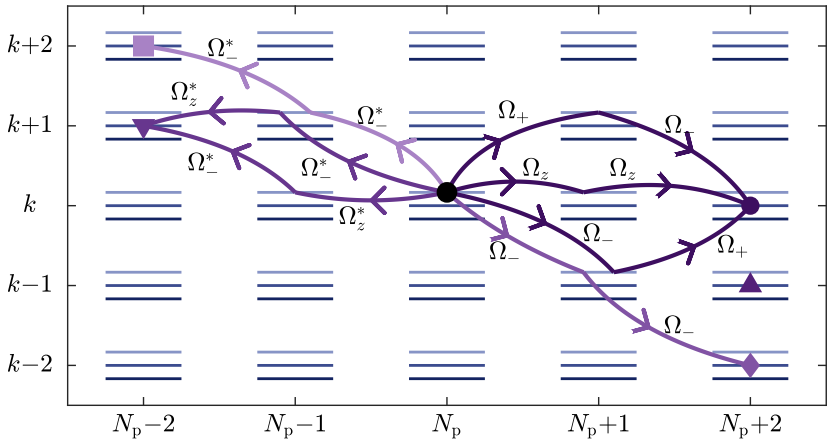

SYMBOL	ω_P	Ω_EFF
♦	$\omega_\mathrm{rf} + \frac{1}{2}\Omega$	$\frac{1}{2}\frac{\Omega_0(\Omega-\Delta)}{\Omega^3}\Omega_-^{*2}$
■	$\omega_\mathrm{rf} - \frac{1}{2}\Omega$	$-\frac{1}{2}\frac{\Omega_0(\Omega+\Delta)}{\Omega^3}\Omega_-^{2}$
●	$\Omega/2$	$\frac{2\Omega_0}{\Omega^2}\left(\frac{\Delta}{\Omega}\Omega_z^{*2} + \frac{\Omega(2\omega_\mathrm{rf}+\Delta)}{2\left(4\omega_\mathrm{rf}^2-\Omega^2\right)}\Omega_+^*\Omega_-^*\right)$
▲	$\frac{1}{2}(\omega_\mathrm{rf} + \Omega)$	$\frac{1}{\Omega^2}\left(\frac{(\Omega-\Delta)\Delta}{\omega_\mathrm{rf}+\Omega} - \frac{\Omega_0^2}{\omega_\mathrm{rf}-\Omega}\right)\Omega_-^*\Omega_z^*$
▼	$\frac{1}{2}(\omega_\mathrm{rf} - \Omega)$	$\frac{1}{\Omega^2}\left(\frac{(\Omega+\Delta)\Delta}{\omega_\mathrm{rf}-\Omega} + \frac{\Omega_0^2}{\omega_\mathrm{rf}+\Omega}\right)\Omega_-\Omega_z$

Figure 5.3: Second-order transitions of atoms dressed by a circularly-polarised field are illustrated in the same way as in Figure 5.2. For second-order transitions, there can be several paths contributing to the same transition. The paths corresponding to $\omega_\mathrm{P} = (\omega_\mathrm{rf} + \Omega)/2$ are omitted for clarity, but proceed mirrored to those for $\omega_\mathrm{P} = (\omega_\mathrm{rf} - \Omega)/2$, with the final state indicated by the upright triangle ▲. This figure is based on a figure originally made by Elliot Bentine for Reference [107].

different polarisations has not been considered previously. The amplitudes for cases that have been calculated in Reference [118] agree with our values.

As was the case for first-order transitions, there is no coupling between states with $m = 1, m' = -1$; all possible paths for such a transition proceed via a resonant intermediate state.

THIRD-ORDER TRANSITIONS

Third-order transitions are calculated in the same manner as those of second order. Some transitions and their amplitudes are shown in Figure 5.4. Transitions at $\omega_\mathrm{rf} \pm \frac{1}{3}\Omega$ appear as expected, but transitions at $\omega_\mathrm{rf} \pm \Omega$ also exist. These have the same frequency as some first-order transitions, and proceed via two off-resonant intermediate states in third order. Third-order transitions exist at probe frequencies

$\Omega/3, \Omega, (\omega_{\mathrm{rf}} \pm \Omega)/3, \omega_{\mathrm{rf}} \pm \Omega, (2\omega_{\mathrm{rf}} \pm \Omega)/3, 2\omega_{\mathrm{rf}} \pm \Omega, \omega_{\mathrm{rf}} \pm \Omega/3, 3\omega_{\mathrm{rf}} \pm \Omega$, but only the dominant ones are listed in Figure 5.4.

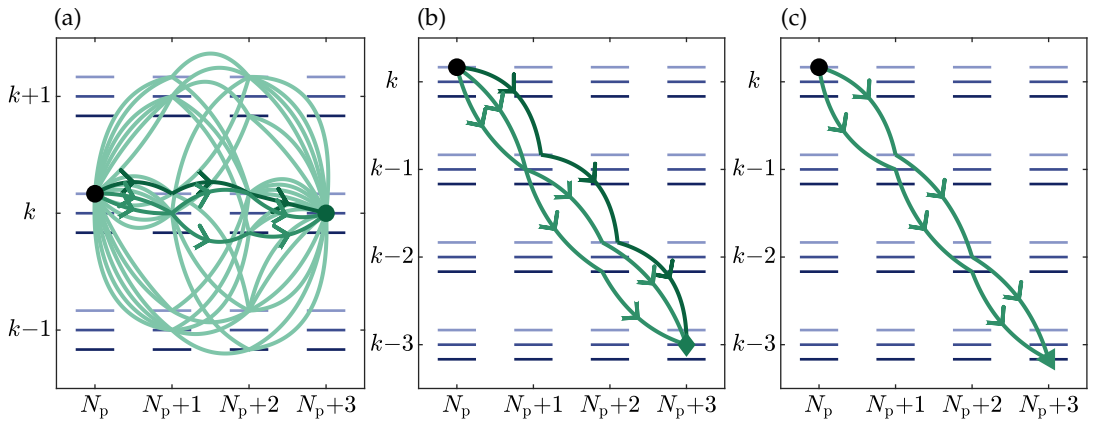

SYMBOL	ω_{P}	Ω_{EFF}	PROBE POLARISATION
	$\omega_{\mathrm{rf}} + \Omega$	$\frac{3}{2^6}\frac{(\Omega+\Delta)\Omega_0^2}{\Omega^5}\Omega_-\Omega_-^{*2}$	$\Omega_- \neq 0, \Omega_+, \Omega_z = 0$
	$\omega_{\mathrm{rf}} - \Omega$	$-\frac{3}{2^6}\frac{(\Omega-\Delta)\Omega_0^2}{\Omega^5}\Omega_-^2\Omega_-^*$	$\Omega_- \neq 0, \Omega_+, \Omega_z = 0$
♦	$\omega_{\mathrm{rf}} + \frac{1}{3}\Omega$	$-\frac{3^4}{2^7}\frac{(\Omega-\Delta)\Omega_0^2}{\Omega^5}\Omega_-^{*3}$	$\Omega_-, \Omega_+, \Omega_z \neq 0$
	$\omega_{\mathrm{rf}} - \frac{1}{3}\Omega$	$\frac{3^4}{2^7}\frac{(\Omega+\Delta)\Omega_0^2}{\Omega^5}\Omega_-^3$	$\Omega_-, \Omega_+, \Omega_z \neq 0$
●	$\Omega/3$	$\frac{9\Omega_0}{2^4\Omega^5}(\Omega_0^2 - 8\Delta^2)\Omega_z^{*3}$	$\Omega_-, \Omega_+ = 0, \Omega_z \neq 0$
◀	$\omega_{\mathrm{rf}} + 2\Omega/3$	0	$\Omega_-, \Omega_+, \Omega_z \neq 0$

Figure 5.4: Selected third-order transitions of atoms dressed by a circularly-polarised field are illustrated in the same way as in Figure 5.2. (a) Taking into account the full probe polarisation leads to 21 possible paths for $\omega_{\mathrm{p}} = \Omega/3$. Those driven purely by a vertically-polarised probe field are indicated in darker green and the amplitude is given in the table. The full amplitude, including an arbitrary polarisation of the probe field, is listed in Appendix B. Contributions neglected in Reference [118] are a lighter green than the strongest contribution. (b) For $\omega_{\mathrm{p}} = \omega_{\mathrm{rf}} + \Omega/3$, there are only three possible paths. Those neglected in Reference [118] are drawn in lighter green. (c) For $\omega_{\mathrm{p}} = \omega_{\mathrm{rf}} + 2/3\Omega$, there are two paths coupling initial and final states, with amplitudes which cancel exactly. This figure is based on a figure originally made by Elliot Bentine for Reference [107].

For transitions at $\omega_{\mathrm{rf}} \pm \Omega/3$, the effective Rabi frequency given in [118] is smaller by a factor of $8/9$ compared to our results. For a third-order transition of frequency $\Omega/3$, the results in Reference [118] do not include the term proportional to Ω_0^2. This significantly alters the dependence of the transition amplitude on detuning, with the transition not being zero, but rather maximal, at zero detuning, with two zeros at $\Delta = \pm 2\sqrt{2}\Omega_0$. These differences come from the fact that in Reference [118], only one of three paths for transition at $\Omega/3, \omega_{\mathrm{rf}} \pm \Omega/3$ was taken into account (see Figure 5.4). While the contributions of the two neglected paths have opposite sign, they do not

fully cancel due to a different energy for the second intermediate state and thus a different factor $1/(z - E_2)$.

Contrary to first and second-order matrix elements, in third order the states $\left|k, N_\mathrm{p}, 1\right\rangle_1$ and $\left|k', N_\mathrm{p}', -1\right\rangle_1$ do couple for probe frequencies $\omega_\mathrm{p} = \omega_\mathrm{rf} + 2\Omega$ and $\omega_\mathrm{p} = \omega_\mathrm{rf} + 2/3\Omega$. However, the total matrix element is still zero, since possible paths interfere destructively (Figure 5.4 (c)). This is true for any field amplitude and detuning.

GENERALISATION TO TRANSITIONS OF ANY ORDER

The above results can be generalised to describe transition frequencies for any order i in the probe field. They exist for $m = 1, m' = 0$ at frequencies

$$\omega_\mathrm{p} = \frac{\kappa\omega_\mathrm{rf} \pm \Omega}{i - 2j}, \tag{5.15}$$

with integers j, κ such that $0 \leq \kappa \leq i$ and $0 \leq j < i/2$. Here, $\kappa = |k' - k|$ corresponds to the difference between initial and final manifold and $i - 2j = |N_\mathrm{p}' - N_\mathrm{p}|$ to the difference between initial and final probe photon number. Since the action of V_rf is confined to a single manifold, V_p only couples states with $|k' - k| \leq 1$, resulting in the limit of $\kappa \leq i$. Thus, only a finite number of transitions occur for a given order, as shown for first order in [100]. This also means that transitions with a frequency of $2\omega_\mathrm{rf} \pm \Omega$ and $3\omega_\mathrm{rf} \pm \Omega$, while not resonant in first order, exist in third order, via two intermediate, non-resonant states.

No transitions between states with $m = 1, m' = -1$ exist since for an even i, there is no path via non-resonant intermediate states, and for an odd i, all existing paths cancel exactly due to symmetry reasons.

All transitions contain contributions from several orders and all these contributions have to be summed to obtain the full transition amplitude for a given probe frequency. The higher-order terms become more important as the amplitude of the probe field increases.

5.3.1.3 *Comparison to Numerical Results*

We compare the results obtained in the previous section to those returned by the program. Figure 5.5 shows the transition strengths of first- to fourth-order transitions of atoms with $m = 1$ to $m' = 0$ dressed with a circularly-polarised field.

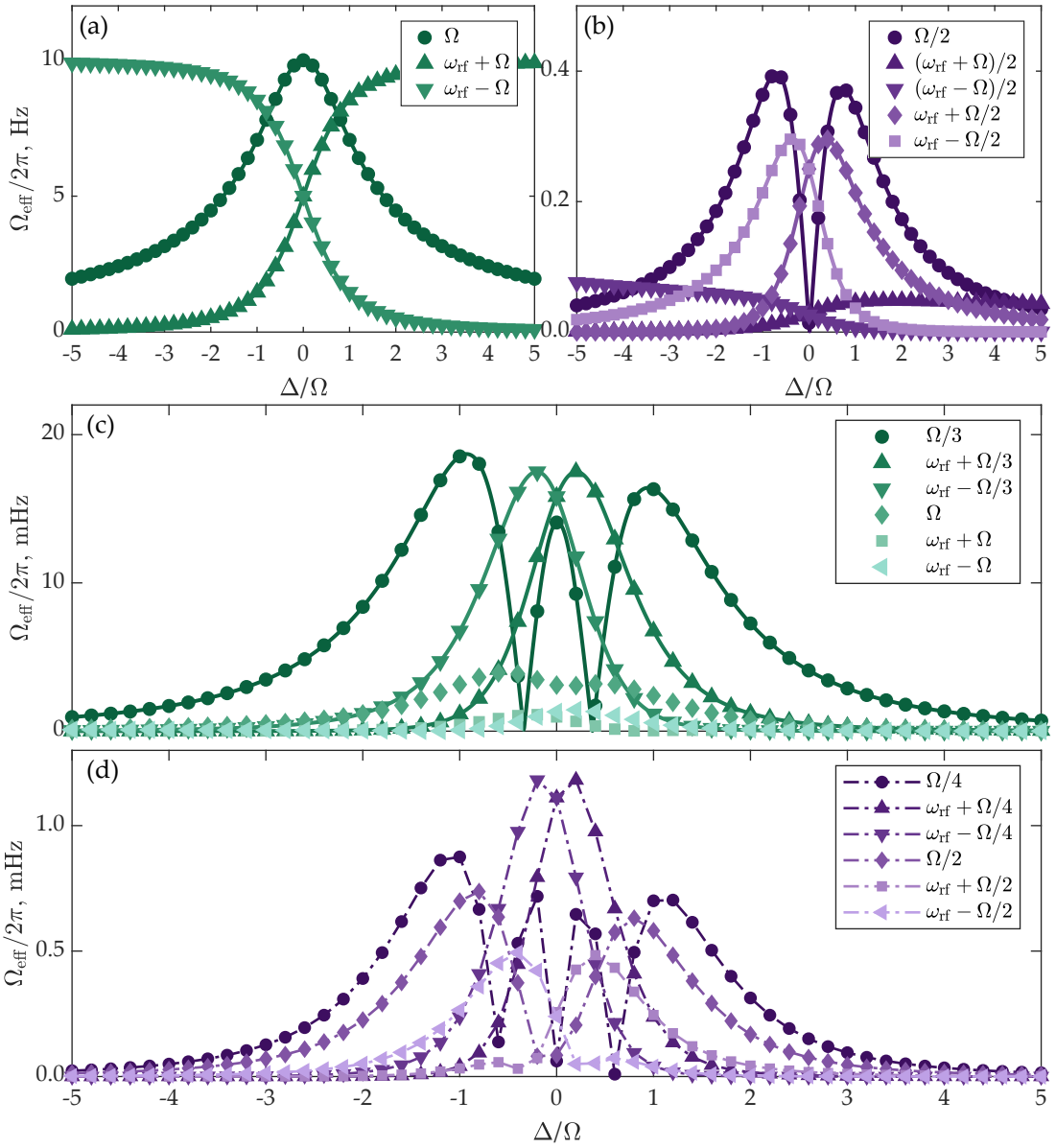

Figure 5.5: Transition amplitudes for (a) first- to (d) fourth-order transitions in a circularly-polarised dressing field with a frequency of 3.6 MHz and a Rabi frequency of 0.2 MHz, as a function of detuning Δ. The probe field is always on resonance. Results from the numerical calculation (markers) and the analytical predictions (line) for $\Omega_z = \Omega_+ = \Omega_- = 2\pi \cdot 10\,\mathrm{kHz}$. For fourth-order transitions, the markers are connected as a guide to the eye.

The theoretical and numerical predictions agree to within the precision of the calculation. The transition at $\omega_p = \Omega$ vanishes for $|\Delta| \to \infty$ while the transition strength of $\omega_{rf} \pm \Omega$ approaches a constant non-zero level as $\Delta \to \pm\infty$ and approaches zero as $\Delta \to \mp\infty$. This is as expected, since the eigenstates approach the simple Zeeman substates as $|\Delta| \to \infty$. In these limits, it is straightforward to also define the order of the dressing field [118]. However, as $\Delta \to 0$, this order is no longer well-defined. We will argue below that the change in k is a good indicator of how transition strength varies with dressing field amplitude.

Panels (b) – (d) of Figure 5.5 show the various transition amplitudes for second- to fourth-order transitions. For clarity, transitions with very small amplitudes are omitted. We observe that resonances at $\omega_p = \Omega/i$ have a vanishing transition strength at $i - 1$ different values of the detuning.

5.3.2 *Single Radiofrequency – Linearly-Polarised Dressing Field*

For a linearly-polarised dressing field, we diagonalise the Hamiltonian numerically. The commonly used RWA neglects all counter-rotating terms and therefore yields the same results as the circularly-polarised case discussed above. Otherwise, the presence of counter-rotating terms causes the dressed eigenstates to contain bare states from an infinite number of manifolds. Thus, an infinite number of possible transitions exist at any order of the probe field, although most are of negligible strength. Ultimately, transitions occur at the same frequencies as for a circularly-polarised dressing field (Equation 5.15), but with no limit on κ. Thus, many of these occur at a lower order, and are therefore stronger, when atoms are dressed by a linearly-polarised field. As the dressing field amplitude increases, these transitions can be become dominant, an effect which has been investigated in [100].

When rewriting V_p in the eigenbasis of H_1, this becomes apparent: V_p is no longer linear in $\widetilde{b}, \widetilde{b}^\dagger$ as in the case of circular polarisation (Equation 5.13). The action of V_p therefore changes the value of k of a given state by more than one, due to the non-linear terms, enabling transitions with $\kappa > i$. Furthermore, each factor of $\widetilde{b}, \widetilde{b}^\dagger$ is proportional to the dressing field amplitude, which means that for large amplitudes,

transitions with a larger value of κ become stronger than those at small κ. In the literature, κ has been called the order of the dressing field for a transition of first order in the probe field, and for a linearly-polarised SRF field [100]. For simplicity, we will continue to use this term when speaking about the 'order' of the dressing field. However, we point out that this change does not exactly correspond to a change of the number of photons in the dressing field, but rather it corresponds to a quantity in the dressed picture, and cannot be disentangled from the state of the atom.

As in the case of a circularly-polarised dressing field, we show the dependence of the transition amplitudes on detuning for first- to fourth-order transitions in Figure 5.6. Panel (a) shows first-order transitions. Those with frequencies $\kappa\omega_{\mathrm{rf}} \pm \Omega$ exist for any non-negative integer κ, but are not shown for $\kappa > 2$ as these become increasingly weak. For comparison, the analytical results for a circularly-polarised dressing field are shown in grey.

Second- to fourth-order transitions are shown in Figure 5.6 (b,e,f). The same transitions as for a circularly-polarised dressing field are shown for clarity. Transitions with higher order in the dressing field exist, but are very weak for the parameters we use. Panels (c) and (d) show the small difference between circularly- and linearly-polarised fields for first- and second-order transitions.

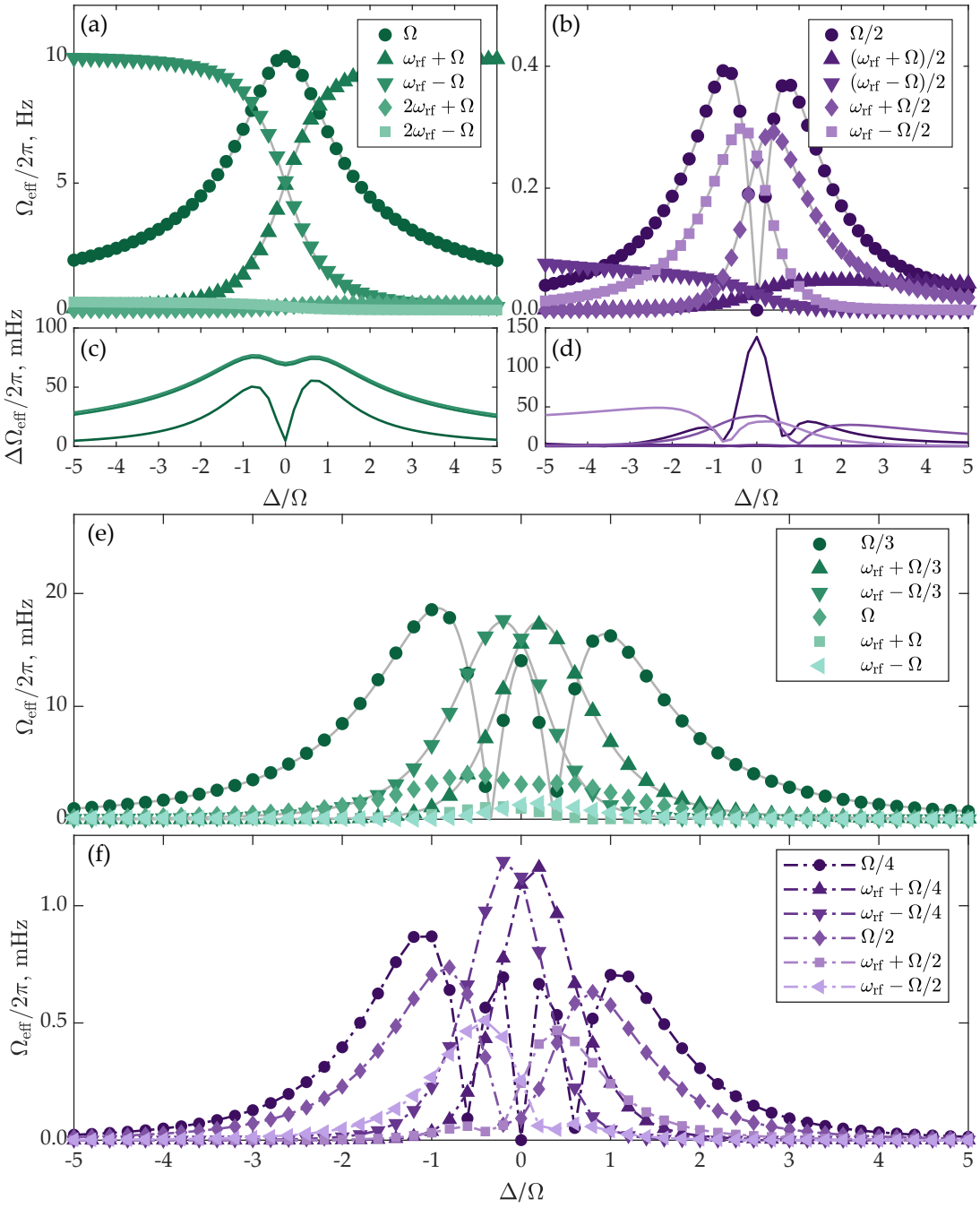

Figure 5.6: Transition amplitudes for atoms in a linearly-polarised dressing field with a frequency of 3.6 MHz and a Rabi frequency of 0.2 MHz, as a function of detuning Δ. The probe field is always on resonance. Results from the numerical calculation (marker) and the analytical predictions for a circularly-polarised dressing field (grey line) for $\Omega_z = \Omega_+ = \Omega_- = 2\pi \cdot 10\,\mathrm{kHz}$. Plots (a, b, e, f) show transition strengths for first- to fourth-order transitions. Plots (c, d) show the difference between amplitudes for linear and circular polarisation and for first- and second-order transitions respectively.

5.3.3 *Multiple Radiofrequencies*

For an SRF dressing field, the periodicity of transitions is simply the dressing frequency. For a circularly-polarised field, transitions do not simply repeat, but for an i^{th} order transition, the manifold number can change by a maximum of i. For a linearly-polarised dressing field, this change is not limited by the order of the probe field, resulting in a comb of transitions repeating with the dressing frequency.

For an MRF field, the transitions now repeat with the common fundamental between the different dressing fields, and transitions at frequencies

$$\frac{(\kappa\omega_{\text{f}} \pm \Omega)}{i - 2j} \tag{5.16}$$

exist, where $i > 0$ is the order of the transitions and $0 \leq j \leq i/2, \kappa \geq 0$ are integers. For simplicity, we only consider linearly-polarised fields here. As for the SRF case, the existence of transitions will not be different, but there will be some limits on the order for circularly-polarised fields.

As for the case of a linearly-polarised dressing field with a single frequency, the expression for V_{p} in the case of multiple frequencies contains any combination of the operators $\widetilde{b}_i, \widetilde{b}_j^\dagger$. The dominant contribution to any transition is given by the path arising from the minimum number of raising and lowering operators required, as well as their respective prefactors[4]. For example, in a dressing field at frequency $n_1\omega_{\text{f}}$, only one creation or annihilation is necessary to drive the transition for which $\kappa = n_1$. For two dressing fields at frequencies $n_1\omega_{\text{f}}, (n_1+1)\omega_{\text{f}}$, the transition at $\kappa = 1$ takes two operators ($\widetilde{b}_{n_1+1}^\dagger \widetilde{b}_{n_1} = \widetilde{b}_1^\dagger$), but the transition with $\kappa = n_1/2$ takes n_1 operators: $(\widetilde{b}_{n_1+1}^\dagger)^{n_1/2}(\widetilde{b}_{n_1})^{n_1/2} = \widetilde{b}_{n_1/2}$. Thus transitions at $(n_1\omega_{\text{f}} \pm \Omega)/(i-2j), (\omega_{\text{f}} \pm \Omega)/(i-2j)$ are strong compared to transitions at $(n_1/2\ \omega_{\text{f}} \pm \Omega)/(i-2j)$. This qualitative description explains the overall pattern of transition strengths in the experimental observations reported in Section 6.3.2 and can lead to second-order transitions surrounding the frequency $(n_1/2)\omega_{\text{f}}$ being stronger than first-order transitions at similar frequencies.

4 This is true unless several paths cancel each other, such that a different term dominates.

5.4 EFFECTS FROM NON-LINEAR ZEEMAN SPLITTING

The eigenenergies of an atom in a static magnetic field can be calculated from the Breit-Rabi formula, and the influence of deviations from linearity on dressed atoms has been investigated in [121]. The static magnetic field used in this work causes Zeeman splittings of a few MHz, compared to the hyperfine splitting of 6.8 GHz. Therefore the energies of the undressed Zeeman states can usually be calculated with sufficient precision without taking into account non-linearity. However, the asymmetry of the eigenenergies does have an observable influence on transitions that are 'forbidden' in the linear regime, analogous to a breakdown of the selection rules. We incorporate it into our calculations by introducing an additional term so that the Hamiltonian now reads

$$H_0 = \hat{N}\hbar\omega_\mathrm{f} + \hat{N}_\mathrm{p}\hbar\omega_\mathrm{p} - \omega_0 F_z - \hbar\delta_\mathrm{ZM}\mathbb{1} \otimes |-1\rangle_{0\ 0}\langle -1| \,, \tag{5.17}$$

where $|-1\rangle$ denotes the Zeeman state with $m_F = -1$ and $\hbar\delta_\mathrm{ZM}$ is the difference between the energy separation of the $m_F = -1, 0$ and the $m_F = 0, 1$ states, such that $\delta_\mathrm{ZM} = 0$ in the linear Zeeman effect. We calculate the eigenstates of $H_1 = H_0 + V_\mathrm{rf}$ numerically and find first-order transition frequencies and amplitudes as described above. A significant feature is that transitions at probe frequencies of $\kappa\omega_\mathrm{f} \pm 2\Omega$ now exist between states with $m = 1$ and $m' = -1$, whereas none are predicted for a purely linear Zeeman effect, as in [100]. These transitions are stronger at larger static fields where the non-linear Zeeman shift is increased.

To calculate higher-order transitions, states with similar, yet slightly different, energy have to be included. While this is straightforward in theory, it requires substantial modifications of our program. For the purpose of this thesis, these modifications are not necessary, since the transitions are significantly weaker compared to those presented above, and no higher-order transitions of this kind are observed in the spectra presented in Chapter 6.

5.5 DISCUSSION

We have presented a general theoretical framework to calculate transition frequencies and strengths for atoms dressed by multiple frequencies. Accounting for arbitrary polarisations and higher-order transitions provides a complete description of the spectrum. This methodology enabled us to derive analytical expressions for transition frequencies and amplitudes for the case of a single, circularly-polarised field. Numerical diagonalisation was used for cases beyond the RWA and for multiple-frequency dressing fields. Transition frequencies for any order in the probe field are given by a simple formula. Our results are consistent with previous predictions [100, 116, 118], but greatly extend these. We uncover transitions that were not predicted previously by considering an arbitrary polarisation of the probe and dressing fields as well as calculating transitions of higher order in the probe field. Formerly unknown were transitions at frequencies $\omega_\mathrm{p} = (\kappa\omega_\mathrm{rf} \pm \Omega)/(i-2j)$ where κ is not an integer multiple of $i-2j$. For a weak probe field, the strongest of these are the second-order transitions at frequencies $\omega_\mathrm{p} = (\omega_\mathrm{rf} \pm \Omega)/2$. Spontaneous emission was neglected, but could be included in our model if required, enabling investigation of an even wider range of multi-frequency phenomena.

The description of multi-frequency fields is common in non-linear optics, and it is insightful to compare this approach to our methods: in non-linear optics the amplitude of dipole oscillations is typically small, off-resonant, and at frequencies associated with the driving fields. In contrast, the multi-frequency transitions considered here can have a large amplitude but are typically slowly oscillating and are observed on resonance. This work is therefore at the opposite end of the scale of multiple-frequency effects to the standard perturbative approach in non-linear optics. These extremes can be combined with the more general theoretical methods presented in [120].

Although the theoretical framework presented here is widely applicable, we have focused on the experimental implementation of MRF-dressed potentials as described in Chapter 4, and will use these to verify the predictions presented here as described in the next chapter. To use MRF-dressed potentials for an investigation of thermalisa-

tion in two-dimensional gases, as proposed in Chapter 2, requires a reduction of the well spacing. For this, a more detailed understanding of the plethora of resonances that arises when multiple dressing fields are present is essential. In particular, our results provide a framework to understand and mitigate the loss of atoms through spurious noise when working with MRF-dressed potentials. This is also of critical importance for experiments that use many closely-spaced frequencies, such as the proposal to form a periodic potential of individually controllable wells [24].

6

RADIOFREQUENCY SPECTROSCOPY

Using RF fields to drive atomic transitions in cold atoms was first demonstrated in 1988 [122]. Since then, RF fields have been widely used to control the internal state of atoms. They can be employed to selectively eject atoms with above average energy from magnetic traps, and so achieve evaporative cooling [104]. Perhaps most famously, this technique paved the way to achieving the first BECs [123, 124] and has since become a staple of modern cold-atom experiments. The method is also applicable to RF-dressed traps, as demonstrated using an additional weak RF field to evaporatively cool gases in off-resonant and resonant traps [117, 125].

The same principle is used in RF spectroscopy by varying the frequency of a weak 'probe' field and observing atom loss at resonant frequencies. This method provides a means to measure the spacing between energy levels, and has been employed to measure effects beyond the RWA of the dressing RF [100] and in our own work to characterise MRF-dressed potentials [16].

For our proposed experiments, it becomes vital to understand these transitions, as the addition of multiple frequencies drastically increases the number of resonances. This in turn makes the potentials more susceptible to RF noise, which motivates the thorough investigation of RF transitions in this chapter.

The only published observation of a higher-order transition of atoms trapped in RF-dressed potentials is of the resonance at the frequency of the dressing field plus half the Rabi frequency reported in [118], and no experimental work has considered these processes further.

We test the predictions from Chapter 5 under a variety of experimental configurations. We start by presenting the experimental details of RF spectroscopy in general (Section 6.1) before describing the work for circularly- and linearly-polarised SRF traps (Section 6.3.1) as well as a linearly-polarised MRF trap (Section 6.3.2).

6.1 EXPERIMENTAL METHOD

RF Spectroscopy is widely used to characterise magnetic potentials: a weak probe field at frequency $\omega_p/2\pi$ is applied to the atoms for a duration t_p. If the probe frequency (or a multiple thereof) is resonant with the energy level splitting of atoms confined in a magnetic trap, the field drives transitions between the eigenstates of the atoms in the trapping potential. Atoms driven to untrapped states are lost, and the remaining atom number is measured by absorption imaging, resulting in the loss spectrum as the probe frequency is varied. An atom is lost with some probability depending on detuning, probe amplitude and duration. On resonance, the probability is highest, resulting in a peak in the loss spectrum, while far off resonance, the probe field does not affect the atom.

Inhomogeneous broadening of the resonance occurs for an atomic ensemble at finite temperature and in a magnetic trap, because the level splitting varies as a function of position. The lineshape depends on the trap parameters and cloud temperatures, with colder clouds resulting in narrower lineshapes [25, 117]. Probe strength and duration have to be chosen carefully when this technique is used to accurately measure transition frequencies. A strong probe field may shift the resonance; for a short duration, the instantaneous distribution of atoms is sampled, while for a long duration the atomic ensemble rethermalises. Additionally, long durations require long hold-times, leading to heating of the atoms and thus broadening the resonance.

In this section, we present the technical parameters for measuring the spectra presented in Section 6.3 and explain the characteristics of the probe field we use.

6.1.1 *Technical Implementation*

We perform spectroscopy on Bose-condensed clouds to achieve narrow lineshapes and distinguish neighbouring resonances when the spectrum is closely packed (as for the MRF case in Section 6.3.2). Our aim is to verify the existence of transitions rather than to accurately determine their frequency. To achieve this, we apply the maximum probe amplitude available in our apparatus (for details see below) to achieve a good signal-to-noise ratio (SNR). A probe duration of 1.2 s was determined to be optimal: the SNR is better than for shorter durations, whilst the fraction of condensed atoms remains large at approximately 0.45 to avoid broadening the resonances.

The experimental sequence is as follows: we apply the probe field after loading approximately 10^5 atoms and wait 100 ms after the probe field has been turned off for ejected atoms to leave the trap before taking an image after 25 ms TOF. Each frequency is typically probed on four separate runs, which is sufficient to disregard outliers. The spacing between neighbouring data points is 4 kHz and 2 kHz for the SRF and MRF cases respectively. 4 kHz is narrow enough such that no first- or second-order resonances are missed, but a narrower spacing is required to distinguish resonances in the MRF case where neighbouring resonances can be as little as 5 kHz apart.

6.1.2 *Amplitude of the Probe Field*

The probe field is generated using the coil and amplifier also used for evaporative cooling (see Section 4.1): the output of a DDS channel is amplified (*Mini-Circuits ZHL-1-2W-S*) before entering the probe coil. The amplifier is specified for frequencies from 5 MHz to 500 MHz[1]. Nevertheless, its frequency response is flat down to 2 MHz, below which the amplitude drops rapidly (Figure 6.1). Even so, we find that resonances at tens of kHz can still be observed.

The frequency response of the full system reveals a resonance of the probe coil at 4.7 MHz. We use the measured characteristics shown in Figure 6.1 (b) to rescale the

1 Thus covering the wide range of 120 MHz to 3 MHz necessary for evaporative cooling, but not ideal for RF spectrosocpy in the range 0 MHz to 7.4 MHz as presented here.

probe amplitude for different probe frequencies: we calibrate the DDS amplitude in the vicinity of the coil resonance (4.3 MHz to 5.1 MHz) to remove the influence of the peak; up to 4.3 MHz, the amplitude still increases with increasing frequency.

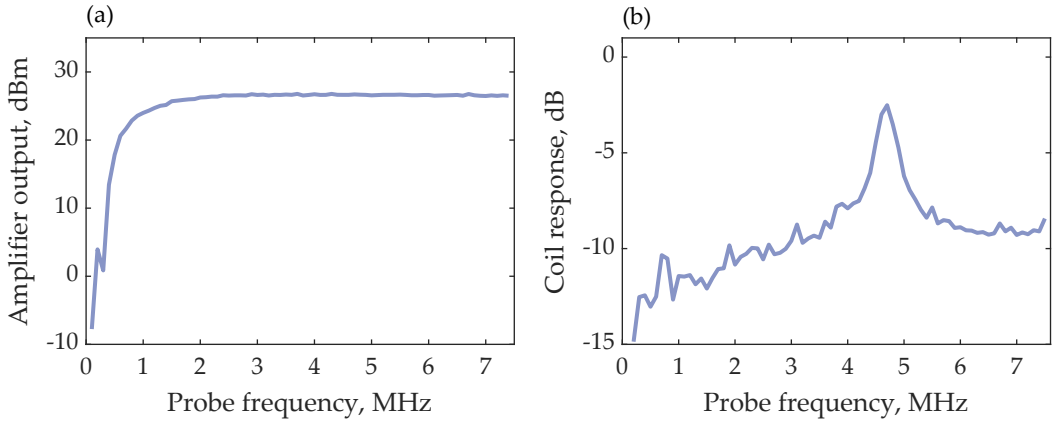

Figure 6.1: (a) Output power of the amplifier as a function of frequency, with the input provided by the DDS at maximum amplitude. While the amplifier is only specified for frequencies larger than 5 MHz, the response is nearly flat down to 2 MHz, when it starts dropping rapidly. (b) Response function of the probe coil, determined from measurements of transmitted and reflected power using a bi-directional coupler. A resonance at 4.7 MHz is evident, leading to an increase in the probe amplitude by a factor of five.

The antenna we use for the spectroscopy pulses is situated above and perpendicular to the coils generating the dressing fields, as shown in Figure 4.1. This results in a field with predominantly linear polarisation along the z direction, i. e. $\Omega_z \gg \Omega_\pm$ in Equation 5.2. We estimate the Rabi frequency of the applied field at 3.6 MHz as $\Omega_z = 2\pi \cdot 30\,\mathrm{kHz}$. This value is obtained by trapping atoms in a shell trap formed by a dressing field with frequency 3.6 MHz and applying the probe field at maximum amplitude, but turning it on adiabatically. The vertical field slightly modifies the potential, pushing the atoms to the side, with the direction determined by the phase between the dressing and probe fields [126, 127]. We determine the maximum horizontal displacement and thus the corresponding probe amplitude by taking in-situ absorption images of the trapped atoms for a relative phase between 0 and 2π.

However, since the coil consists of just two turns of wire added above the coil array and not precisely aligned, there will be other polarisation components as well. We observe all predicted first- and second-order transitions, including those which require σ_+ and σ_- terms. Transitions at low frequencies are mainly driven by the

vertical polarisation and can thus be observed despite the reduced field strength at low frequencies. We will use the data below to estimate the values for Ω_+ and Ω_-.

6.2 DATA ANALYSIS

Before presenting the measured spectra, we give details of the analysis routine used to identify resonances in the measurements, which was carried out in the same fashion for all spectra. Figure 6.2 shows a sample spectrum, illustrating several aspects explained below.

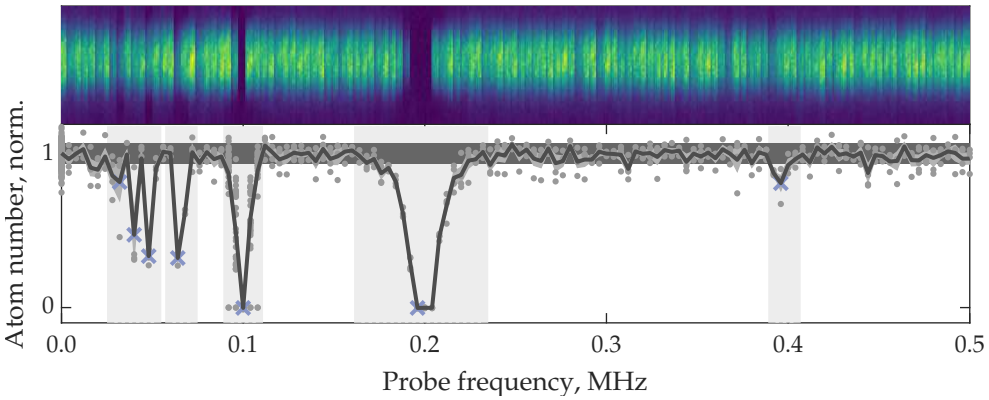

Figure 6.2: Slices of absorption images (top) and normalised atom number (bottom) versus probe frequency for atoms trapped in a linearly-polarised dressing field of a single frequency. The grey points indicate measured atom numbers (normalised), and the black line shows the average at each probe frequency. The light grey area indicates the standard error of the mean. The dark grey strip indicates the range of atom numbers within one standard deviation of the background distribution. Resonances identified from the data using the Kolmogorov-Smirnov test are marked with '×'. Probe frequencies which were excluded during the normalisation process are indicated by the light grey boxes.

The atom number prepared in each experimental cycle fluctuates randomly by about 10 %, and a dip in measured atom number due to a resonance must be reliably distinguished from this random noise. We determine this background statistical distribution by measuring the atom number (without a probe applied) at random times interleaved with each data series. Resonant frequencies are identified as those for which the mean atom number corresponds to a minimum, and the distribution of measured atom numbers is different from the background distribution, using the Kolmogorov-Smirnov (KS) test with a significance level of 0.01. This test compares a given dataset (in our case of typically four normalised atom numbers for a given

probe frequency) to a normal distribution. Any set with a p-value below the significance level is rejected and returned as a resonance candidate. The mean and standard deviation of the reference normal distribution are obtained from the background distribution.

Acquiring detailed spectra with many repeats and a cycle time of approximately one minute requires continuous operation for days at a time. The atom number prepared in our experiment typically drifts by 30 % over many hours due to variations in vacuum pressure, laser intensities, and magnetic fields, some of which are correlated to changes in room temperature. Some of these changes can be mitigated if the absolute atom number is of importance, but was not done for this data to allow faster data-taking. To reduce systematic effects, measurements and repeats at different frequencies were taken in a random, interspersed order. Furthermore, to remove long-term drifts, we normalise each atom number measurement with respect to the mean atom number in an interval spanning 30 minutes either side of that point[2], and excluding points with an applied probe RF on or close to resonance as determined by the KS test. This is carried out in a circular fashion: excluding regions which are evidently resonances, identifying resonances in the normalised spectrum as described below, then excluding these resonances in turn, and iterating this procedure until convergence.

A single resonance feature typically spans many neighbouring probe frequency measurements and we identify the resonant frequency of the transition as that which minimises atom number. Of the remaining resonance candidates, we reject those that are not minima[3] and verify those with small contrast, discarding them if they do not appear in an additional scan with smaller frequency spacing.

2 Since the drifts vary slowly with time compared to the duration of one sequence, with the fastest drifts on the order of the cycle of the air conditioning unit, about half an hour – one sequence takes about one minute – they can easily be averaged out.

3 In some cases, all repeats taken happen to coincide very closely, leading to a rejection by the KS test due to a low standard deviation alone. As we only take four measurements for each probe frequency, these occurrences are expected statistically.

6.3 MEASURED SPECTRA

We measure spectra of atoms trapped in an SRF trap with linearly- and circularly-polarised dressing fields to verify the existence of resonances predicted in Chapter 5 and find any additional resonances. The simpler case of a single dressing field facilitates comparison with the theory. We then present an MRF potential formed by three linearly-polarised dressing fields which is similar to the trap we used for matter-wave interference [25]. These results shed light on the requirements on noise levels and enable extrapolation to smaller frequency spacing and lower Rabi frequencies. We focus on low frequency transitions (surrounding the dressing field and below) since this is where most technical noise appears[4]. We calculate the transition frequencies and amplitudes for our experimental parameters up to fourth order for the SRF case and up to third order for the MRF case, and compare these to the experimental spectra.

6.3.1 *Single Radiofrequency*

For the simple case of a single dressing frequency, the trap is formed by a field at 3.6 MHz with an amplitude of 197 kHz for a linearly-polarised dressing field and an amplitude of 199 kHz for a circularly-polarised dressing field. The static quadrupole gradient is $155\,\mathrm{G\,cm^{-1}}$. We probe a wide frequency range for a linearly-polarised dressing field to verify whether all transitions are explained by our model and repeat ranges around observed resonances with circular dressing to observe differences between the two. The focus is on the lower frequency ranges, corresponding to higher-order probe effects and regions of typically higher technical noise. Effects of higher order in the dressing fields have been examined in great detail elsewhere [100].

6.3.1.1 *Linearly-Polarised Field*

Figure 6.3 shows the loss spectrum versus probe frequency for a linearly-polarised SRF-dressing field. The theoretical spectrum is displayed above the data.

4 Noise at tens or hundreds of kHz is often caused by switch-mode power supplies and ground loops, whereas noise surrounding the dressing frequencies appears as sidebands from the frequency generation.

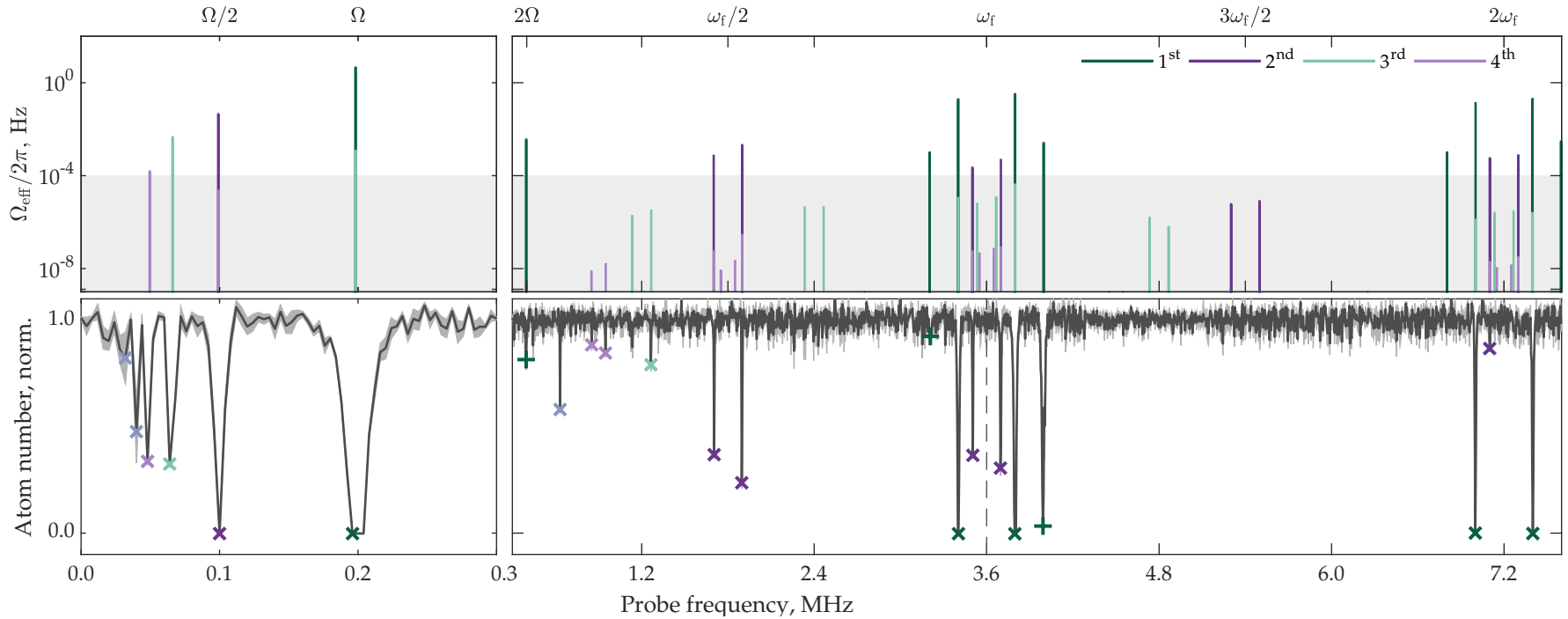

Figure 6.3: The loss spectrum for atoms in a linearly-polarised SRF dressing field. The predicted resonances (top) correspond to probe frequencies where loss is observed (bottom). Top: The magnitude of the matrix element is indicated by the length of the bar, with different colours indicating the order of the transition. Transitions due to the non-linearity of the Zeeman effect are included for first order. Probe values are chosen as $\Omega_z = 2\pi \cdot 30\,\mathrm{kHz}, \Omega_\pm = 2\pi \cdot 1\,\mathrm{kHz}$. The shading gives a rough indication of the threshold amplitude below which resonances cannot be detected, however there are exceptions, e. g. the resonances near 1.2 MHz. The angular frequency of selected points is indicated on the upper x axis. Bottom: These measurements of normalised atom number versus probe frequency are compiled from almost 8000 measurements taken over the duration of 12 days (and nights). The black line shows the mean atom number for typically four measurements at each probe frequency and the shaded area indicates the standard error of the mean. Resonances identified from the data are marked with crosses, where the colour indicates the order. Blue markers indicate that the resonance is higher order than fourth. An '×' indicates that the resonance was predicted in Section 5.3.2 and a '+' that it arises because of the non-linear Zeeman effect (see Section 5.4). The frequency of the dressing field is indicated by a vertical dashed line.

To calculate theoretical values for Ω_{eff}, the value for Ω_z at 3.6 MHz was taken to be $2\pi \cdot 30\,\text{kHz}$ as estimated in Section 6.1.2 and the values for $\Omega_+ = \Omega_- = 2\pi \cdot 1\,\text{kHz}$ were chosen such that the theoretical spectrum replicates the experimental one. These values are then rescaled with the variation of the probe amplitude (Section 6.1.2). As expected from the geometry of the coil array, $\Omega_\pm \ll \Omega_z$. All first-order coupling strengths are of a similar order of magnitude due to the following coincidence of our apparatus: transitions at low frequencies mainly couple via Ω_z, and transitions at higher frequencies mainly couple via Ω_-; $\Omega_z \gg \Omega_-$, but the amplitude of the probe field is smaller for lower probe frequencies. The strongest amplitude of the probe field is thus a factor of at least 6 smaller than the amplitude of the dressing field.

Since the experimental values for polarisation and amplitude of the probe field are only approximate, a more quantitative comparison cannot be made. The grey shaded area approximately indicates which transitions are visible.

Figure 6.3 shows resonances at frequencies of 0.196, 3.404, 3.796, 7.0 and 7.4 MHz, which we identify with all first-order resonances predicted by Equation 5.15 in the range 0 to 7.5 MHz, that is for $\kappa = 0, 1, 2$. Theoretically predicted transition strengths are on the order of $\Omega_{\text{eff}} = 2\pi \cdot 1\,\text{Hz}$ and all atoms are lost rapidly.

Second-order resonances can be identified with those predicted for $\kappa = 0, 1, 2$ at frequencies 0.1, 1.704, 1.896, 3.504 and 3.696 MHz as well as at 7.1 MHz for $\kappa = 4$. The dominant contribution to the transition strength for $\kappa = 3$ is proportional to $\Omega_z\Omega_+$, which makes it weaker than transitions for $\kappa = 4$ which are proportional to ${\Omega_z}^2$. Second-order Rabi frequencies are on the order of $\Omega_{\text{eff}} = 2\pi \cdot 10^{-3}\,\text{Hz}$, and slightly more than half the atoms are lost within $t_p = 1.2\,\text{sec}$.

In addition, we observe resonances at 64, 48, 40 and 32 kHz which correspond to i^{th} order transitions at Ω/i for $3 \leq i \leq 6$. Although these are predicted to be weaker than some transitions we do not observe, third and fourth-order resonances also appear at frequencies 1.264, 0.852 and 0.948 MHz, i. e. for $\omega_p = (\omega_{\text{rf}} + \Omega)/3, (\omega_{\text{rf}} \pm \Omega)/4$. We observe one 6^{th}-order resonance at a frequency of $\omega_p = (\omega_{\text{rf}} + \Omega)/6 = 632\,\text{kHz}$. Figure 6.4 shows a scan of the resonance at $(\omega_{\text{rf}} + \Omega)/6$, with a FWHM of 1 kHz. We have verified that it is indeed 6^{th} order by varying the Rabi frequency and observing the expected shift in the transition frequency. This suggests that further, higher-order

resonances were missed due to the wide frequency spacing of the probe field. It also explains why the maximum loss does not fully correspond to the predicted strengths – especially for higher-order resonances, the maximum loss observed depends on how close to the resonance the closest probe frequency happened to be.

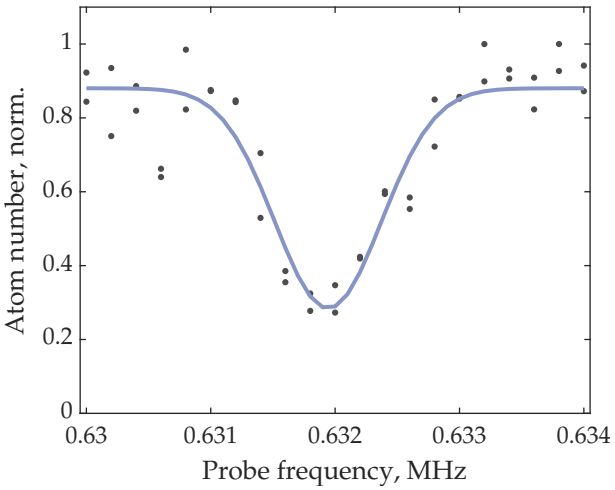

Figure 6.4: The loss spectrum of the 6^{th}-order resonance at $\omega_p = (\omega_{rf} + \Omega)/6 = 632\,\text{kHz}$. The spacing between probe frequencies is 0.2 kHz. The blue line shows a Gaussian fit to the data with a centre of 631.9 kHz and a FWHM of 1 kHz.

Resonances at frequencies of 0.396, 3.208 and 3.992 MHz are visible, but do not correspond to the transitions predicted by Equation 5.15. They can be matched to transitions at $\kappa\omega_{rf} \pm 2\Omega$ for $\kappa = 0, 1$, frequencies which correspond to the energy difference between states with $m = 1$ and $m' = -1$. In Section 5.4 we argued that the non-linearity of the Zeeman effect causes the appearance of these resonances. Here we see that this is indeed strong enough to observe the resonances, and it is therefore necessary to take this into account. The transition strengths for first-order transitions are included in Figure 6.3.

We have verified this result by varying both the dressing RF and Rabi frequency, and the resonances move as expected as a function of these parameters. Additionally, we trap atoms in RF-dressed potentials with dressing frequencies of 3.0 MHz, 3.6 MHz and 4.2 MHz and a Rabi frequency of 190 kHz, and perform RF spectroscopy of the atoms with a probe frequency at twice the Rabi frequency and with $t_p = 2\,\text{sec}$. Figure 6.5 shows the result. The loss occurring on resonance increases as the dressing RF increases, supporting the hypothesis that this transition is due to the non-linear Zeeman effect.

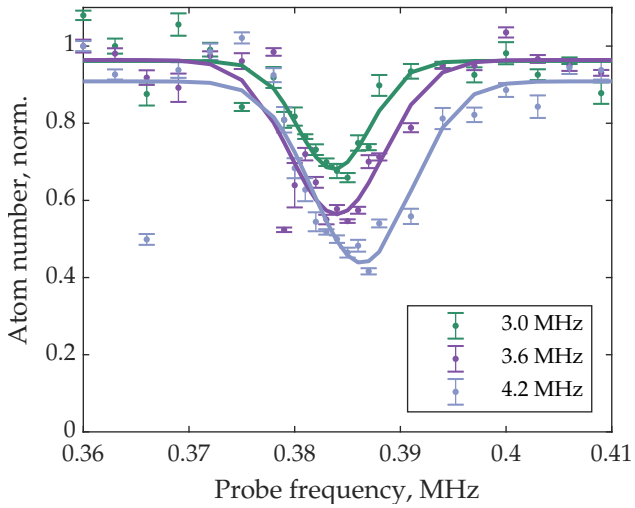

Figure 6.5: RF spectroscopy at twice the Rabi frequency for dressing frequencies of 3.0 MHz (green), 3.6 MHz (purple), and 4.2 MHz (blue) and a Rabi frequency of approximately 190 kHz. Each point is averaged from six data points, and the standard error of each mean indicated by the error bars. The lines indicate a Gaussian fit.

While the resonances at 400 kHz and 3.2 MHz are barely visible above the background noise, the resonance at 4 MHz is notably stronger, which we partially attribute to the increased amplitude of the probe at 4 MHz compared to 3.2 MHz (see Figure 6.1 (b)).

We observe a total of 22 resonances, all of which can be explained by the theory presented in Chapter 5. An overview of the number of predicted and observed first to fourth order resonances is given in Table 6.1. Only the first-order resonances and the resonance at $\omega_{\mathrm{rf}} + \Omega/2$ have been observed in previous work [100, 118].

ORDER	0 MHz TO 4 MHz				4 MHz TO 7.4 MHz			
	PREDICTED		OBSERVED		PREDICTED		OBSERVED	
	π	σ	π	σ	π	σ	π	σ
1st	3	3	3	3	2	0	2	0
2nd	5	5	5	5	4	0	1	0
3rd	7	7 (3)	2	1	6	2	0	2
4th	9	9 (7)	3	0	8	4 (0)	0	0
$\frac{n\omega_f \pm 2\Omega}{2\pi}$	3	3	3	3	2	2	0	0

Table 6.1: Number of observed and predicted resonances for the SRF cases. π and σ indicate values for linearly- and circularly-polarised dressing fields respectively. For the circular case, numbers in parentheses indicate number of probed resonances (since we did not take the full spectrum).

6.3.1.2 *Circularly-Polarised Field*

Figure 6.6 shows spectra of atoms trapped by a circularly-polarised dressing field (with an amplitude of 199 kHz) for subregions where resonances appeared with a linearly-polarised field.

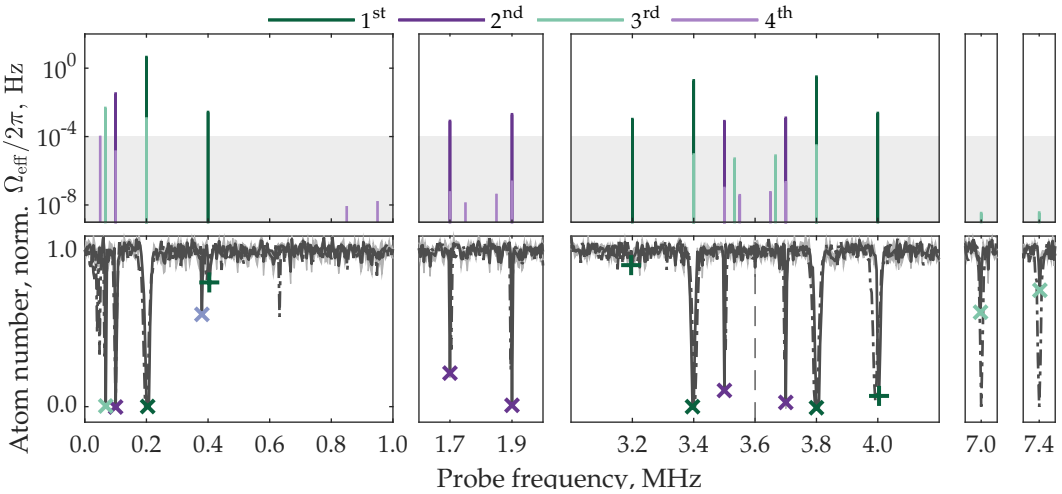

Figure 6.6: Loss spectrum for a circularly-polarised SRF dressing field. These measurements of normalised atom number versus probe frequency are compiled from more than 3000 measurements. The plot style is consistent with Figure 6.3 and the scale of the x axis is the same for all subplots. As a reference, the mean atom number for the linear case is shown (dash-dotted line). The small offset between resonances is due to slightly different Rabi frequencies for the two cases.

It is immediately obvious that the transitions with $\omega_p = 2\omega_{rf} \pm \Omega$ are much weaker than for the linear case, as is to be expected: these are forbidden in a circularly-polarised dressing field and first order, since the eigenstates only contain bare states of one manifold; however they do appear as third-order resonances for the case of arbitrary probe polarisation. While care was taken to achieve the best possible circular polarisation, any imperfection in the alignment of the coils or the phase between the two fields will strengthen these transitions, accounting for the fact that these appear stronger than any other third-order resonances[5].

The transitions at $(\kappa\omega_f \pm 2\Omega)/2\pi$ can also be observed here, but other weaker resonances have disappeared completely. A full comparison can be found in Table 6.1. As in the linear case, we happen to observe one resonance of even higher order: at a probe frequency of 0.38 MHz, we observe atom loss. We have observed this peak

5 As a result, these transitions could be used to further improve the phase between the two dressing fields, if it becomes necessary to improve the accuracy achievable by the method we currently employ [25, 94].

move with the Rabi frequency as would be expected for the 10^{th}-order resonance at $\omega_p = (\omega_{rf} + \Omega)/10$. The width of this resonance is well below 1 kHz.

With a probe frequency close to the dressing RF, variation in atom number increases, which appears in the spectrum resembling a weak resonance. We attribute this to a sudden perturbation in the dressing potential when the probe field is turned on at these frequencies, increasing the amplitude of the dressing field suddenly. The resulting kick imparted to the atoms causes heating and loss. Given that the amplitude of the dressing field is only about seven times stronger than that of the probe field, this is unsurprising.

6.3.2 *Multiple Radiofrequencies*

Applying additional dressing frequencies introduces more transitions, as dressing photons of different frequencies can be involved. In Chapter 5 we used a theoretical approach to predict the frequencies at which these transitions occur, and we now test the validity of these calculations. With multiple dressing frequencies present, we expect transitions to repeat at the common fundamental frequency as in Equation 5.16. The transition strength not only depends on the probe polarisation and amplitude, but also on the integer κ in Equation 5.15.

We apply three linearly-polarised dressing fields with frequencies 3.6, 3.8 and 4.0 MHz, i. e. $\omega_i = n_i \omega_f$ with $\{n_1, n_2, n_3\} = \{18, 19, 20\}$ and $\omega_f/2\pi = 200$ kHz. Atoms remain trapped in the well formed by the 3.6 MHz radiation. The amplitudes of the other two dressing fields are chosen such that they are sufficiently large in order to observe transitions driven by them. Additionally, we choose the Rabi frequency of the primary RF such that no two transitions overlap[6] – for example, with a frequency separation of $\omega_f/2\pi = 200$ kHz and a Rabi frequency of $\Omega/2\pi = 100$ kHz, the transition frequency of $\omega_p = \Omega$ would be equal to that of $\omega_p = \omega_f - \Omega$. Parameters which fulfil these conditions are amplitudes of 80 kHz, 69 kHz and 99 kHz. Note that the observed resonances are shifted by the presence of the other two RFs as well as

6 Of course, this is not a general requirement but only necessary for spectroscopy, so different resonances can be resolved.

gravity, e. g. resulting in an observed transition at $\Omega/2\pi = 72.5\,\mathrm{kHz}$ rather than at 80 kHz as discussed in [16]. A quadrupole gradient of $155\,\mathrm{G\,cm^{-1}}$ was used, which provides a lifetime in the trap sufficient for a probe pulse duration of 1.2 s. In contrast our matter-wave interference experiments use a closer well spacing that is provided by a higher quadrupole gradient of $219\,\mathrm{G\,cm^{-1}}$ [25].

Each frequency is probed four times, except in the range 0 kHz to 400 kHz, where we probe each frequency nine times to improve the SNR, since the resonances are densely populated. Due to the large number of observed transitions, we did not repeat measurements of low-contrast resonances.

Figure 6.7 shows the experimental spectrum with theoretical predictions displayed above. We restrict the range to a maximum of 4.8 MHz, since the behaviour at higher probe frequencies is expected to be periodic but extremely weak, as was shown for the linearly-polarised SRF case. It is immediately obvious that there is a plethora of transitions surrounding the Rabi frequency and dressing frequencies.

In the theoretical spectrum, a periodicity of transition amplitudes of order i with ω_1/i is evident. As explained in Section 5.3.3, this is due to the fact that approximately $n_1/2 \approx 10$ creation or annihilation operators are required for transitions with $\kappa = n_1/2$. In contrast, the second-order transitions at frequency $(n_1\omega_\mathrm{f} \pm \Omega)/2$, require one creation operator only, since $\kappa = n_1$. This results in second-order transitions being significantly stronger than first-order ones surrounding the probe frequencies near $\omega_1/2$. The same behaviour can be observed for third-order transitions.

These predictions agree well with the observations: most of the visible resonances are at low frequencies, as well as surrounding the dressing frequencies. Additionally, some transitions at $(\omega_\mathrm{rf} \pm \Omega)/i$ are visible for $i = 2, 3, 4$ and for $\omega_\mathrm{rf} = \omega_1, \omega_2, \omega_3$. Again, transitions at $\kappa\omega_\mathrm{f} \pm 2\Omega$ appear, as a result of the non-linearity of the Zeeman effect.

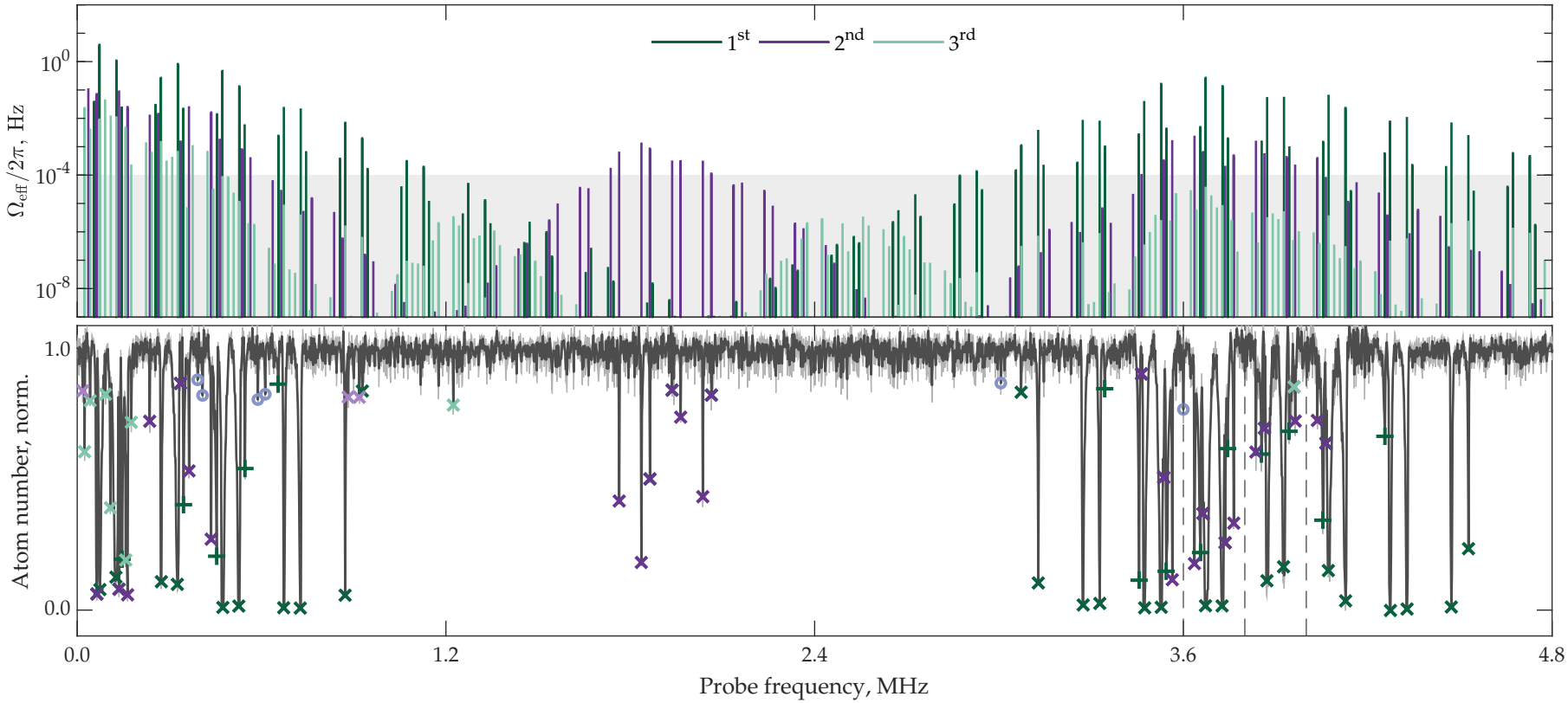

Figure 6.7: Normalised atom number versus probe frequency for the MRF case, compiled from more than 11000 measurements taken over the duration of 16 days (and nights). The plot style is consistent with Figure 6.3. Magnified plots of the frequency regions 0 MHz to 0.4 MHz and 3.5 MHz to 4.1 MHz are shown in Figures 6.8 and 6.9.

In total, we observe 83 resonances, and identify them with theoretical peaks if the observed and predicted frequency are no more than 2 kHz apart. This corresponds to the spacing of neighbouring points and is smaller than the typical linewidth. Of the total resonances, there are 26 first-order, 26 second-order, 7 third-order, and three fourth-order resonances. A total of 14 resonances for transitions $m = 1$ to $m' = -1$ can be observed. One more resonance can be identified with a third-order transition if we extend the distance between theoretical and measured value to 2.5 kHz.

The remaining six unidentified resonances are weak dips close to $n\omega_f/2\pi$, identified in Figure 6.7 with blue circles. They appear around 0.4 MHz, 0.6 MHz, 3.0 MHz and 3.6 MHz, and some are visible in Figure 6.8 and Figure 6.9. While these are stronger than in the SRF case, we again attribute them to the fact that a probe field at the fundamental frequency will act as an additional dressing field, causing a sudden change in the potential and leading to loss.

We show an overview of the observed resonances in Table 6.2 and elaborate on the observations below.

ORDER	PREDICTED	0 – 0.2	0.2 – 0.4	0.4 – 0.6	0.6 – 0.8
1st	2	2	2	2	2
2nd	4	3	3	1	0
3rd	6	6	0	0	0
$\frac{n\omega_f \pm 2\Omega}{2\pi}$	2	1	1	2	1
unexplained	-	0	1	2	1
ORDER	PREDICTED	3 – 3.4	3.4 – 3.8	3.8 – 4.2	4.2 – 4.6
1st	4	4	4	4	4
2nd	8	0	7	5	0
3rd	12	0	0	1	0
$\frac{n\omega_f \pm 2\Omega}{2\pi}$	4	1	4	3	1
unexplained	-	1	1	0	0

Table 6.2: Number of observed and predicted resonances in selected regions for the MRF case. The number of predicted resonances is the same for each of the intervals shown and indicated in the second column. Intervals shown in MHz.

First-order resonances can be observed until 873 kHz $= (4\omega_f + \Omega)/2\pi$, while the amplitudes of higher-order transitions decay faster. This transition at 873 kHz cor-

responds to a minimum of four creation and annihilation operators, two each of 3.6 MHz and 4.0 MHz.

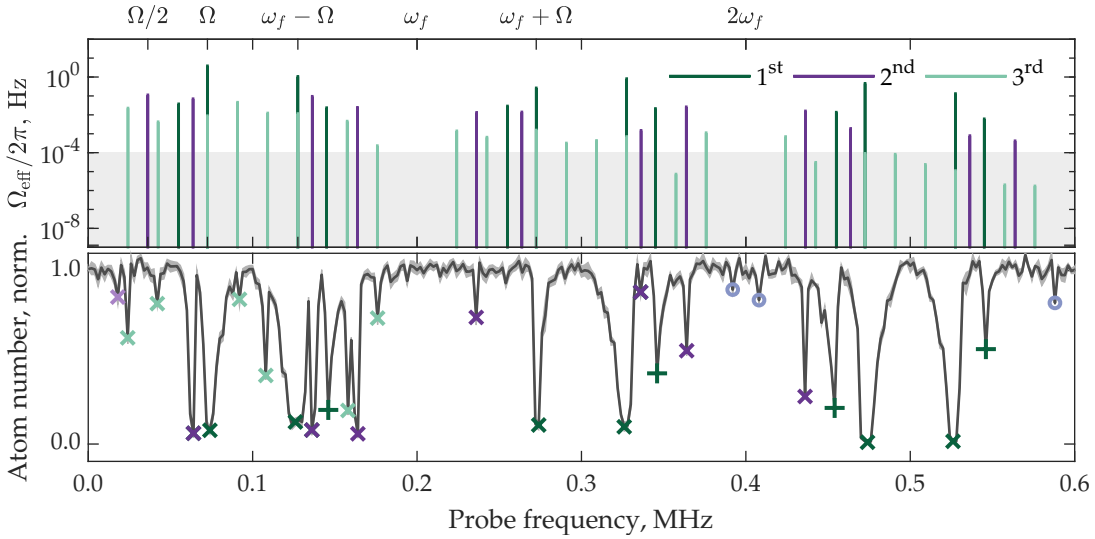

Figure 6.8: Loss spectrum for the MRF case on an expanded scale focussing on low frequencies. The plot style is consistent with Figure 6.3.

The low-frequency region is shown on an expanded scale in Figure 6.8. The transitions are predicted to be periodic with the fundamental frequency, with the lowest-frequency transitions being the strongest, as they are lowest order in the dressing field. The only visible fourth-order transition is at $\Omega/4$, and third-order resonances are only visible below $\omega_f/2\pi$. As the amount of creation or annihilation operators of the dressing field that are required increases, higher-order transitions vanish. In the region 200 kHz to 400 kHz, most second-order transitions can still be observed. The periodicity of transitions with the fundamental frequency is apparent in the theory lines and can be seen in the data with the repetition of first-order transitions.

In the region between low frequencies and the dressing frequencies, while resonances are predicted to exist from the theory, most are too weak to be observed with the probe powers and durations that we use. This is because the creation or annihilation of a large number of dressing field photons is involved in those transitions, in combination with the relatively low field amplitudes. The exceptions are transitions which are lowest order in the dressing field: two fourth-order transition at $\frac{1}{4}(\omega_1 \pm \Omega)/2\pi$, one third-order transition at $\frac{1}{3}(\omega_1 + \Omega)/2\pi$ and all second-order transitions at $\frac{1}{2}(\omega_i \pm \Omega)/2\pi$, as well as one transition at $\frac{1}{2}(4.2\,\text{MHz} - \Omega)/2\pi$. The

transitions $\frac{1}{2}(\omega_1 \pm \Omega)/2\pi$ are the strongest, since the involved dressing field is the primary RF which traps the atoms.

Figure 6.9 shows the frequency region surrounding the three dressing frequencies. The transitions surrounding the primary dressing field at 3.6 MHz are asymmetric, with more transitions visible towards the higher frequencies due to the presence of the other dressing fields. First-order resonances are visible up to 600 kHz either side of the dressing frequencies. Raising or lowering the value of k five times is required for the extrema at $3\,\text{MHz} + \Omega/2\pi$ and $4.6\,\text{MHz} - \Omega/2\pi$. Again, we observe the periodicity of resonances with the fundamental frequency, with gaps surrounding any frequency $n\omega_f/2\pi$ and higher-order transitions clustering around those of first order.

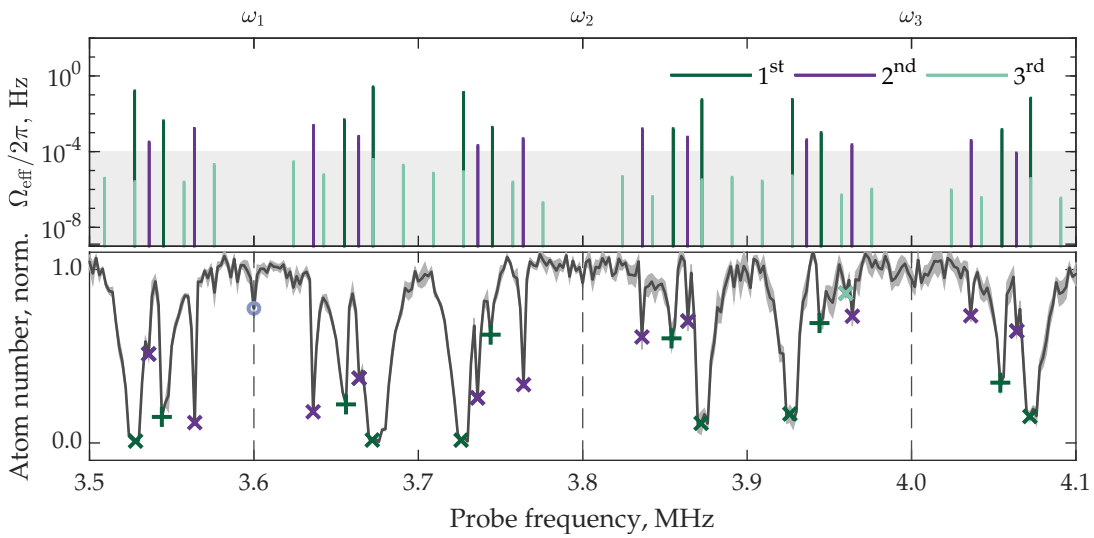

Figure 6.9: Loss spectrum for the MRF case on an expanded scale focussing on frequencies surrounding the dressing RFs. The plot style is consistent with Figure 6.3.

6.4 DISCUSSION

We performed RF spectroscopy of atoms trapped in single- and multi-frequency fields, for the first time observing transitions higher than second order in the probe field. We find very good agreement between the observed and the theoretically predicted transition frequencies. First-order transitions between states with $m = 1, m' = -1$ were observed, which were not apparent in previous work; these arise from the non-

linearity of the Zeeman effect. This effect introduces an asymmetry into the Hamiltonian operator that results in a coupling of states with $m = 1, m' = -1$, thus causing a breakdown of the selection rules.

The observed atom loss agrees qualitatively with the predicted transition strengths, though we also observe loss for surprisingly low effective Rabi frequencies. Several details of the experiment prevent a more detailed quantitative comparison: firstly, the polarisation and amplitude of the probe field is undetermined. Secondly, the 4 kHz spacing of data points means that we do not accurately determine the maximum loss rate, especially for the intrinsically narrower higher-order transitions. A clear example of this lack of resolution occurs for the observed 6^{th}-order resonance with a FWHM of 1 kHz. It would be both impractical and unnecessary to apply this resolution over the whole range of frequencies inspected here. It is likely that some high-order resonances were missed by our experimental procedure, but more than a sufficient number of transitions were observed to give an extremely high degree of confidence in the theoretical model presented in Chapter 5, and all observed transitions in the linearly-polarised SRF case are explained. The large range of probe frequencies we have scanned ensures that we have not missed any other resonances strong enough to be a limitation.

We observe higher-order transitions even for moderate probe amplitudes. These include previously unseen transitions which result from a combination of different probe polarisations; this emphasises the importance of taking into account all possible polarisations of the probe field when determining the effect of stray fields.

In the MRF case, the number of resonances increases, clustering at low frequencies as well as surrounding the dressing frequencies. These measurements support the requirements on noise mentioned above: both low-frequency noise and sidebands on the dressing field are highly destructive, leading to rapid atom loss. However, the strength of resonances drops rapidly as we move away from these regions with higher-order resonances becoming weak very rapidly.

With the combination of low amplification for low frequencies and high amplification for high frequencies, but large fraction of σ_z polarised probe, we probe all resonances in the spectrum to a similar degree. In combination with the model pre-

sented in Chapter 5, these results permit an accurate determination of the resonance spectrum for atoms trapped in MRF-dressed potentials. In particular, our work provides a framework to understand and mitigate the loss of atoms through spurious noise when working with MRF-dressed potentials. This is of critical importance for experiments that use many closely-spaced frequencies, such as the proposal to form a periodic potential of individually controllable wells [24], and the double-well potential described in this work. In Section 7.2, we apply these results to amplitude ramps of an MRF-dressed potential.

7

SPLITTING A BOSE-EINSTEIN CONDENSATE

To achieve the aims set out in Chapter 2, ultracold atoms must be loaded into a 2D potential and coherently split. The experimental sequence described in Reference [25] was used to split a BEC and observe matter-wave interference. In this chapter, we will present an alternative method of splitting BECs trapped in RF-dressed potentials. It has advantages over the ramps of Reference [25], such as no associated centre-of-mass motion of the atoms and shorter ramp duration.

As explained in Section 3.4, 2D confinement requires lowering the Rabi frequency of the dressing field. This brings the resonances calculated in Chapter 5 into the vicinity of low-frequency noise currently present on the experimental apparatus and thus reduces the lifetime of trapped atoms. Improved hardware for frequency generation and impedance matching is currently being developed to achieve long lifetimes at low Rabi frequencies, and will be detailed in future theses [110, 128]. Due to these limitations all measurements presented in this chapter were obtained using 3D gases, but the methods are the same for 2D confinement.

In Section 7.1 we explain the amplitude ramps and show how these can be used to split a BEC, highlighting the differences to the previously used scheme. Comparing resonant transitions for both methods illustrates further advantages of the new ramps in Section 7.2. We then detail the limitations of the current apparatus in Section 7.3 and present the next steps towards coherent splitting and observing matter-wave interference.

7.1 AMPLITUDE RAMPS

We review the amplitude ramps that were previously used to split a BEC before explaining the improved ramps and demonstrating these experimentally. The RF field amplitudes for each frequency component are calibrated independently using RF spectroscopy of SRF-dressed, linearly-polarised, shell traps. These calibrations are then used to determine control amplitudes for ramps in MRF-dressed potentials. Saturation and mixing in the dressing-RF amplifiers reduces the amplitudes if multiple frequencies are present by less than one percent. In this chapter, we state the control amplitudes defined by the SRF case; the actual, reduced amplitudes can be determined by measuring the amplitude of the emitted RF fields using a pickup coil, which is also calibrated by RF spectroscopy.

7.1.1 *Review of the Ramps Used in Previous Work*

The thesis of Elliot Bentine [25] reported results on splitting and subsequent interference of a BEC trapped in an RF-dressed potential. This was achieved using near-adiabatic amplitude ramps of 200 ms duration, and suffered from significant atom loss. Atoms were first loaded into the upper well, formed by a field with frequency $\omega_u = 2\pi \cdot 3.6\,\mathrm{MHz}$ and amplitude Ω_u. The fields for the lower well and barrier, at frequencies of $\omega_l = 2\pi \cdot 4.0\,\mathrm{MHz}$ and $\omega_b = 2\pi \cdot 3.8\,\mathrm{MHz}$ and amplitudes Ω_l and Ω_b, were then turned on and atoms were first transferred into the centre of a 3-RF single well, before splitting the cloud into two. A graph of the ramps is shown in Section 7.2, where we present the associated resonant transitions. For fully adiabatic ramps, atoms were lost as Ω_b was increased, and we avoided this loss by turning the field on at $\Omega_b = 2\pi \cdot 80\,\mathrm{kHz}$ and only changing it adiabatically afterwards. We will refer to these ramps as the 'barrier jump' ramps, and to those without the jump as the 'adiabatic' ramps.

7.1.2 *Projection Ramps*

Here, we present alternative amplitude ramps and demonstrate that they split an ultracold gas in less than half the time, and without displacing the centre-of-mass of the cloud. We use the same dressing frequencies, and the final potential is the same as used previously. Rather than beginning the sequence with atoms loaded in an SRF shell at 3.6 MHz (the upper well), we instead begin with atoms loaded into an SRF shell at 3.8 MHz (the barrier).

Figure 7.1 (a) shows the subsequent ramps, with the potential shape for four selected times shown in Figure 7.1 (b). The amplitude of one coil is ramped down to load the atoms into a potential formed by linearly-polarised fields, while the amplitude of the other coil is increased from 200 kHz to 240 kHz. Contrary to the previous ramps, no adiabatic deformation of the potential can be used for splitting the cloud in this case, since adiabatically increasing the fields will result in atoms being trapped in the 'wrong' eigenstate. Any such deformation would result in atoms staying in the same eigenstate, and thus ending in the anti-trapped state of the double-well potential[1]. In the 'projection' ramps, we instead turn on the other RF fields suddenly, projecting the atoms into an eigenstate of the MRF-dressed potential (second panel in Figure 7.5 (b)). If the Rabi frequencies are chosen appropriately, the majority of the atoms stay trapped in a 3-RF single well (see Section 7.1.3). The value of Ω_b can then be reduced adiabatically, thus raising the barrier and splitting the cloud. The final wells have a separation of 4.8 µm for the parameters shown here, which is well within the range to observe matter-wave interference.

Note that for an amplitude of $\Omega_b = 2\pi \cdot 200\,\text{kHz}$, the potential exhibits a kink rather than smooth dependence on position (third panel in Figure 7.5 (b)). Atoms cannot follow the trapped eigenstate adiabatically, leading to rapid loss [99]. We find that a ramp duration on the order of 80 ms is long enough not to induce motion during the

1 This applies to any deformation of the form describe here, with three RF fields. Using a 2-RF field, where one component is linearly polarised in x, and the other linearly-polarised in the vertical direction, can also result in a double-well potential. In this case, the second frequency corresponds to the level splitting of the trapped atoms, and the double-well potential is similar to the 1D double-well created by a single frequency in Reference [82]. In this scheme, however, there would be no way to account for gravity, or to individually manipulate the two wells.

splitting procedure, whilst retaining a sufficient number of atoms to obtain two BECs after the split.

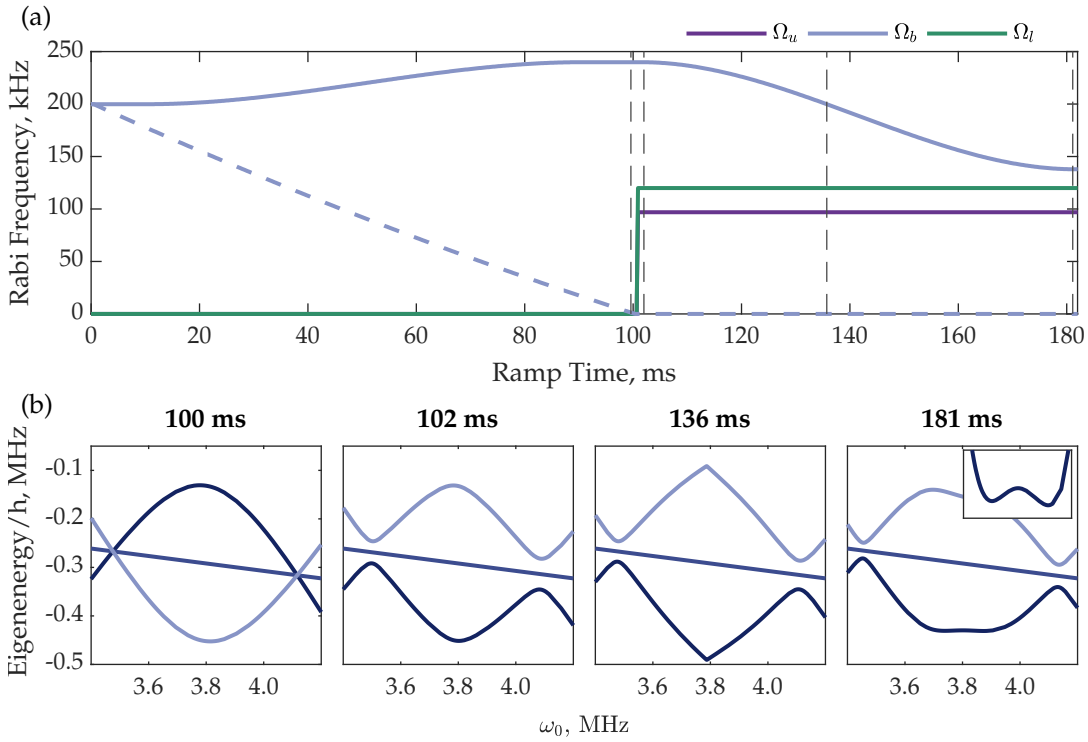

Figure 7.1: (a) Amplitude ramps for splitting a BEC. Atoms are loaded into a circularly-polarised potential created by a field with a frequency of 3.8 MHz (blue lines). After loading, the amplitude of one coil is reduced to zero (dashed line). Then, fields at frequencies of 3.6 MHz and 4.0 MHz (purple and green lines) are turned on near-instantaneously. Vertical dashed lines indicate times for which the corresponding potentials are plotted below. (b) Potential energies for $m = 1, 0, -1$ states as a function of ω_0. Atoms are initially trapped in the light blue eigenstate, and projected into the dark blue eigenstate when the additional fields are turned on. Note that the avoided crossings that appear at the edges result from higher-order resonances. The first-order crossings due to the additional frequencies act to form a three-RF single well, which is then transformed into a double-well potential. This is magnified in the inset of the last panel which shows the region 3.67 MHz to 3.93 MHz with an energy range of 5 kHz $\cdot h$.

These ramps can be divided into two parts, the first being the projection into the MRF potential, and the second the subsequent adiabatic ramps for splitting. The investigation of both of these is described in the sections below.

7.1.3 *Projecting into a Multiple-Radiofrequency-Dressed Potential*

Two problems may arise due to the projection: First, the spatial mode of the traps before and after projection is different, thus causing motion and heating of the atoms.

In our case, the vertical trap minima before and after projection are separated by 0.43 µm and we have observed no evidence of motion or heating due to this separation. Secondly, not all atoms are projected into the trapped eigenstate, causing atom loss.

To investigate the ratio of atoms trapped in the MRF potential after the projection, we load a linearly-polarised SRF shell trap. Afterwards, the two fields corresponding to the two wells are turned on instantaneously. This corresponds to the first 102 ms of the ramp in Figure 7.1 (a). Atoms that were projected into the trapped state are then held in this 3-RF single-well before being released and imaged after TOF expansion. Atoms that were projected into the untrapped state with $m = 0$ are lost from the trap, and fall under gravity. Lastly, atoms that were projected into the antitrapped state are accelerated upwards by the potential, and only start falling under gravity once the potential is turned off. For a hold time of 8 ms and a TOF duration of 16 ms, we can observe all three clouds in the field of view. We compare the atom number projected into the three eigenstates states to the atom number in the SRF trap for different values of the field amplitude Ω_b.

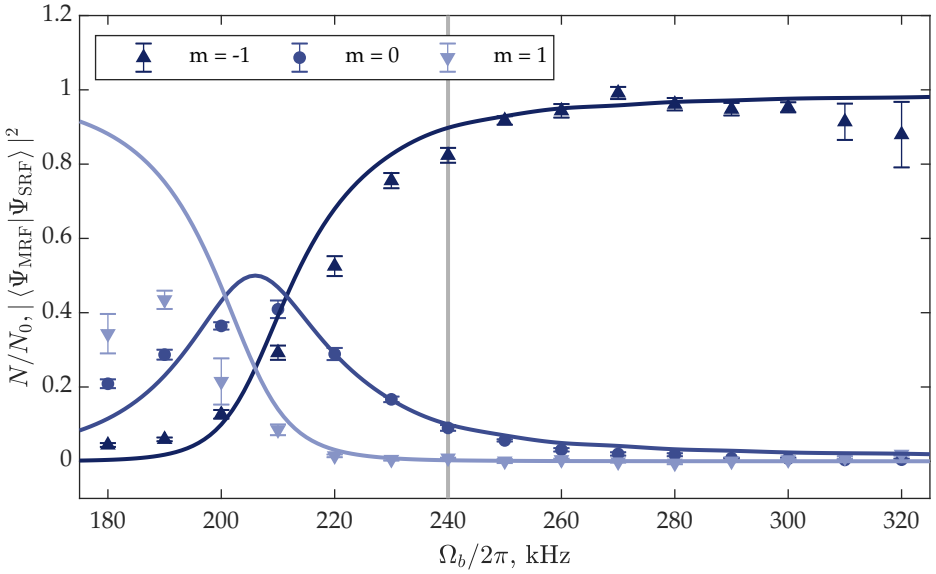

Figure 7.2: Fraction of atoms remaining trapped (▲), and atoms being projected into the $m = 0$ and $m = 1$ states (●,▼) and thus lost from the trap, as a function of barrier amplitude. The ratio of measured atom number N over atom number before projection, N_0, is displayed. The mean and standard deviation are obtained from five measurements. Additionally, the square of the overlap of the initial state Ψ_{SRF} in the SRF potential and the final state Ψ_{MRF} with $m = -1, 0, 1$ in the MRF potential (solid lines) are shown. A vertical line indicates the amplitude of the 3.8 MHz field chosen for the remaining measurements of this chapter.

Figure 7.2 shows the variation of relative atom numbers with the barrier amplitude. For comparison, the overlap of the wave functions before and after the projection, $|\langle\Psi_{\mathrm{SRF}}|\Psi_{\mathrm{MRF}}\rangle|^2$, is shown. The wave functions were calculated using the Floquet code presented in Reference [25]. Owing to the semi-classical approximation, these eigenstates do not include the state of the RF fields. The measured field amplitudes before and after the projection were used for the calculations, thus accounting for the saturation of the amplifier when turning on the additional fields. This amplitude reduction could easily be mitigated by increasing the control amplitude of the barrier field simultaneously. The values on the x axis in the graph correspond to the control amplitude and thus to the amplitude of the 3.8 MHz field forming the SRF-trap before projection.

For amplitudes of the 3.8 MHz field above 260 kHz, we observe a vertical oscillation of the trapped atoms. We attribute this to parametric driving as the trap frequency changes with RF amplitude and comes into resonance with spurious noise. This is not an intrinsic problem of the scheme described here and can be removed once the responsible noise source has been identified. For barrier values above 300 kHz, it prevents an accurate determination of atom numbers and results in larger error bars.

The antitrapped cloud is accelerated by the potential after projection takes place, and oscillates in the well formed by a higher-order resonance. This leads to a heated and elongated cloud when observed, preventing an accurate determination of atom number. Furthermore, atoms are lost due to non-adiabatic loss occurring as they transit the higher-order resonance. These effects explain the disagreement between the theoretically predicted and the experimentally observed fraction of antitrapped atoms.

We choose a value of $\Omega_b = 2\pi \cdot 240\,\mathrm{kHz}$ as a compromise between atom loss due to the projection for low amplitudes, and the parametric driving at high amplitudes. Once the cause of the parametric heating has been identified and removed, higher initial values for Ω_b are possible, such that a larger fraction of the initial atom number can be retained.

7.1.4 *Characterising the Projection Ramps Experimentally*

We split a BEC trapped in a potential formed by a single field of 3.8 MHz and a quadrupole gradient of 199 G cm^{-1} by applying the ramps shown in Figure 7.1. The atoms are then released from the trap by turning off the quadrupole gradient as described in Section 4.3. Atoms trapped in different wells experience different acceleration as the quadrupole field is reduced. Thus, the two clouds are separated after TOF. This method is helpful for diagnostics and improving the splitting procedure. For matter-wave interference, the clouds have to be overlapped and we release the atoms from the trap by turning off the dressing fields.

Figure 7.3 (a) shows absorption images of atoms released and imaged after TOF for different values of the final barrier amplitude. This value determines whether atoms stay in the central 3-RF single well or whether the cloud is split into two. A high value of Ω_b reduces the barrier height, while a low value increases it (see Figure 3.4). Thus, higher amplitudes of the field at 3.8 MHz lead to smaller well separation, and for the final value of 143 kHz we achieve a well separation of 4.8 µm.

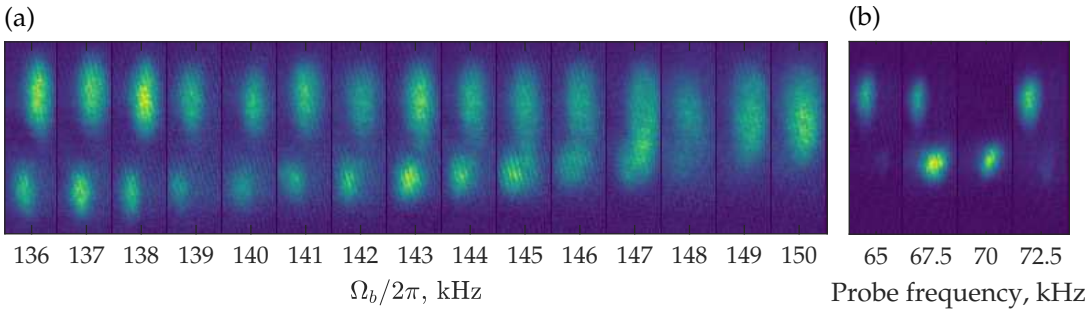

Figure 7.3: Absorption images of atoms after a TOF of (a) 15 ms and (b) 10 ms. The top cloud corresponds to atoms in the upper well, and the bottom cloud to atoms in the lower well. (a) Varying the final value of Ω_b determines whether the BEC is split. (b) Applying a probe RF at different frequencies removes atoms from one well or the other selectively.

To prove unambiguously whether the two clouds correspond to atoms trapped in the two wells, we apply a probe field as in Chapter 6, thus ejecting atoms from one well only for a given probe frequency. The dressing amplitudes lead to first-order transitions at 58 kHz for the upper, and 71 kHz for the lower well, with a second-order transition at 65 kHz for the lower well, and at 71 kHz for the upper well. Figure 7.3 (b)

shows images with the probe field in the range 65 kHz to 72.5 kHz, and all predicted resonances are present. Due to some uncertainty in the field amplitudes, and the coarse frequency spacing and large probe field amplitude used here, the exact frequency of the resonances cannot be verified. However, the measurement proves that we are indeed imaging two BECs that were trapped in separate wells.

7.1.5 *Balancing the Wells*

We have full control over the population ratio of atoms trapped in each well by changing the amplitudes of the two fields that create the upper and lower well, which changes their relative potential energy (see Figure 3.4). We demonstrate this control in Figure 7.4 by changing the amplitude of the 3.6 MHz field. Increasing the amplitude in turn increases the energy of the corresponding well, thus tilting the potential and tipping more atoms into the lower well. Reducing the amplitude, on the other hand, reduces the energy of the upper well, such that a larger fraction of the atom number accumulates in this well. Adjusting the ratio between the two amplitudes thus allows adjusting the ratio of atoms in the upper and lower well. These measurements are similar to the ones in Reference [16], where we demonstrated the same versatility using different adiabatic ramps and larger well separation.

We observe long-term drifts of the population ratio. The change is correlated to drifts in the RF field amplitudes, which will be removed by using active stabilisation. The projection scheme presented here, however, is more robust than the previously used barrier jump ramps, since there is no associated centre-of-mass motion.

7.2 RESONANT TRANSITIONS DURING SPLITTING

As the amplitude ramps are applied, the frequencies at which resonant transitions occur vary. In this section we apply the results from Chapter 5 to the amplitude ramps used for splitting a BEC, and discuss the resulting spectra. We compare the resonant transitions for the projection ramps introduced in Section 7.1.2 to the barrier jump

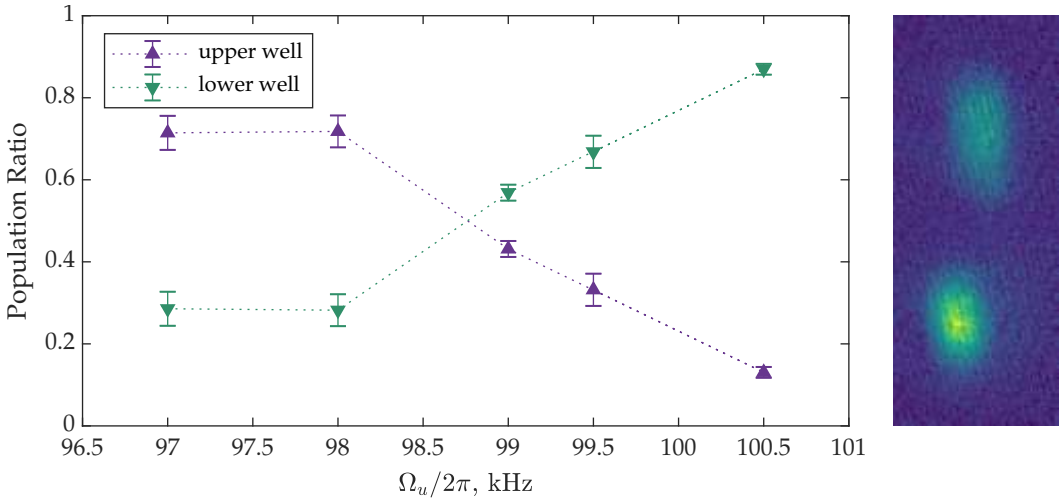

Figure 7.4: Population ratio of atoms in the upper and lower well as a function of Ω_u. The values of the amplitudes Ω_l, and Ω_b are fixed at $2\pi \cdot 120\,\text{kHz}$, and $2\pi \cdot 130\,\text{kHz}$ respectively. The population ratio is the mean of five consecutively taken images, and the error bars corresponds to the standard deviation. To the right is a sample image for $\Omega_u = 2\pi \cdot 99\,\text{kHz}$, with a TOF of 20 ms. Data points are connected as a guide to the eye.

and adiabatic ramps described in Section 7.1.1, demonstrating further advantages of our new projection scheme.

Figure 7.5 shows the transition spectrum versus time for the projection ramps presented in Figure 7.1 and for the barrier jump ramps presented in Reference [25]. For both cases, resonances up to second order are displayed. The general pattern found in Chapter 6 appears, with strong transitions surrounding the Rabi frequency and the dressing frequencies, and second-order transitions being stronger than first for frequencies at half the dressing frequency. To compare the overall effect of noise on the atoms, we also show the transition amplitudes integrated over time in Figure 7.5 (c).

Atoms are initially trapped in an SRF potential, with a limited number of transitions, as apparent in Figure 7.5 (a). As the other two fields are turned on, and atoms are projected into the 3-RF potential, further transitions appear with a fundamental frequency of 200 kHz. As the value of Ω_b is decreased, the resonant frequencies vary. For an amplitude of 200 kHz, the potential exhibits a kink as shown in Figure 7.1 (b). Therefore, $\Omega(\omega_0) = 0$, and the only transitions possible are at ω_f/i, as in Figure 7.5 (a) for a time of 38 ms. The loss at this point does not occur due to RF noise, but rather due to non-adiabatic following of the eigenstates. As the cloud splits after 70 ms, the number of resonances increases further.

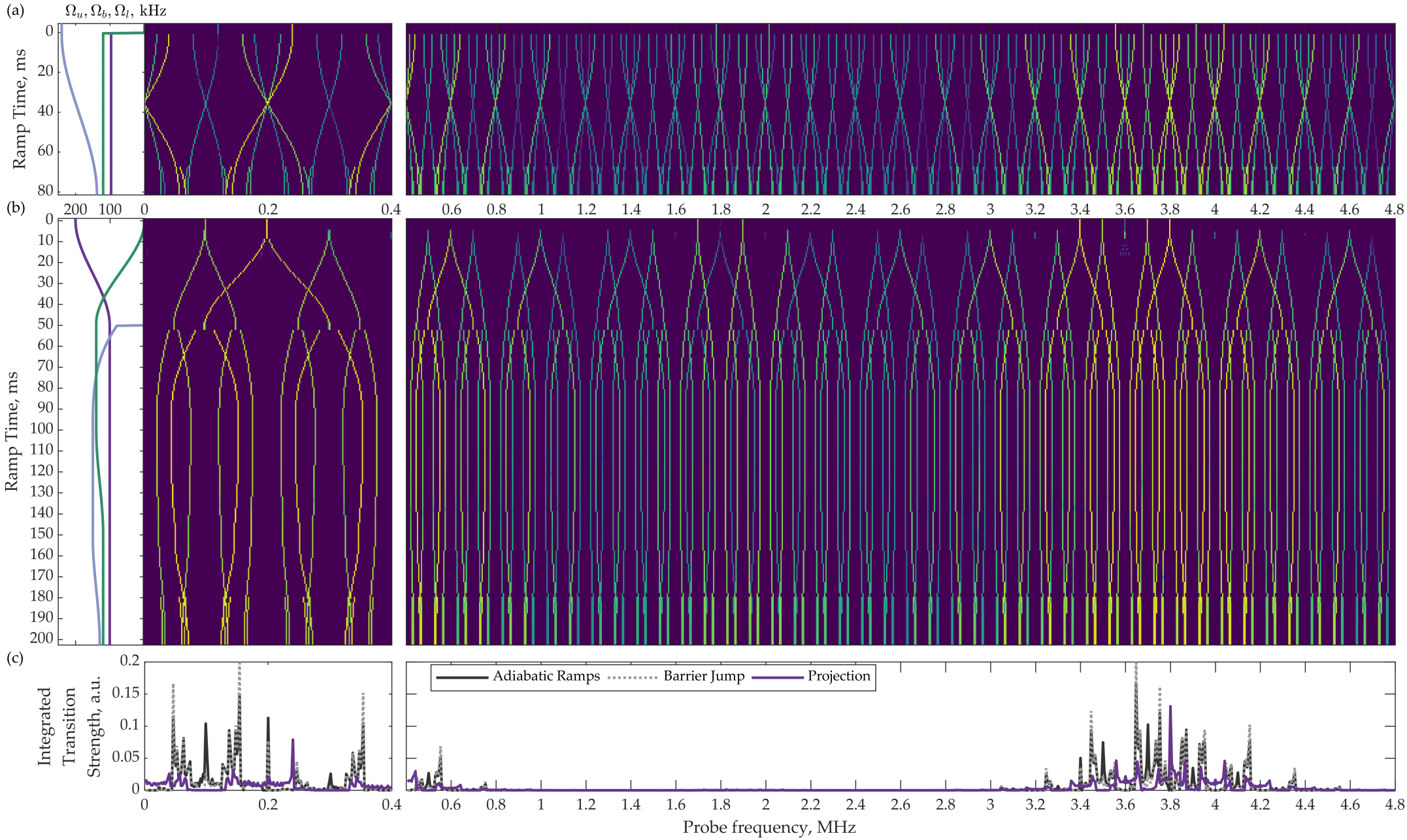

Figure 7.5: Predicted spectra of first- and second-order resonances at the trap minimum as a function of time during the ramp sequences, for $\Omega_+ = \Omega_- = \Omega_z = 2\pi \cdot 10\,\mathrm{kHz}$. Transition strength is indicated by the colour on a logarithmic scale, with yellow indicating the strongest resonances and dark purple indicating that no resonance exists. The amplitude ramps as a function of time are indicated on the left. (a) Projection ramps as discussed in this thesis. (b) Barrier jump ramps as used in [25]. (c) Comparison of the integrated spectra for these two ramps, as well as the completely adiabatic ones, integrated over time in order to compare the overall effect of noise on the atoms.

For the barrier jump ramps, atoms are loaded into the well formed by 3.6 MHz initially, and the amplitude of the field at 4.0 MHz is increased afterwards. This is evident in the spectrum Figure 7.5 (b) as transitions repeating at the fundamental frequency of 400 kHz. Subsequently, the field at a frequency of 3.8 MHz is turned on suddenly with $\Omega_b = 2\pi \cdot 80\,\text{kHz}$. This results in a fundamental frequency of 200 kHz, as evident after 50 ms through the ramps. The amplitude jump causes the discontinuities in the spectrum. During the subsequent amplitude ramps, the resonant frequencies vary again, with further resonances appearing as the cloud splits after a duration of 180 ms.

When comparing the integrated spectra, Figure 7.5 (c), it is immediately obvious that the adiabatic ramps contain more and stronger resonances than the one containing the projection. This is not surprising, given that the latter is of much shorter duration. Not only are the amplitudes in the integrated spectrum reduced, however, resonances also appear at different frequencies, and there are fewer strong resonances.

These integrated spectra can be used to diagnose the cause of loss when performing amplitude ramps. As an example, the integrated spectrum for fully adiabatic ramps is also shown in Figure 7.5. These ramps do not contain the amplitude jump of the barrier field, but the field is turned on smoothly in the same manner as that of the lower well. The amplitude jump had to be introduced to avoid atom loss, as described in Reference [25]. The integrated spectrum points to one potential reason for this loss: a resonance with a frequency of 100 kHz appears very strongly. This is due to the fact that after turning the barrier field on initially, the resonant frequencies stay constant at this value until a barrier value of approximately 70 kHz, leading to a large peak in the integrated spectrum. Changing the ramps, such that e. g. parts of the ramps of Ω_l and Ω_b coincide should avoid this issue, and remove the necessity to jump the value of Ω_b. Calculating integrated spectra for several ramps will enable us to find improved ramps and avoid lengthy experimental optimisation.

7.3 NEXT STEPS

There are currently several limitations to repeatedly achieving evenly split BECs and observing high-contrast interference fringes. Most of these relate to the current implementation of the experimental apparatus, while some are intrinsic to the amplitude ramps presented in this chapter. In this section, we will enumerate these problems and present the steps that should be taken to solve them.

7.3.1 *Shortcomings of the Projection Ramps*

An intrinsic problem of the amplitude ramps presented above is the fact that as the barrier is raised, the potential goes through a point of non-adiabatic loss. We observe that this does not fundamentally prevent splitting of a BEC, and modifications to the amplitude ramps may reduce atom loss even further – one could imagine a ramp that rapidly traverses 200 kHz or even includes a second projection, avoiding the resonance altogether. Machine learning algorithms could help optimise these ramps[2]. The fact that the hottest atoms are most likely to be lost may even prove beneficial.

Additionally, the minima of the potentials before and after projection are vertically displaced, and the trap frequencies are different. We have not observed motion induced on the atoms due to these, and the heating rates must be low since we retain BECs after performing the ramps. Nonetheless it would be better to avoid these jumps. Options include changing the dressing frequency or quadrupole gradient at the same time as the projection. Whether this is experimentally feasible remains to be seen.

7.3.2 *Noise Sources*

RF noise may come from various sources in the laboratory: switch-mode power supplies typically emit spurious frequencies at tens of kHz and harmonics thereof, and the RF generation may cause sidebands to the carrier frequencies. If resonant, these

2 The use of machine learning algorithms is currently being implemented on the experimental apparatus, and has already yielded a four-fold increase in atom number [**Barker2019**, 110]

spurious frequencies cause atom loss, and the projection ramps presented in this thesis are significantly less sensitive as compared to the adiabatic ramps. Calculating the resonances throughout the ramps can be used to diagnose problems, and help to identify noise sources that need to be eliminated.

Furthermore, there is evidence of low-frequency noise driving the motion of the atoms at resonant trap frequencies, which requires further investigation. A combination of filtering and active amplitude stabilisation of the static magnetic field can then be used to reduce this noise.

7.3.3 *Radial Motion*

We observe a radial oscillating motion of the atoms after ramping to a linearly-polarised trapping potential. This prevents overlap of the two clouds in TOF, thus preventing the observation of interference in this work. While tedious, this problem should be straightforward to eliminate. It seems to be caused by different minima of the potentials for circularly- and linearly-polarised dressing fields, probably due to imperfect coil alignment. Adding further dressing fields, e. g. by using the evaporative coil, can compensate this effect [126, 127]. Another approach to solving this problem is to load a thermal cloud of atoms into the linearly-polarised shell and only evaporate to BEC afterwards, thus removing any centre-of-mass motion of the cloud. Evaporation in the shell trap is slower than in the TAAP trap, however, due to the smaller geometric mean trap frequency.

7.3.4 *Atom Number Variation*

Lastly, we have observed variation of atom number and cloud temperature over both short and long time scales. Implementation of a new impedance matching circuit will provide better passive amplitude stability. Active amplitude stabilisation, as mentioned above, will further improve the reliability. Any remaining variation will have to be investigated after these upgrades are implemented.

7.4 CONCLUSION

In this chapter, we have presented a new scheme to split a BEC using MRF-dressed potentials. Contrary to previously used adiabatic ramps, this scheme relies on projecting atoms into an MRF-dressed eigenstate, which reduces the ramp duration. We have calculated the resonant transitions throughout the ramps, showing that these ramps are more robust to extraneous noise. Lastly, we avoid the centre-of-mass motion necessary for the adiabatic splitting scheme, by loading into the centre of the double-well potential initially. There remain some limitations to the scheme, however, mostly related to the current experimental apparatus, and many are shared with the fully adiabatic ramps. Solutions to these problems have been described above. Although we have not yet observed matter-wave interference using the projection ramps, their advantages over the adiabatic ramps encourage further investigation and they promise to be a marked improvement to previous methods.

8

CONCLUSION AND OUTLOOK

The work in this thesis was directed towards proposed experiments to investigate NEQ physics and thermalisation of 2D systems, and details of how these experiments will be implemented on our experimental apparatus have been given. 2D systems are especially interesting as they bridge the gap between integrable 1D systems that are dominated by quantum fluctuations, and 3D systems that are governed by interactions. We propose to investigate thermalisation of 2D systems by coherently splitting and re-interfering a cloud of ultracold atoms confined in RF-dressed potentials. Analysing the fluctuations in the phase of the interference fringes promises a wealth of information on the NEQ dynamics [31, 47].

We have presented the experimental apparatus that we use to trap ultracold atoms in pancake-shaped RF-dressed potentials, and how this has been used to split a BEC using multiple dressing frequencies. We have argued that these potentials are well-suited to carrying out the experiments we have proposed. We have presented first results of atoms trapped in a combination of a red-detuned optical dipole trap and an RF-dressed potential and have elaborated how this system can be used to achieve the experiments proposed in Chapter 2.

One limitation of the current implementation is that atom loss is suffered for atoms trapped in the 2D regime, or when adding multiple dressing frequencies. We attribute this loss to spurious RF frequencies. In searching to understand the spectrum of MRF-dressed atoms we have described multi-frequency transitions which are interesting to a wide range of phenomena, and have investigated these experimentally. We find perfect agreement between predicted and observed transition frequencies. Limita-

tions of the experimental measurements did not allow a quantitative comparison between transition amplitudes, but we find qualitative agreement. Furthermore, we uncover previously unknown transitions and explain their existence theoretically by the non-linearity of the Zeeman effect. These results are essential for diagnosing loss on current experiments, and for planning new experimental setups. Furthermore, the theoretical framework is widely applicable to multi-frequency systems and can be extended further to cover spontaneous emission or quantum fluctuations.

Finally, we have presented a new method to split a BEC in an MRF-dressed potential. We project atoms trapped in an SRF-dressed potential into one formed by multiple frequencies and verify our understanding of the dressed eigenstates by observing the fraction of atoms projected into each dressed eigenstate of the new potential. These measurements provide a basis for further investigations into developing better amplitude ramps for splitting BECs. They open a promising path towards splitting that does not rely on adiabatic ramps, thus significantly reducing the duration and range of resonant frequencies throughout the ramps.

This final chapter gives details of the remaining steps towards observing thermalisation in two dimensions and concludes by describing further interesting experiments that could be carried out on our apparatus.

8.1 REMAINING STEPS TOWARDS OBSERVING THERMALISATION

This thesis provides the groundwork for observing thermalisation in 2D systems, proposing the experiments and how they can be carried out on the experimental apparatus. The path forward is clear: using the results on transitions between RF-dressed states, spurious frequencies that are detrimental to the potentials we use can be identified, and either removed or avoided if necessary. In combination with improved frequency generation and impedance matching, this will allow trapping of condensed clouds in 2D confinement with lifetimes sufficient for coherent splitting. Based on the results from Reference [25] and the ramps presented in this thesis, those clouds can then be split coherently, and matter-wave interference observed. These steps are detailed in Chapter 7, and are largely straightforward technical im-

provements. Changes to the imaging system will enhance the visibility of interference fringes and allow the determination of the integrated contrast. In combination, these will allow the first observation of thermalisation in 2D systems via the method proposed in Chapter 2.

The versatility of the MRF-dressed potentials provide further possibilities: for certain combinations of quadrupole gradient and RF field amplitude, the radial confinement is quartic rather than harmonic, resulting in a larger region of nearly-homogeneous density and facilitating comparison to theory. If vastly different amplitudes are used for the fields generating the two wells, 2D confinement in one well can be combined with a 3D gas in the other well, providing a constant phase reference.

Once the RF amplitudes are stabilised sufficiently, tunnelling between neighbouring wells will be possible, further increasing the range of observable phenomena. Lastly, adding a dipole trap increases the range of possible experiments, as described in Section 4.4.

8.2 OTHER POSSIBLE EXPERIMENTS

In this thesis we have investigated transitions in RF-dressed potentials and argued that these are well-suited to investigating thermalisation in 2D gases. The experimental setup provides a basis for cold-atom experiments in two and three dimensions, and we conclude this thesis by listing a few specific applications that will be possible once the technical upgrades are implemented.

As argued in Section 4.4, adding the optical dipole trap gives access to a wide range of experiments. For example, stirring a 2D cloud with a red-detuned laser beam is of interest to contrast the findings with a blue-detuned scanned dipole trap [140].

A special feature of multiple wells, created using RF-dressed potentials, is the ability to rotate atoms in each well independently by varying the polarisation of the RF field that forms it. One cloud can remain stationary or the clouds can counter-rotate. The intricate interference patterns, formed after expansion, provide detailed information, e. g. on the existence of phantom vortices [141].

Once we have achieved quantum tunneling between the two wells, this opens up access to a wide range of experiments. An example is making a system governed by a Hamiltonian corresponding to the sine-Gordon equation [69]. Another interesting option is to induce rotation in one of the two coupled clouds, causing vortices to appear. It has been proposed that the angular momentum will be able to tunnel to the second cloud [142].

Combining non-destructive imaging methods such as Faraday imaging with atoms trapped in MRF-dressed potentials is another promising prospect. Non-destructive imaging has been used to observe the dressing frequency [144]. We plan to combine Faraday imaging with our double-well potential. This will allow non-destructive observation of the number of atoms trapped in each well. An application of this scheme is to create squeezing and improve interferometric measurements. In the context of this thesis, the imaging could be used to post-select only those images of interference that result from a certain ratio of atoms trapped in the two wells, or even to apply feedback to the potential, thus improving the reliability of loading a given ratio of atoms into the two wells. The detailed work that we reported in this thesis provides the foundation for this great range of new experiments.

APPENDICES

A

TRANSFORMING THE PROBE INTERACTION

To calculate matrix elements of the probe interaction in the eigenbasis of H_1, we rewrite V_p in this basis. We start by diagonalising the Hamiltonian describing a spin-1/2 particle interacting with a circularly-polarised SRF dressing field and then rewriting the probe interaction in the eigenbasis of H_1. Finally, we argue that this transformed probe describes any spin.

A.1 DIAGONALISATION OF H_1

As for $F = 1$, for spin-1/2 particles the Hamiltonian is block-diagonal and we can thus write H_1 as the following tensor product, analogously to Equation 3.9:

$$H_1 = \mathbb{1}_k \otimes \mathbb{1}_\mathrm{p} \otimes \frac{\hbar}{2} \begin{pmatrix} \Delta & \Omega_0 \\ \Omega_0 & -\Delta \end{pmatrix} + \hbar\hat{k}\omega_\mathrm{rf} \otimes \hbar\hat{N}_\mathrm{p}\omega_\mathrm{p} \otimes \mathbb{1}_\mathrm{atom}, \tag{A.1}$$

in the basis where $|k\rangle \otimes \left|N_\mathrm{p}\right\rangle \otimes \binom{1}{0}$ denotes states with $m_F = 1/2$ and $|k\rangle \otimes \left|N_\mathrm{p}\right\rangle \otimes \binom{0}{1}$ denotes states with $m_F = -1/2$. The detuning Δ is defined as $\Delta := \omega_\mathrm{rf} - \omega_0$ and $\mathbb{1}_\mathrm{p}, \mathbb{1}_k$ are the identity on the probe field and the manifold number respectively.

We can then diagonalise H_1 and find the eigenvalues $E_\pm = \pm\frac{1}{2}\sqrt{\Delta^2 + \Omega_0^2}$ and eigenstates

$$\begin{aligned} \left|k = N - 1/2, N_\mathrm{p}, 1/2\right\rangle_1 &= \mathcal{N}\left((\Delta + \Omega)\left|N, N_\mathrm{p}, 1/2\right\rangle_0 + \Omega_0\left|N-1, N_\mathrm{p}, -1/2\right\rangle_0\right), \\ \left|k = N - 1/2, N_\mathrm{p}, -1/2\right\rangle_1 &= \mathcal{N}\left(-\Omega_0\left|N, N_\mathrm{p}, 1/2\right\rangle_0 + (\Omega + \Delta)\left|N-1, N_\mathrm{p}, -1/2\right\rangle_0\right), \end{aligned}$$

where we have introduced the generalised Rabi frequency $\Omega^2 := \Omega(\omega_0)^2 = \Omega_0^2 + \Delta^2$ and a normalisation factor $\mathcal{N} := (2\Omega(\Omega + \Delta))^{-1/2}$.

A.2 TRANSFORMING V_P

The unitary transformation U transforms between the eigenbasis of H_0 and the eigenbasis of H_1:

$$\begin{aligned} U = \sum_{N_\mathrm{p}, N} \mathcal{N} \Big[& (\Omega + \Delta) \big(\left|N, N_\mathrm{p}, 1/2\right\rangle_{0\ 1}\!\left\langle k = N - 1/2, N_\mathrm{p}, 1/2\right| \\ & + \left|N-1, N_\mathrm{p}, -1/2\right\rangle_{0\ 1}\!\left\langle k = N - 1/2, N_\mathrm{p}, -1/2\right| \big) \\ & - \Omega_0 \left|N, N_\mathrm{p}, 1/2\right\rangle_{0\ 1}\!\left\langle k = N - 1/2, N_\mathrm{p}, -1/2\right| \\ & + \Omega_0 \left|N-1, N_\mathrm{p}, -1/2\right\rangle_{0\ 1}\!\left\langle k = N - 1/2, N_\mathrm{p}, 1/2\right| \Big]. \end{aligned} \tag{A.2}$$

Using the above basis for the eigenstates of H_0, and denoting states with $m = 1/2$ by $|k\rangle \otimes \left|N_\mathrm{p}\right\rangle \otimes \binom{1}{0}$, and states with $m = -1/2$ by $|k\rangle \otimes \left|N_\mathrm{p}\right\rangle \otimes \binom{0}{1}$ in the eigenbasis of H_1, U becomes:

$$U = \mathbb{1}_k \otimes \mathbb{1}_\mathrm{p} \otimes \begin{pmatrix} \Delta + \Omega & -\Omega_0 \\ \Omega_0 & \Delta + \Omega \end{pmatrix}. \tag{A.3}$$

We define spin operators acting on the two-level system within each manifold:

$$\begin{aligned} S_+ &= \left|k, N_\mathrm{p}, 1/2\right\rangle_{1\ 1}\!\left\langle k, N_\mathrm{p}, -1/2\right|, \\ S_- &= \left|k, N_\mathrm{p}, -1/2\right\rangle_{1\ 1}\!\left\langle k, N_\mathrm{p}, 1/2\right|, \\ S_z &= \frac{1}{2}\left(\left|k, N_\mathrm{p}, 1/2\right\rangle_{1\ 1}\!\left\langle k, N_\mathrm{p}, 1/2\right| - \left|k, N_\mathrm{p}, -1/2\right\rangle_{1\ 1}\!\left\langle k, N_\mathrm{p}, -1/2\right| \right), \end{aligned}$$

and normalised raising and lowering operators for the manifold number $\widetilde{b}^\dagger, \widetilde{b}$ such that $\widetilde{b}^\dagger \left|k, N_\mathrm{p}, m\right\rangle_1 = \left|k+1, N_\mathrm{p}, m\right\rangle_1$ and $\widetilde{b} \left|k, N_\mathrm{p}, m\right\rangle_1 = \left|k-1, N_\mathrm{p}, m\right\rangle_1$. Using these definitions we can rewrite the probe interaction as follows:

$$\begin{aligned} V_\mathrm{p} \to U^\dagger V_\mathrm{p} U = \frac{1}{2\Omega}\Big[&\left(\Omega_z \widetilde{a}_\mathrm{p} + \Omega_z^* \widetilde{a}_\mathrm{p}^\dagger\right)\left(2\Delta S_z - \Omega_0 \left(S_+ + S_-\right)\right) + \\ &\frac{1}{2}\Big(\Omega_+ \widetilde{a}_\mathrm{p} \widetilde{b}\left((\Omega+\Delta)S_+ + 2\Omega_0 S_z - (\Omega-\Delta)S_-\right) + \\ &\Omega_+^* \widetilde{a}_\mathrm{p}^\dagger \widetilde{b}^\dagger\left((\Omega+\Delta)S_- + 2\Omega_0 S_z - (\Omega-\Delta)S_+\right)\Big) + \\ &\frac{1}{2}\Big(\Omega_- \widetilde{a}_\mathrm{p} \widetilde{b}^\dagger\left((\Omega+\Delta)S_- + 2\Omega_0 S_z - (\Omega-\Delta)S_+\right) + \\ &\Omega_-^* \widetilde{a}_\mathrm{p}^\dagger \widetilde{b}\left((\Omega+\Delta)S_+ + 2\Omega_0 S_z - (\Omega-\Delta)S_-\right)\Big)\Big]. \end{aligned}$$

A.3 EXTENSION TO ANY SPIN

This result also holds for a spin-1 system, such as for ^{87}Rb atoms in the F=1 hyperfine state as used in our experiment. To prove this, consider addition of angular momenta using tensor products, replacing the spin-1/2 operators with the corresponding spin-1 operators. These can be written in terms of spin-1/2 operators as follows: $S_{\pm,z}^{(1)} = S_{\pm,z}^{(1/2)} \otimes \mathbb{1} + \mathbb{1} \otimes S_{\pm,z}^{(1/2)}$. The probe interaction for $F = 1$, $V_\mathrm{p}^{(1)}$, is separable, which means that the form of the probe in the basis of eigenstates of H_1 stays the same.

Note that while the form of the transformed probe is exactly the same, the action of these operators on states is modified by the Clebsch-Gordan coefficients, e. g. for spin-1/2 we have $S_+ \left|k, N_\mathrm{p}, -1/2\right\rangle_1 = \left|k, N_\mathrm{p}, 1/2\right\rangle_1$, but for spin-1 we have $S_+ \left|k, N_\mathrm{p}, -1\right\rangle_1 = \sqrt{2}\left|k, N_\mathrm{p}, 0\right\rangle_1$.

B

TRANSITION AMPLITUDE FOR $\omega_p = \Omega/3$

We calculate the full effective Rabi frequency for the third-order transition with $\omega_p = \Omega/3$, using the probe interaction in the form of Equation 5.13 and Equations 5.8 and 5.5. That is, we include all paths shown in Figure 5.4 (a), resulting in an effective Rabi frequency of:

$$
\begin{aligned}
\Omega_{\text{eff}} = \frac{9\Omega_0}{2^4\Omega^5}(\Omega_0^2 - 8\Delta^2)\Omega_z^{*3} \\
&-\frac{1}{2^3}\frac{\Omega_0}{\Omega^3}\Omega_+^*\Omega_-^*\Omega_z^*\Bigg[(\Omega-\Delta)^2\left(\frac{3}{2\Omega}\left(\frac{1}{\omega_{\text{rf}}+\frac{4\Omega}{3}}-\frac{2}{\omega_{\text{rf}}+\frac{2\Omega}{3}}\right)+\frac{1}{\omega_{\text{rf}}+\frac{2\Omega}{3}}\frac{1}{\omega_{\text{rf}}+\frac{4\Omega}{3}}\right) \\
&+(\Omega+\Delta)^2\left(\frac{3}{2\Omega}\left(\frac{2}{\omega_{\text{rf}}-\frac{2\Omega}{3}}-\frac{1}{\omega_{\text{rf}}-\frac{4\Omega}{3}}\right)+\frac{1}{\omega_{\text{rf}}-\frac{2\Omega}{3}}\frac{1}{\omega_{\text{rf}}-\frac{4\Omega}{3}}\right) \\
&+\Omega_0^2\left(\frac{3}{4\Omega}\left(\frac{1}{\omega_{\text{rf}}-\frac{2\Omega}{3}}-\frac{1}{\omega_{\text{rf}}+\frac{2\Omega}{3}}\right)+\frac{3}{\Omega}\left(\frac{1}{\omega_{\text{rf}}+\frac{\Omega}{3}}-\frac{1}{\omega_{\text{rf}}-\frac{\Omega}{3}}\right)-2\frac{1}{\omega_{\text{rf}}-\frac{2\Omega}{3}}\frac{1}{\omega_{\text{rf}}+\frac{2\Omega}{3}}\right) \\
&+2\Delta\Bigg(-(\Omega+\Delta)\left(\frac{1}{\omega_{\text{rf}}-\frac{\Omega}{3}}\frac{1}{\omega_{\text{rf}}-\frac{2\Omega}{3}}-\frac{3}{\Omega}\frac{1}{\omega_{\text{rf}}-\frac{2\Omega}{3}}\right) \\
&+(\Omega-\Delta)\left(\frac{1}{\omega_{\text{rf}}+\frac{\Omega}{3}}\frac{1}{\omega_{\text{rf}}+\frac{2\Omega}{3}}+\frac{3}{\Omega}\frac{1}{\omega_{\text{rf}}+\frac{2\Omega}{3}}\right)\Bigg)\Bigg].
\end{aligned}
\tag{B.1}
$$

BIBLIOGRAPHY

[1] T. W. B. Kibble. "Topology of cosmic domains and strings". In: *Journal of Physics A* 9.8 (1976), pp. 1387–1398 (cited on pp. 1, 10).

[2] A. Polkovnikov, K. Sengupta, A. Silva, and M. Vengalattore. "Colloquium: Nonequilibrium dynamics of closed interacting quantum systems". In: *Reviews of Modern Physics* 83.3 (2011), pp. 863–883 (cited on p. 1).

[3] C. Gogolin and J. Eisert. "Equilibration, thermalisation, and the emergence of statistical mechanics in closed quantum systems". In: *Reports on Progress in Physics* 79 (2016), p. 056001 (cited on p. 1).

[4] M. A. Cazalilla and M. Rigol. "Focus on Dynamics and Thermalization in Isolated Quantum Many-Body Systems". In: *New Journal of Physics* 12 (2010), p. 055006 (cited on p. 1).

[5] J. Eisert, M. Friesdorf, and C. Gogolin. "Quantum many-body systems out of equilibrium". In: *Nature Physics* 11 (2015), pp. 124–130 (cited on p. 1).

[6] S. Trotzky, Y.-A. Chen, A. Flesch, I. P. McCulloch, U. Schollwöck, J. Eisert, and I. Bloch. "Probing the relaxation towards equilibrium in an isolated strongly correlated one-dimensional Bose gas". In: *Nature Physics* 8 (2012), pp. 325–330 (cited on p. 1).

[7] D. Barredo, S. de Léséleuc, V. Lienhard, T. Lahaye, and A. Browaeys. "An atom-by-atom assembler of defect-free arbitrary two-dimensional atomic arrays". In: *Science* 354.6315 (2016), pp. 1021–1023 (cited on p. 1).

[8] H. Labuhn, D. Barredo, S. Ravets, S. de Léséleuc, T. Macrì, T. Lahaye, and A. Browaeys. "Tunable two-dimensional arrays of single Rydberg atoms for realizing quantum Ising models". In: *Nature* 534 (2016), pp. 667–670 (cited on p. 1).

[9] N. Navon, A. L. Gaunt, R. P. Smith, and Z. Hadzibabic. "Emergence of a turbulent cascade in a quantum gas". In: *Nature* 539 (2016), pp. 72–75 (cited on p. 1).

[10] J.-Y. Choi, S. Hild, J. Zeiher, P. Schauß, A. Rubio-Abadal, T. Yefsah, V. Khemani, D. A. Huse, I. Bloch, and C. Gross. "Exploring the many-body localization transition in two dimensions". In: *Science* 352.6293 (2016), pp. 1547–1552 (cited on p. 1).

[11] P. Jurcevic, H. Shen, P. Hauke, C. Maier, T. Brydges, C. Hempel, B. P. Lanyon, M. Heyl, R. Blatt, and C. F. Roos. "Direct Observation of Dynamical Quantum Phase Transitions in an Interacting Many-Body System". In: *Physical Review Letters* 119.8 (2017), p. 080501 (cited on p. 1).

[12] M. Gring, M. Kuhnert, T. Langen, T. Kitagawa, B. Rauer, M. Schreitl, I. Mazets, D. Adu Smith, E. Demler, and J. Schmiedmayer. "Relaxation and Prethermalization in an Isolated Quantum System". In: *Science* 337.6100 (2012), pp. 1318–1322 (cited on pp. 2, 3, 7, 9, 13, 33).

[13] A. Mazurenko, C. S. Chiu, G. Ji, M. F. Parsons, M. Kanász-Nagy, R. Schmidt, F. Grusdt, E. Demler, D. Greif, and M. Greiner. "A cold-atom Fermi–Hubbard antiferromagnet". In: *Nature* 545 (2017), pp. 462–466 (cited on p. 2).

[14] M. F. Parsons, A. Mazurenko, C. S. Chiu, G. Ji, D. Greif, and M. Greiner. "Site-resolved measurement of the spin-correlation function in the Fermi-Hubbard model". In: *Science* 353.6305 (2016), pp. 1253–1256 (cited on p. 2).

[15] O. Zobay and B. M. Garraway. "Two-Dimensional Atom Trapping in Field-Induced Adiabatic Potentials". In: *Physical Review Letters* 86.7 (2001), pp. 1195–1198 (cited on pp. 2, 10, 17).

[16] T. L. Harte, E. Bentine, K. Luksch, A. J. Barker, D. Trypogeorgos, B. Yuen, and C. J. Foot. "Ultracold atoms in multiple radio-frequency dressed adiabatic potentials". In: *Physical Review A* 97.1 (2018), p. 013616 (cited on pp. 2, 3, 10, 22, 25, 29, 33, 38, 49, 75, 88, 102).

[17] M. Fleischhauer, A. Imamoglu, and J. P. Marangos. "Electromagnetically induced transparency: Optics in coherent media". In: *Reviews of Modern Physics* 77.2 (2005), pp. 633–673.

[18] N. Bloembergen. *Nonlinear optics*. World Scientific, 1996.

[19] R. C. Prince, R. R. Frontiera, and E. O. Potma. "Stimulated Raman Scattering: From Bulk to Nano". In: *Chemical Reviews* 117.7 (2017), pp. 5070–5094.

[20] C. L. Evans and X. S. Xie. "Coherent Anti-Stokes Raman Scattering Microscopy: Chemical Imaging for Biology and Medicine". In: *Annual Review of Analytical Chemistry* 1.1 (2008), pp. 883–909.

[21] J. Sebby-Strabley, M. Anderlini, P. S. Jessen, and J. V. Porto. "Lattice of double wells for manipulating pairs of cold atoms". In: *Physical Review A* 73.3 (2006), p. 033605 (cited on p. 2).

[22] G.-B. Jo, J. Guzman, C. K. Thomas, P. Hosur, A. Vishwanath, and D. M. Stamper-Kurn. "Ultracold Atoms in a Tunable Optical Kagome Lattice". In: *Physical Review Letters* 108.4 (2012), p. 045305 (cited on p. 2).

[23] L. J. LeBlanc and J. H. Thywissen. "Species-specific optical lattices". In: *Physical Review A* 75.5 (2007), p. 053612 (cited on p. 2).

[24] P. W. Courteille, B. Deh, J. Fortágh, A. Günther, S. Kraft, C. Marzok, S. Slama, and C. Zimmermann. "Highly versatile atomic micro traps generated by multifrequency magnetic field modulation". In: *Journal of Physics B* 39.5 (2006), pp. 1055–1064 (cited on pp. 2, 73, 94).

[25] E. Bentine. "Atomic Mixtures in Radiofrequency Dressed Potentials". DPhil thesis. University of Oxford, 2018 (cited on pp. 2, 22, 25, 26, 34, 36–38, 40, 41, 46, 50, 62, 76, 81, 86, 88, 95, 96, 100, 103–105, 110).

[26] K. Merloti, R. Dubessy, L. Longchambon, A. Perrin, P.-E. Pottie, V. Lorent, and H. Perrin. "A two-dimensional quantum gas in a magnetic trap". In: *New Journal of Physics* 15.3 (2013), p. 033007 (cited on pp. 3, 8, 10, 30, 31, 33).

[27] D. Adu Smith, M. Gring, T. Langen, M. Kuhnert, B. Rauer, R. Geiger, T. Kitagawa, I. Mazets, E. Demler, and J. Schmiedmayer. "Prethermalization revealed by the relaxation dynamics of full distribution functions". In: *New Journal of Physics* 15.7 (2013), p. 075011 (cited on pp. 3, 7, 9).

[28] V. . L. Berezinskii. "Destruction of Long-range Order in One-dimensional and Two-dimensional Systems Possessing a Continuous Symmetry Group. II. Quantum Systems." In: *Journal of Experimental and Theoretical Physics* 34.3 (1972), p. 610 (cited on pp. 3, 8).

[29] J. M. Kosterlitz and D. J. Thouless. "Ordering, metastability and phase transitions in two-dimensional systems". In: *Journal of Physics C* 6.7 (1973), pp. 1181–1203 (cited on pp. 3, 8).

[30] A. Polkovnikov, E. Altman, and E. Demler. "Interference between independent fluctuating condensates". In: *Proceedings of the National Academy of Sciences* 103.16 (2006), pp. 6125–6129 (cited on pp. 10, 11, 13, 14).

[31] A. Imambekov, V. Gritsev, and E. Demler. "Fundamental noise in matter interferometers". In: *Ultra-cold Fermi Gases*. Vol. 164. Proceedings of the International School of Physics "Enrico Fermi". 2007, pp. 535–606 (cited on pp. 10–15, 109).

[32] J. Berges, S. Borsányi, and C. Wetterich. "Prethermalization". In: *Physical Review Letters* 93.14 (2004), p. 142002 (cited on p. 6).

[33] C. J. Foot. *Investigating non-equilibrium physics and universality using two-dimensional quantum gases*. `https://gow.epsrc.ukri.org/NGBOViewGrant.aspx?GrantRef=EP/S013105/1`. 2018 (cited on pp. 6, 11, 14).

[34] L. D'Alessio, Y. Kafri, A. Polkovnikov, and M. Rigol. "From quantum chaos and eigenstate thermalization to statistical mechanics and thermodynamics". In: *Advances in Physics* 65.3 (2016), pp. 239–362 (cited on pp. 6, 7).

[35] J. M. Deutsch. "Quantum statistical mechanics in a closed system". In: *Physical Review A* 43.4 (1991), pp. 2046–2049 (cited on p. 7).

[36] M. Srednicki. "Chaos and quantum thermalization". In: *Physical Review E* 50.2 (1994), pp. 888–901 (cited on p. 7).

[37] M. Rigol, V. Dunjko, and M. Olshanii. "Thermalization and its mechanism for generic isolated quantum systems". In: *Nature* 452 (2008), pp. 854–858 (cited on p. 7).

[38] R. Steinigeweg, A. Khodja, H. Niemeyer, C. Gogolin, and J. Gemmer. "Pushing the Limits of the Eigenstate Thermalization Hypothesis towards Mesoscopic Quantum Systems". In: *Physical Review Letters* 112.13 (2014), p. 130403 (cited on p. 7).

[39] A. M. Kaufman, M. Eric Tai, A. Lukin, M. Rispoli, R. Schittko, P. M. Preiss, and M. Greiner. "Quantum thermalization through entanglement in an isolated many-body system". In: *Science* 353.6301 (2016), pp. 794–800 (cited on p. 7).

[40] E. Fermi, P. Pasta, S. Ulam, and M. Tsingou. *Studies of the nonlinear problems*. Technical Report. Los Alamos Scientific Lab., N. Mex., 1955 (cited on p. 7).

[41] T. Kinoshita, T. Wenger, and D. S. Weiss. "A quantum Newton's cradle". In: *Nature* 440 (2006), pp. 900–903 (cited on p. 7).

[42] T. Langen, R. Geiger, M. Kuhnert, B. Rauer, and J. Schmiedmayer. "Local emergence of thermal correlations in an isolated quantum many-body system". In: *Nature Physics* 9 (2013), pp. 640–643 (cited on pp. 7, 9).

[43] T. Langen, S. Erne, R. Geiger, B. Rauer, T. Schweigler, M. Kuhnert, W. Rohringer, I. E. Mazets, T. Gasenzer, and J. Schmiedmayer. "Experimental observation of a generalized Gibbs ensemble". In: *Science* 348.6231 (2015), pp. 207–211 (cited on pp. 7, 9).

[44] T. Schweigler, V. Kasper, S. Erne, I. Mazets, B. Rauer, F. Cataldini, T. Langen, T. Gasenzer, J. Berges, and J. Schmiedmayer. "Experimental characterization of a quantum many-body system via higher-order correlations". In: *Nature* 545 (2017), pp. 323–326 (cited on pp. 7, 9, 15).

[45] M. Pigneur, T. Berrada, M. Bonneau, T. Schumm, E. Demler, and J. Schmiedmayer. "Relaxation to a Phase-Locked Equilibrium State in a One-Dimensional

Bosonic Josephson Junction". In: *Physical Review Letters* 120.17 (2018), p. 173601 (cited on pp. 7, 9).

[46] B. Rauer, S. Erne, T. Schweigler, F. Cataldini, M. Tajik, and J. Schmiedmayer. "Recurrences in an isolated quantum many-body system". In: *Science* 360.6386 (2018), pp. 307–310 (cited on pp. 7, 13, 42).

[47] L. Mathey and A. Polkovnikov. "Light cone dynamics and reverse Kibble-Zurek mechanism in two-dimensional superfluids following a quantum quench". In: *Physical Review A* 81.3 (2010), p. 033605 (cited on pp. 8, 9, 11, 12, 109).

[48] R. S. Kagiwada, J. C. Fraser, I. Rudnick, and D. Bergman. "Superflow in Helium Films: Third-Sound Measurements". In: *Physical Review Letters* 22.8 (1969), pp. 338–342 (cited on p. 8).

[49] D. J. Bishop and J. D. Reppy. "Study of the Superfluid Transition in Two-Dimensional ^{4}He Films". In: *Physical Review Letters* 40.26 (1978), pp. 1727–1730 (cited on p. 8).

[50] A. F. Hebard and A. T. Fiory. "Evidence for the Kosterlitz-Thouless Transition in Thin Superconducting Aluminum Films". In: *Physical Review Letters* 44.4 (1980), pp. 291–294 (cited on p. 8).

[51] D. J. Resnick, J. C. Garland, J. T. Boyd, S. Shoemaker, and R. S. Newrock. "Kosterlitz-Thouless Transition in Proximity-Coupled Superconducting Arrays". In: *Physical Review Letters* 47.21 (1981), pp. 1542–1545 (cited on p. 8).

[52] A. I. Safonov, S. A. Vasilyev, I. S. Yasnikov, I. I. Lukashevich, and S. Jaakkola. "Observation of Quasicondensate in Two-Dimensional Atomic Hydrogen". In: *Physical Review Letters* 81.21 (1998), pp. 4545–4548 (cited on p. 8).

[53] A. Görlitz et al. "Realization of Bose-Einstein Condensates in Lower Dimensions." In: *Physical Review Letters* 87.13 (2001), p. 130402 (cited on p. 8).

[54] S. Burger, F. S. Cataliotti, C. Fort, P. Maddaloni, F. Minardi, and M. Inguscio. "Quasi-2D Bose-Einstein condensation in an optical lattice". In: *Europhysics Letters* 57.1 (2002) (cited on p. 8).

[55] D. Rychtarik, B. Engeser, H.-C. Nägerl, and R. Grimm. "Two-Dimensional Bose-Einstein Condensate in an Optical Surface Trap". In: *Physical Review Letters* 92.17 (2004), p. 173003 (cited on p. 8).

[56] Z. Hadzibabic, S. Stock, B. Battelier, V. Bretin, and J. Dalibard. "Interference of an Array of Independent Bose-Einstein Condensates". In: *Physical Review Letters* 93.18 (2004), p. 180403 (cited on p. 8).

[57] N. L. Smith, W. H. Heathcote, G. Hechenblaikner, E. Nugent, and C. J. Foot. "Quasi-2D confinement of a BEC in a combined optical and magnetic potential". In: *Journal of Physics B* 38.3 (2005), pp. 223–235 (cited on p. 8).

[58] M. Köhl, H. Moritz, T. Stöferle, C. Schori, and T. Esslinger. "Superfluid to Mott insulator transition in one, two, and three dimensions". In: *Journal of Low Temperature Physics* 138.3-4 (2005), pp. 635–644 (cited on p. 8).

[59] P. Cladé, C. Ryu, A. Ramanathan, K. Helmerson, and W. D. Phillips. "Observation of a 2D Bose Gas: From Thermal to Quasicondensate to Superfluid". In: *Physical Review Letters* 102.17 (2009), p. 170401 (cited on p. 8).

[60] J. I. Gillen, W. S. Bakr, A. Peng, P. Unterwaditzer, S. Fölling, and M. Greiner. "Two-dimensional quantum gas in a hybrid surface trap". In: *Physical Review A* 80.2 (2009), p. 021602 (cited on p. 8).

[61] Z. Hadzibabic and J. Dalibard. "Two-dimensional Bose fluids: An atomic physics perspective". In: *La Rivista del Nuovo Cimento* 34.6 (2011) (cited on pp. 8, 9).

[62] J. V. José, ed. *40 Years of Berezinskii-Kosterlitz-Thouless Theory*. World Scientific, 2013 (cited on pp. 8, 9).

[63] Z. Hadzibabic, P. Krüger, M. Cheneau, B. Battelier, and J. Dalibard. "Berezinskii–Kosterlitz–Thouless crossover in a trapped atomic gas". In: *Nature* 441 (2006), pp. 1118–1121 (cited on pp. 9, 13–15).

[64] J.-Y. Choi, S. W. Seo, and Y.-I. Shin. "Observation of Thermally Activated Vortex Pairs in a Quasi-2D Bose Gas". In: *Physical Review Letters* 110.17 (2013), p. 175302 (cited on pp. 9, 10, 15).

[65] A. A. Burkov, M. D. Lukin, and E. Demler. "Decoherence dynamics in low-dimensional cold atom interferometers". In: *Physical Review Letters* 98.20 (2007), p. 200404 (cited on p. 9).

[66] L. Mathey, K. J. Günter, J. Dalibard, and A. Polkovnikov. "Dynamic Kosterlitz-Thouless transition in two-dimensional Bose mixtures of ultracold atoms". In: *Physical Review A* 95.5 (2017), p. 053630 (cited on pp. 9, 12).

[67] W. H. Zurek. "Cosmological experiments in superfluid helium?" In: *Nature* 317 (1985), pp. 505–508 (cited on p. 10).

[68] L. Mathey, A. Polkovnikov, and A. H. Castro Neto. "Phase-locking transition of coupled low-dimensional superfluids". In: *Europhysics Letters* 81.1 (2008), p. 10008 (cited on p. 12).

[69] E. G. Dalla Torre, E. Demler, and A. Polkovnikov. "Universal Rephasing Dynamics after a Quantum Quench via Sudden Coupling of Two Initially Independent Condensates". In: *Physical Review Letters* 110.9 (2013), p. 090404 (cited on pp. 12, 112).

[70] M. R. Andrews, C. G. Townsend, H.-J. Miesner, D. S. Durfee, D. M. Kurn, and W. Ketterle. "Observation of Interference Between Two Bose Condensates". In: *Science* 275.5300 (1997), pp. 637–641 (cited on p. 13).

[71] Y. Shin, M. Saba, T. A. Pasquini, W. Ketterle, D. E. Pritchard, and A. E. Leanhardt. "Atom Interferometry with Bose-Einstein Condensates in a Double-Well Potential". In: *Physical Review Letters* 92.5 (2004), p. 050405 (cited on p. 13).

[72] S. Hofferberth, I. Lesanovsky, T. Schumm, A. Imambekov, V. Gritsev, E. Demler, and J. Schmiedmayer. "Probing quantum and thermal noise in an interacting many-body system". In: *Nature Physics* 4 (2008), pp. 489–495 (cited on p. 13).

[73] T. Kitagawa, A. Imambekov, J. Schmiedmayer, and E. Demler. "The dynamics and prethermalization of one-dimensional quantum systems probed through the full distributions of quantum noise". In: *New Journal of Physics* 13.7 (2011), p. 073018 (cited on p. 13).

[74] L. Mathey. Personal Communication (cited on p. 15).

[75] I. Shvarchuck, C. Buggle, D. S. Petrov, K. Dieckmann, M. Zielonkowski, M. Kemmann, T. G. Tiecke, W. von Klitzing, G. V. Shlyapnikov, and J. T. M. Walraven. "Bose-Einstein Condensation into Nonequilibrium States Studied by Condensate Focusing". In: *Physical Review Letters* 89.27 (2002), p. 270404 (cited on p. 15).

[76] P. A. Murthy, D. Kedar, T. Lompe, M. Neidig, M. G. Ries, A. N. Wenz, G. Zürn, and S. Jochim. "Matter-wave Fourier optics with a strongly interacting two-dimensional Fermi gas". In: *Physical Review A* 90.4 (2014), p. 043611 (cited on p. 15).

[77] K. Hueck, N. Luick, L. Sobirey, J. Siegl, T. Lompe, and H. Moritz. "Two-Dimensional Homogeneous Fermi Gases". In: *Physical Review Letters* 120.6 (2018), p. 060402 (cited on p. 15).

[78] C. Cohen-Tannoudji, J. Dupont-Roc, and G. Grynberg. *Atom-Photon Interactions. Basis Processes and Applications*. Wiley-VCH Verlag GmbH, 1998 (cited on pp. 17, 18, 22, 49, 53).

[79] R. Grimm, M. Weidemüller, and Y. B. Ovchinnikov. "Optical Dipole Traps for Neutral Atoms". In: *Advances in Atomic, Molecular, and Optical Physics*. Vol. 42. 2000, pp. 95–170 (cited on pp. 17, 18, 42).

[80] R. J. C. Spreeuw, C. Gerz, L. S. Goldner, W. D. Phillips, S. L. Rolston, C. I. Westbrook, M. W. Reynolds, and I. F. Silvera. "Demonstration of neutral atom trapping with microwaves". In: *Physical Review Letters* 72.20 (1994), pp. 3162–3165 (cited on p. 17).

[81] Y. Colombe, E. Knyazchyan, O. Morizot, B. Mercier, V. Lorent, and H. Perrin. "Ultracold atoms confined in rf-induced two-dimensional trapping potentials". In: *Europhysics Letters* 67.4 (2004), pp. 593–599 (cited on pp. 17, 24).

[82] T. Schumm, S. Hofferberth, L. M. Andersson, S. Wildermuth, S. Groth, I. Bar-Joseph, J. Schmiedmayer, and P. Krüger. "Matter-wave interferometry in a double well on an atom chip". In: *Nature Physics* 1 (2005), pp. 57–62 (cited on pp. 17, 97).

[83] B. M. Garraway and H. Perrin. "Recent developments in trapping and manipulation of atoms with adiabatic potentials". In: *Journal of Physics B* 49.17 (2016), p. 172001 (cited on p. 17).

[84] C. Cohen-Tannoudji and S. Haroche. "Interprétation quantique des diverses résonances observées lors de la diffusion de photons optiques et de radiofréquence par un atome". In: *Journal de Physique* 30.1 (1969), pp. 125–144 (cited on p. 18).

[85] C. Cohen-Tannoudji and S. Haroche. "Absorption et diffusion de photons optiques par un atome en interaction avec des photons de radiofréquence". In: *Journal de Physique* 30.2-3 (1969), pp. 153–168 (cited on p. 18).

[86] C. J. Foot. *Atomic Physics*. Oxford University Press, 2005 (cited on pp. 18, 34, 39).

[87] T. Yabuzaki, S. Nakayama, Y. Murakami, and T. Ogawa. "Interaction between a spin-1/2 atom and a strong rf field". In: *Physical Review A* 10.6 (1974), pp. 1955–1963 (cited on p. 19).

[88] C. Cohen-Tannoudji and D. Guéry-Odelin. *Advances in Atomic Physics. An Overview*. World Scientific, 2011 (cited on pp. 19, 22, 23).

[89] F. Bloch and A. Siegert. "Magnetic Resonance for Nonrotating Fields". In: *Physical Review* 57.6 (1940), pp. 522–527 (cited on pp. 22, 23).

[90] J. H. Shirley. "Solution of the Schrödinger Equation with a Hamiltonian Periodic in Time". In: *Physical Review* 138.4B (1965), B979–B987 (cited on p. 22).

[91] B. Yuen and C. J. Foot. *Multi-Frequency Atom-Photon Interactions*. 2019. arXiv: `1907.01469 [quant-ph]` (cited on pp. 22, 26–28).

[92] M. Gildemeister. "Trapping altracold atoms in time-averaged adiabatic potentials". PhD thesis. Oxford University, 2010, pp. 1–146 (cited on pp. 24, 34, 41).

[93] B. Sherlock. "Ultracold Quantum Gases in Time-Averaged Adiabatic Potentials". PhD thesis. Univeristy of Oxford, 2011, pp. 1–223 (cited on pp. 24, 34).

[94] T. L. Harte. "Ultracold atoms in dressed potentials". DPhil thesis. University of Oxford, 2017 (cited on pp. 25, 26, 34, 36, 38, 40, 43, 44, 47, 86).

[95] O. Morizot, C. L. Garrido Alzar, P.-E. Pottie, V. Lorent, and H. Perrin. "Trapping and cooling of rf-dressed atoms in a quadrupole magnetic field". In: *Journal of Physics B* 40.20 (2007), pp. 4013–4022 (cited on p. 29).

[96] L. Landau. "On the theory of transfer of energy at collisions II". In: *Physikalische Zeitschrift der Sowjetunion* 2.46 (1932), p. 118 (cited on p. 31).

[97] C. Zener. "Non-adiabatic crossing of energy levels". In: *Proceedings of the Royal Society of London.* Series A, Containing Papers of a Mathematical and Physical Character 137.833 (1932), pp. 696–702 (cited on p. 31).

[98] K. A. Burrows. "Non-adiabatic losses from radio frequency dressed cold atom traps". PhD thesis. Univeristy of Sussex, 2015 (cited on p. 31).

[99] K. A. Burrows, H. Perrin, and B. M. Garraway. "Nonadiabatic losses from radio-frequency-dressed cold-atom traps: Beyond the Landau-Zener model". In: *Physical Review A* 96.2 (2017), p. 023429 (cited on pp. 31, 97).

[100] S. Hofferberth, B. Fischer, T. Schumm, J. Schmiedmayer, and I. Lesanovsky. "Ultracold atoms in radio-frequency dressed potentials beyond the rotating-wave approximation". In: *Physical Review A* 76.1 (2007), p. 013401 (cited on pp. 49, 52, 62, 65, 67, 68, 71, 72, 75, 81, 85).

[101] H. J. Metcalf and P. van der Straten. *Laser Cooling and Trapping*. Springer, 1999 (cited on p. 34).

[102] K. I. Lee, J. A. Kim, H. R. Noh, and W. Jhe. "Single-beam atom trap in a pyramidal and conical hollow mirror". In: *Optics Letters* 21.15 (1996), pp. 1177–1179 (cited on p. 34).

[103] D. A. Steck. *Rubidium 87 D Line Data*. available online at `http://steck.us/alkalidata` (revision 2.1.5, 13 January 2015) (cited on p. 34).

[104] K. B. Davis, M.-O. Mewes, M. A. Joffe, M. R. Andrews, and W. Ketterle. "Evaporative Cooling of Sodium Atoms". In: *Physical Review Letters* 74.26 (1995), p. 5202 (cited on pp. 35, 75).

[105] T. H. Bergeman, P. McNicholl, J. Kycia, H. Metcalf, and N. L. Balazs. "Quantized motion of atoms in a quadrupole magnetostatic trap". In: *Journal of the Optical Society of America B* 6.11 (1989), pp. 2249–2256 (cited on p. 35).

[106] W. Petrich, M. H. Anderson, J. R. Ensher, and E. A. Cornell. "Stable, Tightly Confining Magnetic Trap for Evaporative Cooling of Neutral Atoms". In: *Physical Review Letters* 74.17 (1995), pp. 3352–3355 (cited on p. 35).

[107] K. Luksch, E. Bentine, A. J. Barker, S. Sunami, T. L. Harte, B. Yuen, and C. J. Foot. "Probing multiple-frequency atom-photon interactions with ultracold atoms". In: *New Journal of Physics* 21.7 (2019), p. 073067 (cited on pp. 52, 61, 63, 64).

[108] E. H. T. Owen. "Towards an Imaging Lattice for Magnetically Trapped Atoms". PhD thesis. University of Oxford, 2017 (cited on pp. 38, 41).

[109] Y. Castin and R. Dum. "Bose-Einstein Condensates in Time Dependent Traps". In: *Physical Review Letters* 77.27 (1996), pp. 5315–5319 (cited on p. 39).

[110] A. J. Barker. DPhil thesis. University of Oxford, In preparation (cited on pp. 40, 95, 106).

[111] W. E. Lamb and R. C. Retherford. "Fine Structure of the Hydrogen Atom by a Microwave Method". In: *Physical Review* 72.3 (1947), pp. 241–243 (cited on p. 49).

[112] A. Antognini et al. "Proton Structure from the Measurement of 2S-2P Transition Frequencies of Muonic Hydrogen". In: *Science* 339.6118 (2013), pp. 417–420 (cited on p. 49).

[113] A. Beyer et al. "The Rydberg constant and proton size from atomic hydrogen". In: *Science* 358.6359 (2017), pp. 79–85 (cited on p. 49).

[114] W. Happer. "Observations of Transitions Between Stationary States in a Rotating Magnetic Field". In: *Physical Review* 136.1A (1964), A35–A42 (cited on p. 49).

[115] M. Allegrini and E. Arimondo. "Radiofrequency transitions in a dressed atom". In: *Journal of Physics B* 4.8 (1971), pp. 1008–1012 (cited on pp. 49, 53).

[116] C. L. Garrido Alzar, H. Perrin, B. M. Garraway, and V. Lorent. "Evaporative cooling in a radio-frequency trap". In: *Physical Review A* 74.5 (2006), p. 053413 (cited on pp. 49, 72).

[117] R. Kollengode Easwaran, L. Longchambon, P.-E. Pottie, V. Lorent, H. Perrin, and B. M. Garraway. "RF spectroscopy in a resonant RF-dressed trap". In: *Journal of Physics B* 43.6 (2010), p. 065302 (cited on pp. 49, 75, 76).

[118] H. Perrin and B. M. Garraway. "Trapping Atoms With Radio Frequency Adiabatic Potentials". In: *Advances In Atomic, Molecular, and Optical Physics*. Ed. by E. Arimondo, C. C. Lin, and S. F. Yelin. Vol. 66. Academic Press, 2017, pp. 181–262 (cited on pp. 49, 55, 62–64, 67, 72, 75, 85).

[119] S. H. Autler and C. H. Townes. "Stark Effect in Rapidly Varying Fields". In: *Physical Review* 100.2 (1955), pp. 703–722 (cited on pp. 3, 50).

[120] B. Yuen. *Quantum Mechanics in Technicolor; Analytic Expressions for a Spin-Half Particle Driven by Polychromatic Light*. 2018. arXiv: `1805.05922 [quant-ph]` (cited on pp. 55, 72).

[121] G. Sinuco-León and B. M. Garraway. "Radio-frequency dressed atoms beyond the linear Zeeman effect". In: *New Journal of Physics* 14.12 (2012), p. 123008 (cited on p. 71).

[122] A. G. Martin, K. Helmerson, V. S. Bagnato, G. P. Lafyatis, and D. E. Pritchard. "rf Spectroscopy of Trapped Neutral Atoms". In: *Physical Review Letters* 61.21 (1988), pp. 2431–2434 (cited on p. 75).

[123] M. H. Anderson, J. R. Ensher, M. R. Matthews, C. E. Wieman, and E. A. Cornell. "Observation of Bose-Einstein Condensation in a Dilute Atomic Vapor". In: *Science* 269.5221 (1995), pp. 198–201 (cited on p. 75).

[124] K. B. Davis, M.-O. Mewes, M. R. Andrews, N. J. van Druten, D. S. Durfee, D. M. Kurn, and W. Ketterle. "Bose-Einstein Condensation in a Gas of Sodium Atoms". In: *Physical Review Letters* 75.22 (1995), pp. 3969–3973 (cited on p. 75).

[125] S. Hofferberth, I. Lesanovsky, B. Fischer, J. Verdu, and J. Schmiedmayer. "Radiofrequency-dressed-state potentials for neutral atoms". In: *Nature Physics* 10 (2006), pp. 710–716 (cited on pp. 33, 75).

[126] B. E. Sherlock, M. Gildemeister, E. Owen, E. Nugent, and C. J. Foot. "Time-averaged adiabatic ring potential for ultracold atoms". In: *Physical Review A* 83.4 (2011), p. 043408 (cited on pp. 78, 107).

[127] M. Gildemeister, B. E. Sherlock, and C. J. Foot. "Techniques to cool and rotate Bose-Einstein condensates in time-averaged adiabatic potentials". In: *Physical Review A* 85.5 (2012), p. 053401 (cited on pp. 78, 107).

[128] S. Sunami. DPhil thesis. University of Oxford, In preparation (cited on p. 95).

[129] S. Eckel, J. G. Lee, F. Jendrzejewski, C. J. Lobb, G. K. Campbell, and W. T. Hill. "Contact resistance and phase slips in mesoscopic superfluid-atom transport". In: *Physical Review A* 93.6 (2016), p. 063619 (cited on p. 42).

[130] A. L. Gaunt, T. F. Schmidutz, I. Gotlibovych, R. P. Smith, and Z. Hadzibabic. "Bose-Einstein Condensation of Atoms in a Uniform Potential". In: *Physical Review Letters* 110.20 (2013), p. 200406 (cited on p. 42).

[131] G. Gauthier, I. Lenton, N. McKay Parry, M. Baker, M. J. Davis, H. Rubinsztein-Dunlop, and T. W. Neely. "Direct imaging of a digital-micromirror device for configurable microscopic optical potentials". In: *Optica* 3.10 (2016), pp. 1136–1143 (cited on p. 42).

[132] W. H. Heathcote, E. Nugent, B. T. Sheard, and C. J. Foot. "A ring trap for ultracold atoms in an RF-dressed state". In: *New Journal of Physics* 10.4 (2008), p. 043012 (cited on pp. 43, 47).

[133] W. Alt. "An objective lens for efficient fluorescence detection of single atoms". In: *Optik* 113.3 (2002), pp. 142–144 (cited on p. 43).

[134] K. Henderson, C. Ryu, C. MacCormick, and M. G. Boshier. "Experimental demonstration of painting arbitrary and dynamic potentials for Bose–Einstein condensates". In: *New Journal of Physics* 11.4 (2009), p. 043030 (cited on p. 43).

[135] T. A. Bell, J. A. P. Glidden, L. Humbert, M. W. J. Bromley, S. A. Haine, M. J. Davis, T. W. Neely, M. A. Baker, and H. Rubinsztein-Dunlop. "Bose–Einstein condensation in large time-averaged optical ring potentials". In: *New Journal of Physics* 18.3 (2016), p. 035003 (cited on p. 43).

[136] M. Endres, H. Bernien, A. Keesling, H. Levine, E. R. Anschuetz, A. Krajenbrink, C. Senko, V. Vuletic, M. Greiner, and M. D. Lukin. "Atom-by-atom assembly of defect-free one-dimensional cold atom arrays". In: *Science* 354.6315 (2016), pp. 1024–1027 (cited on p. 43).

[137] H. Bernien et al. "Probing many-body dynamics on a 51-atom quantum simulator". In: *Nature* 551 (2017), pp. 579–584 (cited on p. 43).

[138] D. Trypogeorgos, T. L. Harte, A. Bonnin, and C. J. Foot. "Precise shaping of laser light by an acousto-optic deflector". In: *Optics Express* 21.21 (2013), pp. 24837–24846 (cited on p. 44).

[139] S. Hunn, K. Zimmermann, M. Hiller, and A. Buchleitner. "Tunneling decay of two interacting bosons in an asymmetric double-well potential: A spectral approach". In: *Physical Review A* 87.4 (2013), p. 043626 (cited on p. 47).

[140] R. Desbuquois, L. Chomaz, T. Yefsah, J. Léonard, J. Beugnon, C. Weitenberg, and J. Dalibard. "Superfluid behaviour of a two-dimensional Bose gas". In: *Nature Physics* 8 (2012), pp. 645–648 (cited on p. 111).

[141] S. E. Weiner, M. C. Tsatsos, L. S. Cederbaum, and A. U. J. Lode. "Phantom vortices: hidden angular momentum in ultracold dilute Bose-Einstein condensates". In: *Scientific Reports* 7.40122 (2017) (cited on p. 111).

[142] O. Fialko, A. S. Bradley, and J. Brand. "Quantum Tunneling of a Vortex between Two Pinning Potentials". In: *Physical Review Letters* 108.1 (2012), p. 015301 (cited on p. 112).

[143] E. Bentine, A. J. Barker, K. Luksch, S. Sunami, T. Harte, B. Yuen, and C. J. Foot. "Inelastic collisions in radiofrequency-dressed mixtures". In preparation.

[144] S. Jammi, T. Pyragius, M. G. Bason, H. M. Florez, and T. Fernholz. "Dispersive detection of radio-frequency-dressed states". In: *Physical Review A* 97.4 (2018), p. 043416 (cited on p. 112).